University of Bath

UNIVERSITY OF
BATH

PHD

Sound and light in periodically microstructured materials

Davies, Elliott John Henry

Award date:
2005

Awarding institution:
University of Bath

Link to publication

SOUND AND LIGHT IN PERIODICALLY MICROSTRUCTURED MATERIALS

Submitted by Elliott John Henry Davies
for the degree of
Doctor of Philosophy
of the University of Bath
2005

E Davies

UMI Number: U197997

UMI U197997

ProQuest LLC
789 East Eisenhower Parkway
P.O. Box 1346
Ann Arbor, MI 48106-1346

Acknowledgements

Abstract

This study is concerned with the properties of elastic waves in periodic systems and their interaction with light.

An overview of the fundamental characteristics of elastic waves in solid systems is given and the wavevector diagram is introduced in treating interfaces. A transfer matrix technique is employed for laminar media and ultimately forms the basis of the analysis of elastic waves in singly periodic systems. The dispersion of longitudinal and shear waves is modelled revealing that anti-plane polarised waves are very similar to light, while in-plane coupled waves behave quite differently due to the presence of the longitudinal strain components. The coupling between the longitudinal and shear waves creates additional stop-bands within the Brillouin zones and not just at the Brillouin zone edges. Analytical expressions are derived, which take account of the coupling between the longitudinal and shear disturbances, to model the positions at which the stop-bands close. The results are presented graphically using wavevector diagrams, dispersion curves and band edge diagrams.

The interaction of elastic waves with light in periodic systems is investigated in the doubly periodic photonic crystal fibre waveguide. Measurements of the Brillouin frequency shift and threshold power are used to characterise the acoustooptic interaction. The experimental results are modelled by approximating the core of the photonic crystal fibre as a silica rod in a vacuum. Several varieties of photonic crystal fibre are studied and multiple Brillouin peaks are shown in the Stokes spectrum.

Key Results

In my attempt to present to you this engaging field of acoustooptics, I have arranged the thesis into two parts. The first part is concerned with the fundamental concepts of elastic wave propagation in layered systems, while the second part is more experimentally orientated and concerned with elastic wave propagation in *photonic crystal fibre*.

I have endeavoured to convey my research and thoughts in as clear a fashion as possible and in initiating that endeavour, I summarise here the main results of my research:

1. Calculated the band structure of elastic waves in singly periodic systems and formulated anti-resonance conditions for in-plane polarised elastic waves which cause the associated stop-bands to close (pp64-67).

2. Modelled the Brillouin frequency shift in photonic crystal fibre by analysing the dispersion of the optical and elastic modes of a free silica rod (pp107-118).

3. Demonstrated the presence of multiple Brillouin peaks in the Brillouin spectrum of a photonic crystal fibre, which is suggestive of the possible guidance of elastic waves by a phononic band gap (pp114-118).

4. Measured threshold powers for stimulated Brillouin scattering in PCF approximately ×10 greater than that predicted by conventional theory (pp119-123).

In recognising these results I would like to thank Paulo Dainese of the Optics and Photonics Research Center, State University at Campinas, Brazil, for his contribution to the measurements of the threshold powers in photonic crystal fibre, and in particular the results shown in figure 11.13 of chapter 11.

Contents

Notes

- A_{eff} — effective area (m^2)

- α — attenuation constant (dB/km)

- a — rod radius (m)

- β — wavevector component parallel to interface (m^{-1})

- C_i — acoustooptic overlap of fundamental optical mode with the ith elastic mode

- c_L — phase velocity of L elastic waves (ms^{-1})

- c_S — phase velocity of S elastic waves (ms^{-1})

- d_i — thickness of layer i of unit cell (m)

- δ_{ij} — Kronecker delta function (1 for $i = j$, 0 for $i \neq j$)

- d — mirror spacing (m)

- ϵ_r — relative dielectric constant

- ϵ_o — electric permittivity of a vacuum (Fm^{-1})

- E — Young's Modulus (Nm^{-2})

- $\mathbf{E}$ — electric field (V/m)

- f — frequency (Hz)

- Δf_B — Brillouin linewidth (Hz)

- Δf_P — pump linewidth (Hz)

- g_B — Brillouin gain (m/W)

- Γ — phonon decay rate (s^{-1})

- G — single pass Brillouin gain

- G_L — reciprocal lattice wavevector (m^{-1})

- $\mathbf{H}$ — magnetic field (Am^{-1})

- I_S — Stokes intensity (Wm^{-2})

- I_P — pump intensity (Wm^{-2})

- k_y — Bloch wavevector (m^{-1})

- $\mathbf{k_E}$ — elastic wavevector (m^{-1})

- $\mathbf{k_P}$ — pump wavevector (m^{-1})

- $\mathbf{k_S}$ — Stokes wavevector (m^{-1})

- L — fibre length (m)

- L_{eff} — effective fibre length (m)

- Λ — Pitch of multilayer stack (m)

- λ — Lamé longitudinal elastic constant (Nm^{-2})

- λ_P — pump wavelength (m)

- m — integer

- μ — Lamé shear elastic constant (Nm^{-2})

- μ_0 — vacuum magnetic permeability (Hm^{-1})

- μ_r — relative magnetic permeability

- n — refractive index

- ω — angular frequency $(rads^{-1})$

- p — component of wavevector normal to the interface (m^{-1})

- Ψ — shear wave potential (m^2)

- ϕ — longitudinal wave potential (m^2)

- P — power (W)

- p_{12} — longitudinal elasto-optic coefficient

- $\mathbf{r}$ — position vector

- ρ — density (kgm^{-3})

- S_{ij} — strain tensor

- $S(\omega)$ — Brillouin lineshape profile

- σ — Poisson's ratio

- τ_{ij} and T_{ij} — stress tensor (Nm^{-2})

- t — time (s)

- $\mathbf{U}$ — displacement (m)

- v_E — elastic wave phase velocity (ms^{-1})

- x, y, z — position coordinates

Part I

Elastic Wave Propagation in Singly Periodic Systems

Chapter 1

Introduction and Literature Review

Chapter 1 introduces the subject of elastic waves in periodic systems. Topical issues, recent achievements and proposals in the field are outlined.

The periodic patterning of materials on a length scale comparable to the wavelength can radically affect wave propagation. This is evident for example in semi-conductor materials where the electron wave function is naturally modulated by the periodicity of the electric potential of the crystal lattice. This periodicity creates regions in energy where the electron is forbidden to exist, namely the energy gaps and energy bands where propagation of the electron is allowed.

This property of blocking wave propagation in certain frequency ranges is also apparent with electromagnetic (EM) waves in structures that possess a periodic variation in refractive index. Such photonic band gap (PBG) materials forbid the presence of photons in the frequency range of a PBG, so that an atom cannot spontaneously emit or absorb light in this region. The advent of PBG materials, as demonstrated by Yablonovitch [1] and John [2], [3], coupled with the fact that only waves and a periodic scatterer are required to produce these band phenomena, has lead to the development of so-called *phononic* band gap materials (the phonon being the quantum of elastic waves or lattice vibration). This analogue of photons in PBG materials and electrons in semi-conductors refers to a range of vibrational frequencies in which the associated vibrations of a structure are suppressed and the material becomes silent.

Periodic structures are well known in modern art, in particular the branch of art classified as a form of "minimalism". The sculpture by Eusebio Sempere, which is exhibited

at the Juan March Foundation in Madrid, consists of a periodic array of vertically arranged hollow stainless steel cylinders. The transmission of sound waves through the structure has been measured and found to vary with frequency and direction [4], [5], [6]. In fact, at certain frequencies and for given directions no sound at all propagates through the structure, clearly demonstrating the presence of a phononic band gap.

In contrast to photonic crystals, phononic crystals exhibit a periodic modulation in density. Kushwaha and Djafari-Rouhani [7] have calculated the band structure for a periodic hexagonal array of metallic rods in air and the experimental measurement of similar systems has been performed by Robertson [8]. The analysis of 3D systems has been demonstrated by Kafesaki *et al.* [9], who, using fcc, bcc and sc arrangements of high density scatterers such as Steel, Nickel, Lead, and Copper embedded in a polymer matrix, demonstrated the formation of full phononic band gaps. Until recently, the density modulation was required to be of the same order as the wavelength in the band gap and so it has not been practical to shield environmental noise as the structures would need to be the size of outdoor sculptures. Liu [10] and co-workers however, have demonstrated full band gaps in 3D phononic crystals composed of silicon coated lead spheres embedded in an epoxy matrix. It has been reported that spectral gaps open up with a lattice constant two orders of magnitude smaller than the relevant wavelength.

The first ideas regarding the influence of a medium interrupted by a periodic array of inclusions on the waves propagating therein, was presented by Rayleigh [11] in 1892. Rayleigh utilised a multi-pole expansion method in analysing the flow of heat and electricity through a doubly periodic system composed of an array of parallel rods of circular cross-section embedded in a uniform background. Zalipaev [12], Poulton [13] and Platts [14], [15] have used this approach extensively in describing elastic wave propagation in such structures, however, this method is limited by the shape of the inclusion that can be incorporated into the analysis. The multi-pole expansion technique represents all waves in terms of Bessel functions and so it is difficult to accommodate non-circular inclusions. Other widely used methods of studying wave propagation include the plane wave expansion of fields [16], [17] and the Fourier series representation of spatially varying material properties; this approach holds no restriction on the shape of the inclusions, but is limited when the contrast in spatial properties between the medium and the inclusions become large.

The approach adopted in this study employs a technique developed in seismology for the study of earth tremors, namely the *transfer matrix* method (see section 3.2), and is ideally suited to systems involving discontinuous changes in material properties. This technique, as the name suggests, uses matrix methods to relate the field components at one particular interface in a stratified composite to any other interface or "horizon". The method has since been applied to multilayer dielectric structures supporting EM

waves [18], [19] and also for analysing elastic waves in periodic systems [20], [21], [22], [23], [24], [25], [26].

The first experimental demonstration of the confinement of elastic waves by a phononic band gap was performed by Marin *et al.* [27] in dual core photonic crystal fibre preform. Such acoustic confinement could lead to highly efficient acoustooptic devices including tunable filters, frequency shifters [28], [29], [30] and even the development of the SASER (Sound Amplification by the Stimulated Emission of Radiation) [31].

The generation of phonons in materials possessing a phononic band gap, using laser radiation, has been performed by several groups [32], [33], [34]. Trigo [35] and Worlock [36] in particular have demonstrated the excitation of phonons within a 1D phononic cavity by EM radiation, due to the photoelastic effect, with the EM radiation itself being confined within a 1D photonic cavity that encloses the phononic cavity.

The band structure of elastic waves in periodic composites is significantly more complicated than the EM case, since elastic waves have a third polarisation state which is coupled to the transverse disturbance. It is the intention of this study to investigate the dispersive properties of elastic waves in materials that are periodic in only 1D as a first step towards treating acoustooptic interactions which form the discussion of Part II.

Chapter 2

Elastic Waves - Properties and Concepts

Chapter 2 discusses the properties of elastic waves and the concepts underlying their propagation in solid media.

All materials are composed of atoms that may be put into various states of vibrational motion. However, for the purposes described here, only the macroscopic effects of the synchronised motion of clusters of atoms are studied in analysing the elastic properties of materials. This allows one to formulate elastic wave theory based on matter as a continuum. In this study, an elastic solid is defined as one in which no energy loss occurs when it returns to its undeformed or equilibrium state. This assumption suppresses the effect of creep associated with viscoelastic materials which have a damping effect on the wave. All solids will therefore be considered as being linear, elastic and ultimately lossless, such that waves propagating in such media do not decay through dissipative mechanisms. Also, to avoid any apparent frequency limitation by referring to a wave as being "acoustic", the term "elastic" will be used throughout when referring to the deformation of a solid.

2.1   Stress, Strain and Hooke's Law

Solids can support various types of wave motion. These disturbances are categorised by the local deformation of the solid relative to the propagation direction. Disturbances that reside in the direction of the wavevector are characteristic of *longitudinal* (L) or dilatational waves, while a motion perpendicular to the propagation direction (a

disturbance unique to solids) is a characteristic of a *shear* (S) or transverse wave. (It is also possible to excite other wave types in rods, but these are not considered here in the study of plates and layered media [37]).

When the particles of a medium are displaced from equilibrium, internal forces will develop to restore the system to its original state. It is these forces combined with the associated inertia of particles that cause the oscillatory motion. This oscillation of particles is described by the displacement vector $\mathbf{U}(\mathbf{r}, t)$, which specifies the displacement of a particle from its initial position $\mathbf{r}$, at a time t.

The displacement field is a continuous variable, but is not a complete description of material deformation. In rigid body translations and rotations the particles of the body retain their relative positions and there is no deformation even though a non-zero displacement field is produced. A more satisfactory measure of material deformation is provided by the gradient of the displacement field,

$$d\mathbf{U}(\mathbf{r}, t) = \frac{\partial \mathbf{U}(\mathbf{r}, t)}{\partial x} dx + \frac{\partial \mathbf{U}(\mathbf{r}, t)}{\partial y} dy + \frac{\partial \mathbf{U}(\mathbf{r}, t)}{\partial z} dz \qquad (2.1)$$

which is zero for rigid translations.

However, this measure of material deformation does not account for rigid body rotations which leaves the internal state of a solid unchanged. Rigid rotations present themselves through the non-zero, anti-symmetric part of the matrix of displacement gradients. Consequently, only the symmetric part which is zero for an overall translation and rotation, successfully describes the deformation [37]. The linearised strain relation (i.e. small strains to avoid permanent deformation or fracture) is given by the symmetric part of the gradient of displacements and is shown below,

$$S_{ij}(\mathbf{r}, t) = \frac{1}{2} \left(\frac{\partial U_i}{\partial r_j} + \frac{\partial U_j}{\partial r_i} \right) \qquad (2.2)$$

where $i, j = 1, 2, 3$ such that $r_1 = x, r_2 = y$ and $r_3 = z$.

Terms in S_{ij} with $i = j$ correspond to the trace of the strain matrix and the sum of these trace elements is termed the dilatation. The dilatation is a measure of the relative change in volume due to a compression or extension of the medium, which itself is due to the passage of an L wave and is given by $\nabla.\mathbf{U}$. In addition to a relative elongation or contraction of the material element in the direction of wave propagation, there is
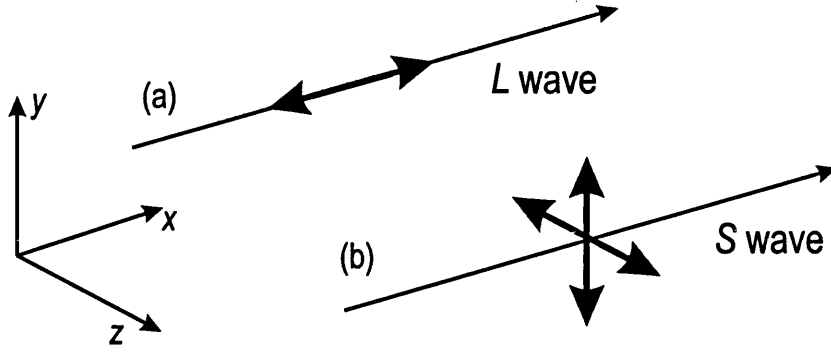
Figure 2.1: Plot showing the displacement associated with (a) longitudinal (L) waves and (b) shear (S) waves

also a small change in the cross-section of the element. This perpendicular strain is characterised by Poisson's ratio (σ), which is defined as the ratio of lateral contraction to longitudinal extension. Terms with $i \neq j$ cause displacements perpendicular to the material element and correspond to a shearing motion which is present as a rotation. Shear waves simply distort the lattice without causing a density gradient along its passage [38]. L and S wave motions are presented pictorially in figure 2.1.

Forces produced during the act of deformation are described by the stress tensor, τ_{ij}, where τ_{ij} refers to the force acting in the j-direction upon a unit area whose perpendicular resides in the i-direction. Such forces can arise from mechanical contact at the free surface of the solid or within the solid (body forces) from an externally applied field, such as the gravitational field or an electric field in a polar crystal. For small stresses and strains, i.e. in the linear theory of elasticity, Hooke's Law in tensor form [39] describes this deformation as,

$$\tau_{ij} = \lambda \left(\frac{\partial U_k}{\partial x_k} \right) \delta_{ij} + \mu \left(\frac{\partial U_i}{\partial x_j} + \frac{\partial U_j}{\partial x_i} \right) \tag{2.3}$$

where λ and μ are the Lamé elastic constants and δ_{ij} is the Kronecker delta function. (Einsteins suffix notation is implied here whereby summation is applied over terms with repeated indices).

Newtons 2nd Law for a particle in a solid describes the acceleration in terms of the forces to which it is subjected (body forces being neglected). Thus, using equation 2.3 the wave equation for particles in a solid can be written as,

$$\rho \frac{\partial^2 U_j}{\partial t^2} = \frac{\partial \tau_{ij}}{\partial x_i} \tag{2.4}$$

7

where ρ is the density of the medium at equilibrium (i.e. with no elastic disturbance) and $i, j = 1, 2, 3$ such that 1 corresponds to the x-component, 2 corresponds to the y-component and 3 corresponds to the z-component.

2.2 Elastic Wave Propagation in Unbounded Media

The general expression dictating the passage of an elastic wave through a solid is obtained on substituting equation 2.3 into equation 2.4. This produces,

$$\frac{\partial^2 U_j}{\partial t^2} = \frac{\partial}{\partial x_j}\left[\lambda \frac{\partial U_k}{\partial x_k}\right] + \frac{\partial}{\partial x_i}\left[\mu\left(\frac{\partial U_i}{\partial x_j} + \frac{\partial U_j}{\partial x_i}\right)\right] \qquad (2.5)$$

where $k = 1, 2, 3$, such that 1 corresponds to the x-component, 2 corresponds to the y-component, etc. The vector form of 2.5 is quoted in many texts and papers without any reference to the derivation. For this reason, it is included here and proceeds by analysing each component of **U** independently. For the x-component, equation 2.5 yields,

$$\rho\frac{\partial^2 U_x}{\partial t^2} = \underbrace{\frac{\partial}{\partial x}\left[\lambda\frac{\partial U_x}{\partial x} + \lambda\frac{\partial U_y}{\partial y} + \lambda\frac{\partial U_z}{\partial z}\right]}_{a} + \underbrace{\frac{\partial\mu}{\partial x_i}\left[\frac{\partial U_i}{\partial x} + \frac{\partial U_x}{\partial x_i}\right]}_{b} + \underbrace{\mu\frac{\partial}{\partial x_i}\left[\frac{\partial U_i}{\partial x} + \frac{\partial U_x}{\partial x_i}\right]}_{c}.$$
$$(2.6)$$

Now expanding a it is found,

$$a = \frac{\partial\lambda}{\partial x}\frac{\partial U_x}{\partial x} + \frac{\partial\lambda}{\partial x}\frac{\partial U_y}{\partial y} + \frac{\partial\lambda}{\partial x}\frac{\partial U_z}{\partial z} + \lambda\left[\frac{\partial^2 U_x}{\partial x^2} + \frac{\partial^2 U_y}{\partial x\partial y} + \frac{\partial^2 U_z}{\partial x\partial z}\right] \qquad (2.7)$$

and similarly,

$$b = \frac{\partial\mu}{\partial x}\frac{\partial U_x}{\partial x} + \frac{\partial\mu}{\partial y}\frac{\partial U_y}{\partial x} + \frac{\partial\mu}{\partial z}\frac{\partial U_z}{\partial x} + \frac{\partial\mu}{\partial x}\frac{\partial U_x}{\partial x} + \frac{\partial\mu}{\partial y}\frac{\partial U_x}{\partial y} + \frac{\partial\mu}{\partial z}\frac{\partial U_x}{\partial z} \qquad (2.8)$$

$$c = \mu\frac{\partial^2 U_x}{\partial x^2} + \mu\frac{\partial^2 U_y}{\partial x\partial y} + \mu\frac{\partial^2 U_z}{\partial x\partial z} + \mu\frac{\partial^2 U_x}{\partial x^2} + \mu\frac{\partial^2 U_x}{\partial y^2} + \mu\frac{\partial^2 U_x}{\partial z^2}. \qquad (2.9)$$

Therefore, combining 2.6, 2.7, 2.8 and 2.9, the expression for the x-component of the wave can be written as,

$$\rho\frac{\partial^2 U_x}{\partial t^2} = \frac{\partial \lambda}{\partial x}(\nabla.\mathbf{U}) + \lambda\frac{\partial}{\partial x}(\nabla.\mathbf{U}) + \nabla\mu.\frac{\partial \mathbf{U}}{\partial x} + (\nabla\mu.\nabla)U_x + \mu\frac{\partial}{\partial x}(\nabla.\mathbf{U}) + \mu\nabla^2 U_x. \quad (2.10)$$

In a similar fashion, the y and z-components can be represented as,

$$\rho\frac{\partial^2 U_y}{\partial t^2} = \frac{\partial \lambda}{\partial y}(\nabla.\mathbf{U}) + \lambda\frac{\partial}{\partial y}(\nabla.\mathbf{U}) + \nabla\mu.\frac{\partial \mathbf{U}}{\partial y} + (\nabla\mu.\nabla)U_y + \mu\frac{\partial}{\partial y}(\nabla.\mathbf{U}) + \mu\nabla^2 U_y \quad (2.11)$$

$$\rho\frac{\partial^2 U_z}{\partial t^2} = \frac{\partial \lambda}{\partial z}(\nabla.\mathbf{U}) + \lambda\frac{\partial}{\partial z}(\nabla.\mathbf{U}) + \nabla\mu.\frac{\partial \mathbf{U}}{\partial z} + (\nabla\mu.\nabla)U_z + \mu\frac{\partial}{\partial z}(\nabla.\mathbf{U}) + \mu\nabla^2 U_z. \quad (2.12)$$

The vector form of the wave equation for elastic waves in solids is therefore obtained by combining equations 2.10, 2.11 and 2.12, and takes the form,

$$\rho\frac{\partial^2 \mathbf{U}}{\partial t^2} = (\nabla.\mathbf{U})\nabla\lambda + \lambda\nabla(\nabla.\mathbf{U}) + \mathbf{\Sigma} + (\nabla\mu.\nabla)\mathbf{U} + \mu\nabla(\nabla.\mathbf{U}) + \mu\nabla^2\mathbf{U} \quad (2.13)$$

where,

$$\mathbf{\Sigma} = \nabla\mu.\frac{\partial \mathbf{U}}{\partial x}\mathbf{i} + \nabla\mu.\frac{\partial \mathbf{U}}{\partial y}\mathbf{j} + \nabla\mu.\frac{\partial \mathbf{U}}{\partial z}\mathbf{k} \quad (2.14)$$

and $\mathbf{i}$, $\mathbf{j}$ and $\mathbf{k}$ are Cartesian unit vectors along the x, y and z directions respectively. Upon expanding equation 2.14 it is found that,

$$\mathbf{\Sigma} = \left(\frac{\partial \mu}{\partial x}\frac{\partial U_x}{\partial x} + \frac{\partial \mu}{\partial y}\frac{\partial U_y}{\partial x} + \frac{\partial \mu}{\partial z}\frac{\partial U_z}{\partial x}\right)\mathbf{i} + \left(\frac{\partial \mu}{\partial x}\frac{\partial U_x}{\partial y} + \frac{\partial \mu}{\partial y}\frac{\partial U_y}{\partial y} + \frac{\partial \mu}{\partial z}\frac{\partial U_z}{\partial y}\right)\mathbf{j} +$$
$$\left(\frac{\partial \mu}{\partial x}\frac{\partial U_x}{\partial z} + \frac{\partial \mu}{\partial y}\frac{\partial U_y}{\partial z} + \frac{\partial \mu}{\partial z}\frac{\partial U_z}{\partial z}\right)\mathbf{k} \quad (2.15)$$

and comparing 2.15 with 2.16 below,

$$\nabla\mu \times (\nabla \times \mathbf{U}) = \left[\frac{\partial\mu}{\partial y}\left(\frac{\partial U_y}{\partial x} - \frac{\partial U_x}{\partial y}\right) - \frac{\partial\mu}{\partial z}\left(\frac{\partial U_x}{\partial z} - \frac{\partial U_z}{\partial x}\right)\right]\mathbf{i}$$

$$+ \left[\frac{\partial\mu}{\partial z}\left(\frac{\partial U_z}{\partial y} - \frac{\partial U_y}{\partial z}\right) - \frac{\partial\mu}{\partial x}\left(\frac{\partial U_y}{\partial x} - \frac{\partial U_x}{\partial y}\right)\right]\mathbf{j}$$

$$+ \left[\frac{\partial\mu}{\partial x}\left(\frac{\partial U_x}{\partial z} - \frac{\partial U_z}{\partial x}\right) - \frac{\partial\mu}{\partial y}\left(\frac{\partial U_z}{\partial y} - \frac{\partial U_y}{\partial z}\right)\right]\mathbf{k} \qquad (2.16)$$

the vector form of 2.5 can be written as,

$$\rho\frac{\partial^2\mathbf{U}}{\partial t^2} = (\nabla.\mathbf{U})\nabla\lambda + (\lambda + \mu)\nabla(\nabla.\mathbf{U}) + 2(\nabla\mu.\nabla)\mathbf{U} + \nabla\mu \times (\nabla \times \mathbf{U}) + \mu\nabla^2\mathbf{U}. \quad (2.17)$$

In ideal, homogeneous, isotropic solids the elastic constants λ and μ do not have any spatial dependence. Therefore, $\nabla\lambda = \nabla\mu = 0$ and equation 2.17 reduces to,

$$\frac{\partial^2\mathbf{U}}{\partial t^2} = \frac{(\lambda + 2\mu)}{\rho}\nabla(\nabla.\mathbf{U}) - \frac{\mu}{\rho}\nabla \times (\nabla \times \mathbf{U}). \qquad (2.18)$$

Equation 2.18 is representative of three waves which have different polarisations, namely the L wave in which the disturbance takes place in the same direction as the wavevector and the two S waves (which are mutually orthogonal) in which the displacement resides in a plane perpendicular to the propagation direction.

In unbounded isotropic media, L and S waves propagate independently of each other. However, at defects within the main body of media, interfaces and free surfaces for example, the L and S waves become coupled. The analysis of each type of wave is facilitated through the use of the longitudinal and shear potentials (ϕ and Ψ respectively) which decouple equation 2.18 [37], [38], [39]. However, this approach is only valid when the system under consideration is homogeneous and isotropic. For more general systems involving inhomogeneous media the reader is referred to the paper by Hook [40].

The L and S potentials describing their respective displacements are defined as,

$$\mathbf{U_L} = \nabla\phi \qquad (2.19)$$

$$\mathbf{U_S} = \nabla \times \Psi \qquad (2.20)$$

such that there is no local rotation of the medium associated with the passage of an L wave ($\nabla \times \mathbf{U_L} = 0$) and no volume change associated with the passage of a S wave ($\nabla.\mathbf{U_S} = 0$) [41]. Substituting $\mathbf{U} = \nabla\phi + \nabla \times \mathbf{\Psi}$ in 2.18, gives,

$$(\lambda + 2\mu)\nabla\nabla.[\nabla\phi + \nabla \times \mathbf{\Psi}] - \mu\nabla \times \nabla \times [\nabla\phi + \nabla \times \mathbf{\Psi}] - \rho\frac{\partial^2(\nabla\phi + \nabla \times \mathbf{\Psi})}{\partial t^2} = 0 \quad (2.21)$$

which reduces to,

$$\nabla\left((\lambda + 2\mu)\nabla^2\phi - \rho\frac{\partial^2\phi}{\partial t^2}\right) + \nabla \times \left(\mu\nabla^2\mathbf{\Psi} - \rho\frac{\partial^2\mathbf{\Psi}}{\partial t^2}\right) = 0. \quad (2.22)$$

Each term in brackets must be independently zero, and so we have the scalar wave equation for the L waves,

$$\nabla^2\phi - \frac{\rho}{(\lambda + 2\mu)}\frac{\partial^2\phi}{\partial t^2} = 0 \quad (2.23)$$

and the vector wave equation for the S waves,

$$\nabla^2\mathbf{\Psi} - \frac{\rho}{\mu}\frac{\partial^2\mathbf{\Psi}}{\partial t^2} = 0. \quad (2.24)$$

From equations 2.23 and 2.24, the phase velocity of the L and S waves, (c_L and c_S respectively) are given by,

$$c_L = \left(\frac{\lambda + 2\mu}{\rho}\right)^{1/2} \quad (2.25)$$

$$c_S = \left(\frac{\mu}{\rho}\right)^{1/2} \quad (2.26)$$

and since λ is always greater than zero, $c_L > c_S\sqrt{2}$. The plane wave solutions to 2.23 and 2.24 can be written as,

$$\phi = \phi_A \exp i(\mathbf{k_L}.\mathbf{r} - \omega t) \quad (2.27)$$

11

$$\mathbf{\Psi} = \mathbf{\Psi_A} \exp i(\mathbf{k_S}.\mathbf{r} - \omega t) \qquad (2.28)$$

where ϕ_A and $\mathbf{\Psi_A}$ are constants, ω is the angular frequency, and $|\mathbf{k_L}| = \omega/c_L$ and $|\mathbf{k_S}| = \omega/c_S$ are the magnitudes of the L and S wavevectors, respectively.

2.3   Elastic Waves at an Interface

Elastic wave propagation in bounded solids is complicated by the coupling of the L and S waves at boundaries and interfaces. For two infinite (much larger than the relevant wavelength), homogeneous, isotropic, elastic half-spaces with a welded contact so that no slip takes place, it is possible to define a coordinate system such that the SH disturbance (or shear wave with horizontal polarisation) which takes place in a direction parallel to the interface, is uncoupled to the SV (or shear wave with vertical polarisation) and L wave. This is only viable if the system is invariant to any rotation about the normal to the interface. Thus, in defining an interface with the normal pointing in the y-direction and the x-y plane as the plane of incidence (also known as the sagittal plane), an SH wave would produce a displacement in the z-direction only (this wave is also referred to as anti-plane shear and is similar to the TE mode in photonics [42]) and so the dimensionality of the problem can be reduced (see figure 2.2). In this respect, it is also evident that the L and SV waves (i.e. in-plane polarised waves) are coupled and both present a displacement perpendicular to the z-direction.

The displacement associated with the anti-plane waves ($\mathbf{U^{ap}}$) is derived from 2.20 with the components of the vector potential, $\mathbf{\Psi} = (\Psi_x, \Psi_y, 0)$ being independent of the z-coordinate. Accordingly,

$$\mathbf{U^{ap}} = \left(\frac{\partial \Psi_y}{\partial x} - \frac{\partial \Psi_x}{\partial y}\right)\mathbf{k}. \qquad (2.29)$$

The L and SV waves are coupled to each other at the interface such that an L (SV) wave incident on the interface will produce a reflected and transmitted L (SV) wave as well as exciting an SV (L) wave in the adjoining media. The displacement of the coupled in-plane waves ($\mathbf{U^{ip}}$) is revealed through 2.19 and 2.20 with $\mathbf{\Psi} \rightarrow (0, 0, \Psi_z)$ and is given by,

$$\mathbf{U^{ip}} = \left(\frac{\partial \phi}{\partial x} + \frac{\partial \Psi_z}{\partial y}\right)\mathbf{i} + \left(\frac{\partial \phi}{\partial y} - \frac{\partial \Psi_z}{\partial x}\right)\mathbf{j}. \qquad (2.30)$$
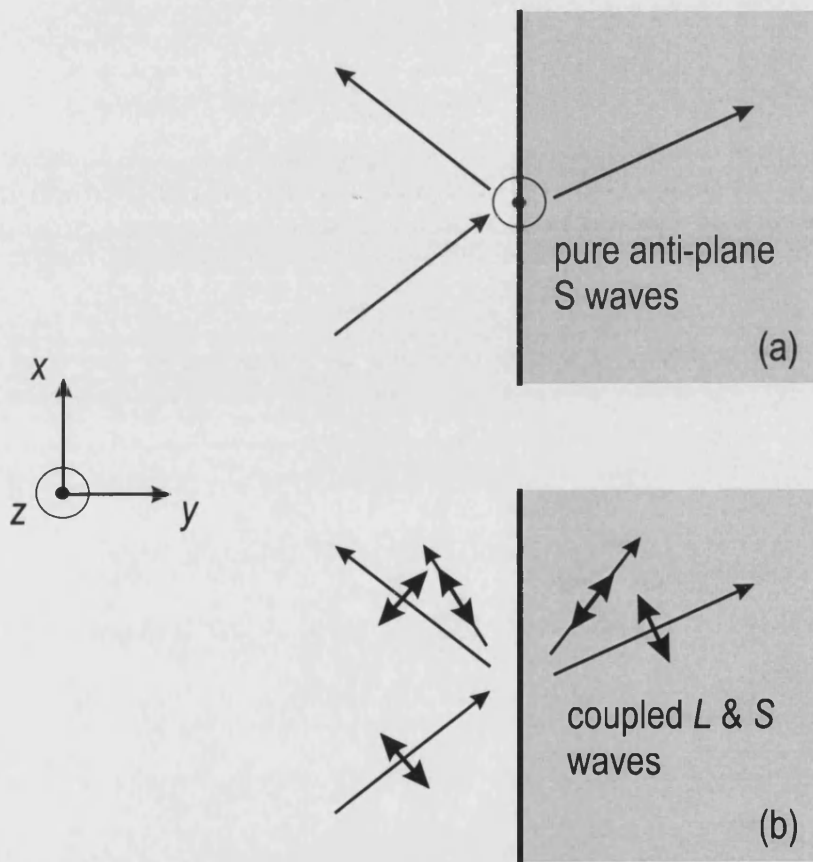
Figure 2.2: Diagram illustrating the polarisation of L and S waves at an interface. (a) Uncoupled anti-plane waves (b) coupled in-plane waves.

At any interface between two media it is required that the wavevector component along the interface be conserved in an analogous manner to EM waves. This result leads to Snells Law [42], which states,

$$\frac{sin(\theta_i)}{v_1} = \frac{sin(\theta_r)}{v_1} = \frac{sin(\theta_t)}{v_2} \qquad (2.31)$$

where v_1 and v_2 are the phase velocities of the elastic waves in materials 1 and 2, and θ_i, θ_r and θ_t are the angles made by the incident, reflected and transmitted waves to the normal to the interface respectively.

In addition to L and S waves, for certain material combinations it is found that guided waves can exist at the interface between different media. These waves were studied by Stoneley [43] and are accordingly named after him. Stoneley waves rapidly decay with increasing distance from the interface into the surrounding media and are polarised in a plane containing the propagation direction and the normal to the interface. The Stoneley wave is a generalised form of the so-called Rayleigh wave, which is trapped at the free surface of a solid (see section 2.3.1) and is found to exist when the elastic wavelength is small compared to the thickness of the solid in question. The formation of the Rayleigh wave is not restricted by the properties of the media forming the interface as with the Stoneley wave, but is polarised in the same sense. The two displacement components of the Rayleigh wave however, have a phase difference of $\pi/2$ and their amplitudes decay with depth at different rates.

2.3.1 Boundary Conditions

Solutions to the wave equations 2.23 and 2.24, which govern the propagation of L and S waves, will depend on the boundary to the system in which the waves propagate. For elastic waves in a solid that is rigidly bonded to a second solid such that no slip can take place (welded interface), the boundary conditions simply require the conservation of displacement and the normal components of stress across the boundary. Solid-liquid interfaces however, only require the conservation of the normal component of displacement and stress. This is because liquids do not possess any resistance to a shearing motion and consequently cannot support a shear wave.

An elastic wave is inherently a disturbance of a particular medium. It is no surprise therefore that a vacuum cannot support an elastic wave. As a result, elastic waves incident on a free surface (i.e. an interface with a vacuum) must satisfy the condition of zero stress at the boundary and be totally reflected. In this manner, there is no

restriction to the displacement at the free surface, provided the resultant stress at the boundary is zero [37], [38], [39].

An interesting theoretical boundary condition is that proposed by Mindlin [44]. The so-called lubricated boundary is an idealised condition which serves to prevent L and S waves from coupling at an interface between two homogeneous, isotropic solids. An L (S) wave incident on a lubricated surface will thus only reflect and transmit into an L (S) wave thereby preserving the state of polarisation (no mode conversion). This allows the L (S) wave to be studied independently of the S (L) wave, and is implemented by setting either the normal component of displacement and tangential component of stress to zero, or equivalently, the tangential component of displacement and the normal component of stress to zero.

2.3.2   The Wavevector Diagram for Waves at an Interface

Waves incident on and departing from an interface are concisely represented through the use of a wavevector diagram [45]. This is a plot in wavevector space of the magnitude and direction of all the allowed real valued wavevectors at constant frequency, ω. In essence it is a plot of the spatial dispersion at a fixed frequency.

The shape of the wavevector diagram reflects the directional dependence of the material properties, i.e. the anisotropy. For isotropic materials however, the magnitude of the wavevector is constant for all directions and so the the diagram is simply circular with a radius of $\frac{\omega}{c}$.

Anti-Plane Polarised Waves

The wavevector diagram representing the interaction of anti-plane shear waves at an interface between two homogeneous, isotropic media, labelled 1 and 2, is shown in figure 2.3.

The conservation of wavevector component along the interface is evident through the use of the construction line. It is seen that the wavevector in each media can be decomposed into two orthogonal components, namely the wavevector component parallel to the interface β, and the component normal to the interface, p_S, which is given by,

15
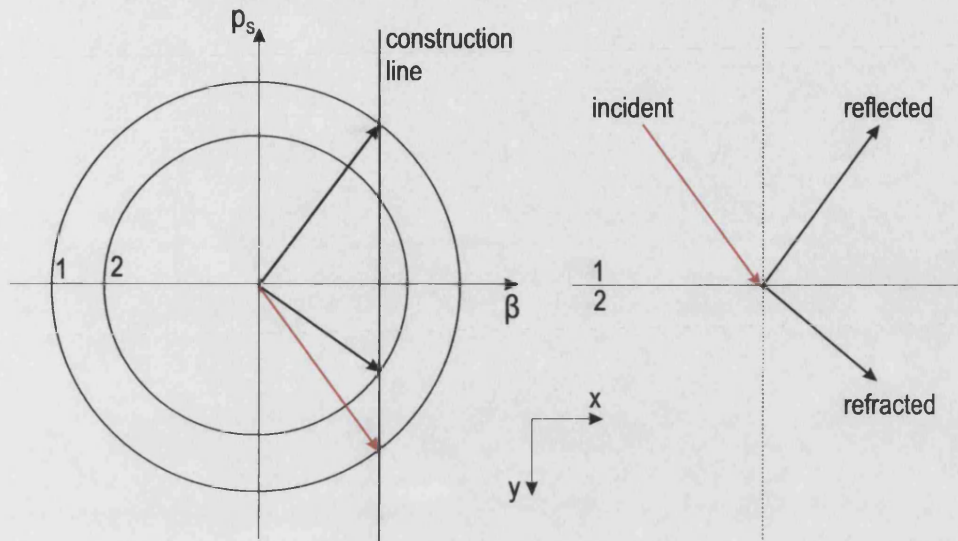
Figure 2.3: Reflection and refraction of anti-plane S waves at an interface between two isotropic media 1 and 2.

$$p_S = \sqrt{\frac{\omega^2}{c_S^2} - \beta^2}.$$ (2.32)

Values of $|\beta| < \frac{\omega}{c_{S2}}$ (where c_{S2} is the phase velocity of anti-plane waves in medium 2) correspond to the regime where anti-plane waves can freely propagate and in which reflection and refraction can occur.

When $|\beta|$ equals $\frac{\omega}{c_{S2}}$, the anti-plane waves will be cut-off from medium 2. This value of β defines the critical angle, equivalent to the critical angle in optics required for total internal reflection. From equation 2.32, it is evident that for $|\beta| > \frac{\omega}{c_{S2}}$, p_{S2} will be imaginary and so the anti-plane waves will be evanescent in medium 2, decaying in a direction normal to the interface. Equally, for $|\beta| > \frac{\omega}{c_{S1}}$, the waves will be evanescent in both media and so the system will be unable to support anti-plane waves at that frequency [18].

In-Plane Polarised Waves

The typical wavevector diagram showing in-plane polarised waves at an interface between two isotropic media is shown in figure 2.4. The four circles are representative of the two types of elastic waves that can propagate in both media, namely the L and S waves. Since $\lambda > 0$, the velocity of the L wave in a given solid is always greater than the S wave. Thus, the L wavevector is always smaller than the S wave at a given fre-
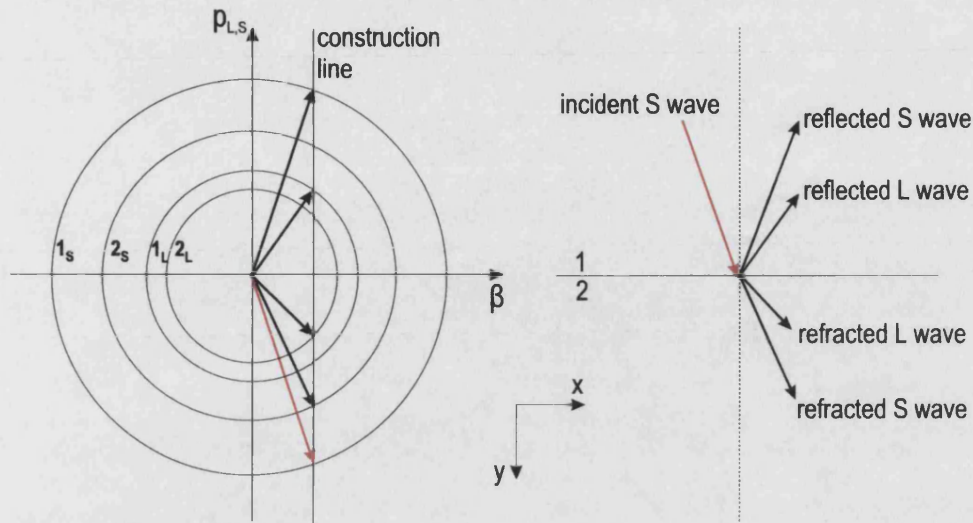
Figure 2.4: Wavevector diagram showing the coupling of L and S waves at an interface between two media which have different densities. Labels 1_L, 2_L, 1_S and 2_S indicate the L and S waves in media 1 and 2, respectively.

Type of Interface	Relative Phase Velocity
I	$c_{L2} > c_{L1} > c_{S2} > c_{S1}$
II	$c_{L2} > c_{S2} > c_{L1} > c_{S1}$
III	$c_{L2} > c_{L1} > c_{S1} > c_{S2}$

Table 2.1: A summary of the possible relative phase velocities of the L and S waves at an interface between two solid media.

quency and in a given solid. Despite this restriction, it is possible to define three types of interface based on the density of the adjoining media, which I shall call respectively type I, II and III. These labels are necessitated as it is believed that no distinction has previously been made; it is important to realise which type of system the coupled waves relate to as it governs the wave propagation.

The interface labelled type I refers to the case whereby both L waves travel faster than the S waves, i.e. $c_{L2} > c_{L1} > c_{S2} > c_{S1}$. A type II interface refers to the situation whereby $c_{L2} > c_{S2} > c_{L1} > c_{S1}$, and the type III interface refers to the system in which $c_{L2} > c_{L1} > c_{S1} > c_{S2}$ namely, the phase velocity of the L and S waves in medium 1 are intermediate to the L and S wave phase velocity in medium 2. These interfaces are summarised in table 2.1.

Figure 2.4 is representative of a type I interface and highlights five propagation regimes (compared to three for anti-plane polarised waves) which are distinguished by the value of β. However, only three of these are of particular interest.

For values of β defined by $|\beta| < \frac{\omega}{c_{L2}}$, all waves are real and can propagate to participate in reflection and refraction.

The range of wavevector values defined as $\frac{\omega}{c_{L2}} < |\beta| < \frac{\omega}{c_{L1}}$ relate to the situation in which the y-component of the L wavevector in medium 2 is imaginary; this results in the exponential decay in of L waves in medium 2. Consequently all L waves incident on the interface from medium 1 will be reflected and furthermore, S waves incident upon the interface from medium 1 will not be partially refracted into an L wave in medium 2. (Equally, S waves incident upon the interface from medium 2 will not be reflected into an L wave).

The third regime is defined as $\frac{\omega}{c_{L1}} < |\beta| < \frac{\omega}{c_{S1}}$, corresponds to the situation in which the L waves will be evanescent in the both half-spaces. In this situation only S wavevectors are real valued can thus propagate freely.

The fourth regime is given by $\frac{\omega}{c_{S2}} < |\beta| < \frac{\omega}{c_{S1}}$ and is such that only an S wave can propagate in medium 1. All other waves will be evanescent and so an S wave incident on the interface from medium 1 will be totally reflected. As the β value continues to increase beyond $\frac{\omega}{c_{S1}}$, the S wave in medium 1 will become evanescent with the result that the system can no longer support in-plane polarised waves at that frequency.

2.3.3 Brewster's Condition and Angles of Polarisation Exchange

In photonics, Brewster's condition refers to the well known angle for which a TM polarised EM wave incident on an interface between two media produces no reflection. The magnitude of the reflection is zero when the reflected and refracted angles are orthogonal. Under such circumstances, the electric dipoles of the reflected and refracted waves are at right angles, resulting in zero reflected power [18], [42].

For elastic waves, the analogous polarisation state refers to the in-plane polarised L and S waves. At an interface between two solids, the L and S waves become coupled and are capable of generating their coupled partner in reflection and transmission. Since L and S waves have different speeds they will leave the interface at different angles (since β must be conserved), and so at most it is only possible to suppress the reflection of one of the coupled waves.

An analytic expression for the β value at which mode conversion takes place is a complicated function of the material properties of both media and wavevector components (see section 3.4). However, the β value at which an L (S) wave is reflected at an inter-

face solely into an S (L) wave is obtained by setting the reflection coefficient of an L (S) wave into an L (S) wave to zero, i.e. $V_{LL}, V_{SS} = 0$.

Figure 2.5 shows the magnitude of the reflection and transmission coefficients of the L and S potentials for L and S waves incident upon an interface between two solid half-spaces having different mechanical properties. It is evident that at a β value of ≈ 0.68, the reflection of an L (S) wave into an L (S) wave becomes zero, indicating the total reflection of one polarisation state into the other. This β value will of course vary according to the property of the materials forming the interface and indeed for some material combinations no mode conversion takes place. The complete analysis of in-plane waves at a free surface and their dependency on the material properties, is given by Malischewsky [46].

The reflection of anti-plane waves at an interface between two solid media (labelled 1 and 2) is given by

$$r = \frac{p_1 \mu_1 - p_2 \mu_2}{p_1 \mu_1 + p_2 \mu_2}.$$
(2.33)

The reflection can be seen to go to zero when $p_1 \mu_1 = p_2 \mu_2$. This Brewster like condition is found to be dependent on the material properties and is considered in detail by Manzanares-Martinez [47]. Through setting the numerator of equation 2.33 to zero, this Brewster condition can be shown to occur at frequencies given by,

$$\omega^2 = \beta^2 \left[\frac{(c_1 c_2)^2 (\mu_1^2 - \mu_2^2)}{(\mu_1 c_2)^2 - (\mu_2 c_1)^2} \right].$$
(2.34)

Angles of Polarisation Exchange and Conservation at a Free Boundary

In-plane polarised waves incident upon a boundary to a vacuum from an elastic half-space demonstrate further interesting polarisation effects upon reflection. It can be shown that the reflection of an L wave or an S wave (at an interface to a vacuum) into an L wave or an S wave respectively, is given by,

$$r_1 = \frac{4\beta^2 p_L p_S - (\beta^2 - p_S^2)^2}{4\beta^2 p_L p_S + (\beta^2 - p_S^2)^2}.$$
(2.35)
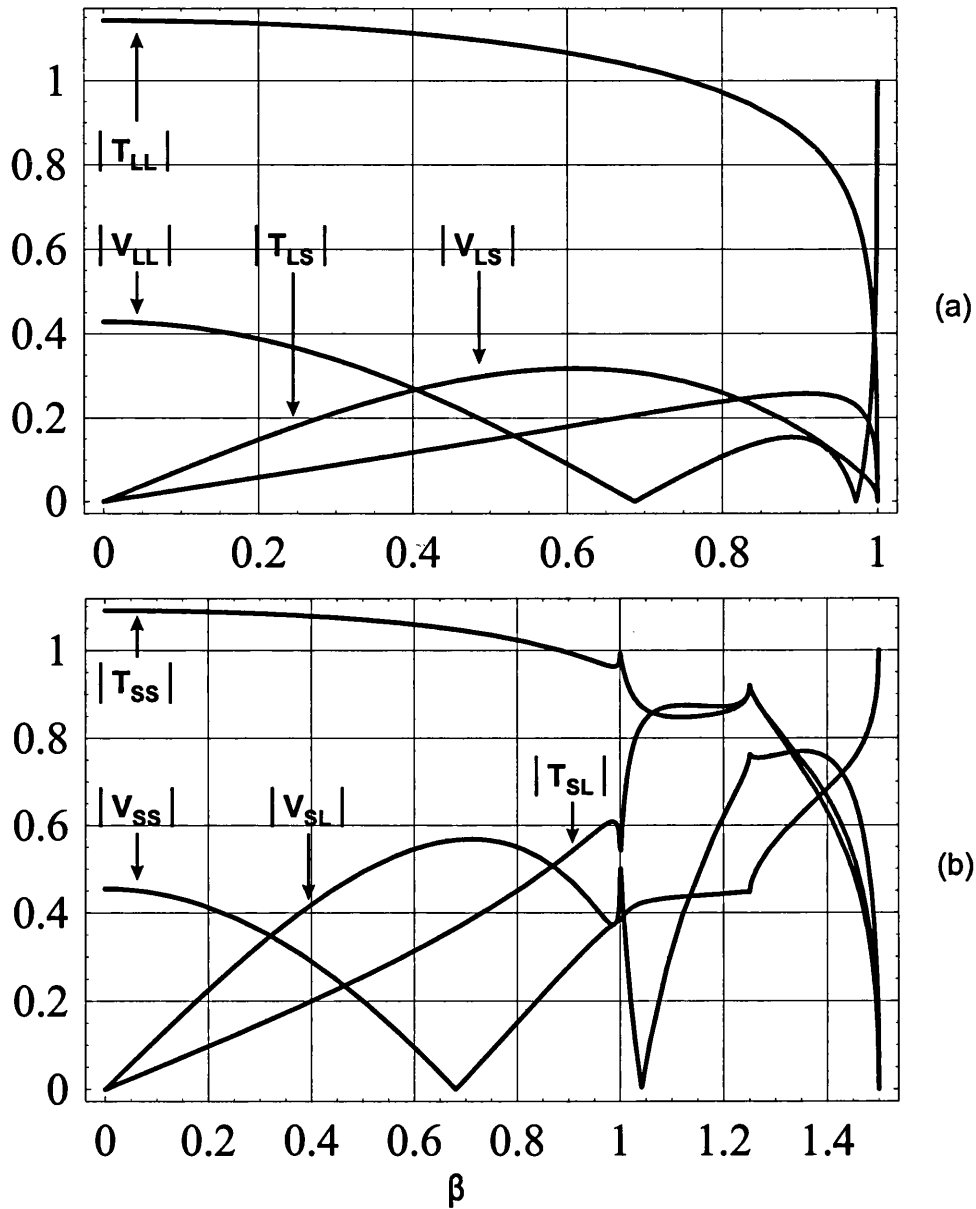
Figure 2.5: Plots showing the magnitude of the reflection (V) and transmission(T) coefficients *of potentials* for (a) an L wave and (b) an S wave, incident from a first elastic half-space (density - ρ_1) upon a welded interface to second solid half-space (density $\rho_2 = \rho_1/2$). In both plots the reflection of an L (S) wave into an L (S) wave (i.e. $V_{LL} = 0(V_{SS} = 0)$) is seen to go to zero at $\beta \approx 0.68$. Note, for the incident medium, $|k_L| = 1$, $|k_S| = 1.5$.

From equation 2.35 it is readily seen that when $4\beta^2 p_L p_S = (\beta^2 - p_S^2)^2$ the reflection does not generate a wave with the same polarisation as that which was incident ($r_1 = 0$). Thus, an L wave incident upon the interface and satisfying the aforementioned condition will be converted to an S wave. Similarly, an S wave incident upon the interface will generate an L wave only under reflection; the elastic wave is said to undergo an *exchange of polarisation*.

Conversely, the reflection of an L wave into an S wave at an interface to a vacuum can be shown to be of the form,

$$r_2 = \frac{4\beta p_L(\beta^2 - p_S^2)}{4\beta^2 p_L p_S + (\beta^2 - p_S^2)} \tag{2.36}$$

and so when $\beta = p_S$, r_2 will become 0. Under such circumstances, an L (S) wave will be totally reflected into an L (S) wave — the state of *polarisation is said to be conserved* [39].

Values of β which satisfy equations 2.35 and 2.36 will also be dependent on Poisson's ratio, σ, which can be expressed in the form,

$$\frac{k_L^2}{k_S^2} = \frac{(1 - 2\sigma)}{(2 - 2\sigma)}. \tag{2.37}$$

The values of β which satisfy equations 2.35 and 2.36 are shown as a function of σ in figure 2.6 for an L wave incident upon the interface. (Values of $\sigma < 0$ correspond to the unusual case whereby a material bulges when stretched, or constricts when squashed). It is evident that at a given frequency, the condition for polarisation exchange (blue line) is only permitted up to a maximum value of σ. There will however, always exist an elastic solid for which the polarisation of a wave incident upon an interface to a vacuum from the solid will be conserved under reflection (red line).

2.4   Energy and the Poynting Vector

The energy associated with an elastic wave can be written as,

$$E = \frac{-\mathbf{U}^* . \tau}{2} \tag{2.38}$$
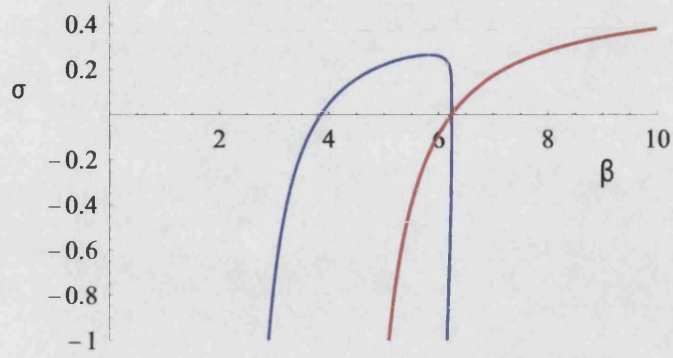
Figure 2.6: Plot showing values of Poisson's ratio σ, which satisfy the condition for polarisation exchange (blue line) and polarisation conservation (red line), as a function of β.

where $*$ indicates the complex conjugate. Thus, the power flow (energy per unit time) associated with an elastic wave becomes,

$$\mathbf{P} = \frac{\partial E}{\partial t} = \frac{-\mathbf{V}^* . \tau}{2} \tag{2.39}$$

which can be expanded to reveal,

$$\mathbf{P} = -\frac{1}{2} \left[v_x^* \tau_{11} + v_y^* \tau_{12} + v_z^* \tau_{13} \right] \mathbf{i} - \frac{1}{2} \left[v_x^* \tau_{21} + v_y^* \tau_{22} + v_z^* \tau_{23} \right] \mathbf{j}$$

$$-\frac{1}{2} \left[v_x^* \tau_{31} + v_y^* \tau_{32} + v_z^* \tau_{33} \right] \mathbf{k} \tag{2.40}$$

where $\mathbf{V}$ is the phase velocity vector of the elastic wave and $\mathbf{P}$ is a vector representing the power flow in each of the cartesian coordinates [48].

Chapter 3

The Multilayer Stack

Chapter 3 is concerned with the multilayer stack. The chapter focusses on the use of the transfer matrix in describing wave propagation in 1D systems and further considers the relationship between the transfer matrix and the scattering matrix.

The system under consideration in this work consists of a stratified composite of homogeneous, isotropic, parallel, welded plates with their respective normals pointing in the y-direction. The composite is periodic over a distance Λ that encompasses the unit cell which itself comprises two layers of differing elastic properties which are distinguished by the labels 1 and 2. The so-called multilayer stack (as shown in figure 3.1) is assumed infinite in each of the three Cartesian directions such that reflections from the outer boundary of the stack can be neglected.

3.1   The Analogy with the Diatomic Chain

Waves normally incident upon a multilayer stack that is periodic over two layers are completely analogous to waves propagating in the linear 1D diatomic chain, as shown in figure 3.2 [49], [50]. A diatomic chain consists of two masses M and m ($M > m$), which are assumed to be connected by identical, massless springs which have spring constants C. Assuming that each plane of atoms only interacts with its nearest neighbour plane of atoms, the equations of motion governing the respective masses become,

$$M\frac{d^2U_S}{dt^2} = C(u_S + u_{S-1} - 2U_S) \tag{3.1}$$
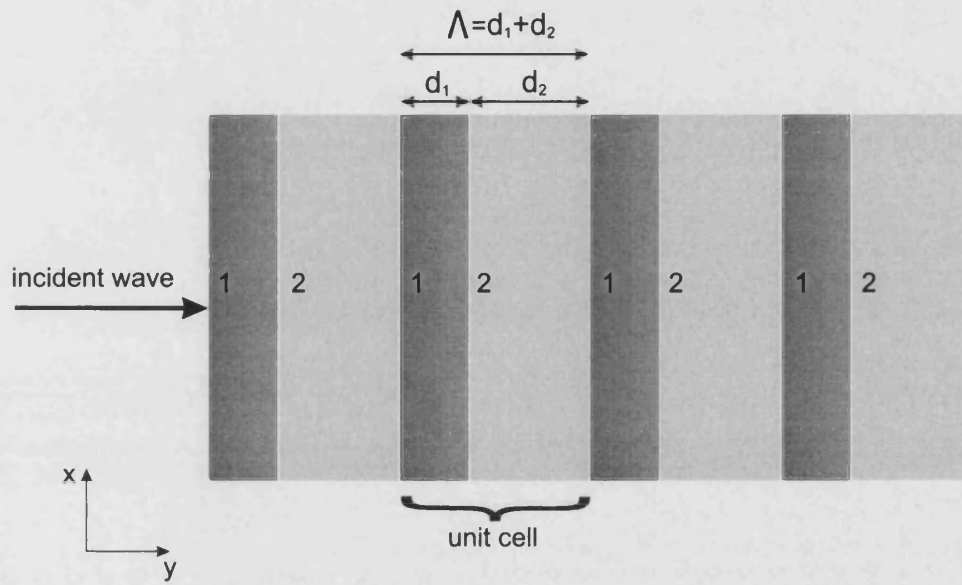
Figure 3.1: Cross-sectional view through the multilayer stack.
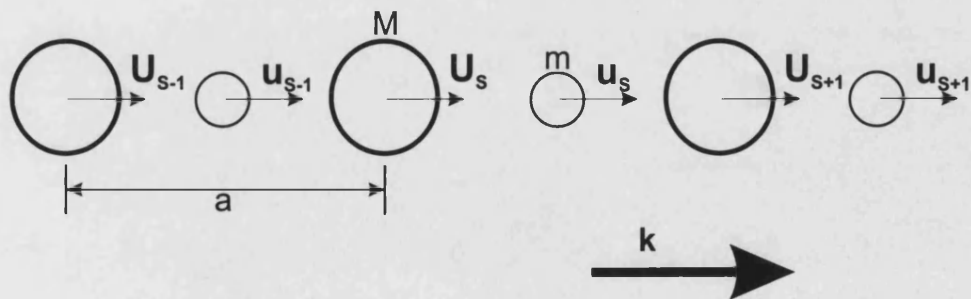
Figure 3.2: Diatomic chain with masses M and m connected by force constants C.

$$m\frac{d^2u_S}{dt^2} = C(U_{S+1} + U_S - 2u_S). \tag{3.2}$$

The dispersion of elastic waves propagating through such a system is strongly influenced by the wavevector **k**. The number of branches (i.e. curves) associated with the dispersion diagram of a given system is directly related to the number of degrees of freedom available to the system. Thus, for elastic waves propagating in a system which incorporates two masses (or layers, as compared with the multilayer stack) per unit cell and having N unit cells, there will be $6N$ degrees of freedom with $3N$ of these including the one L acoustic branch a two S acoustic branches, and the remainder taken up in the optical branches ("acoustic" and "optical" being terms used to describe the low and high frequency curves respectively).

For wavelengths that are long compared with the lattice constant a, i.e. the long wavelength limit, the relation between ω and k has been approximated by Kittel [50] as,

$$\omega^2 \cong 2C\left(\frac{1}{M} + \frac{1}{m}\right) \tag{3.3}$$

$$\omega^2 \cong \frac{C}{2(M+m)}k^2a^2 \tag{3.4}$$

which relate to the optical and acoustical branches respectively.

Similarly, for wavelengths which satisfy the condition $\lambda = 2a$, the dispersion is shown to be approximated by,

$$\omega^2 \cong \frac{2C}{m} \tag{3.5}$$

$$\omega^2 \cong \frac{2C}{M} \tag{3.6}$$

which again relate to the optical and acoustical branches, respectively.

The range of independent k vectors defined within these limits, i.e. the first Brillouin zone, $\frac{-\pi}{a} < k \le \frac{\pi}{a}$, completely describe the propagation of elastic waves in the system. The extrema values, $a \to 0$ and $|k| = \frac{\pi}{a}$, correspond to the elastic continuum and Brillouin zone boundary respectively and present significant differences to the propagation characteristics. For values of $|k| > \frac{\pi}{a}$, it is found that the elastic wave produces lattice motions that can be described with k vectors which reside within the first Brillouin

zone. This is a consequence of the lattice periodicity and is described in the next section.

3.2 Bloch's Theorem and the Transfer Matrix

The linearity of equation 2.18 ensures that any multiple of any solution to equation 2.18 is exactly the same solution, the multiplying factor simply determining the amount of a particular mode in the solution. In addition, the translational invariance of the multilayer stack in the y-direction implies that any field pattern (i.e. solution to equation 2.18) at position (x,y,z) within the stack, is nothing more than the same field pattern at position $(x,y+m\Lambda,z)$ where m is any integer, multiplied by some constant which may be complex (only positive propagation is considered here). This is a consequence of Bloch's Theorem [51] which in 1D systems is conveniently expressed in the form,

$$\mathbf{U}(x,y,z) = \mathbf{A}(x,y,z)\exp i(k_y y) \tag{3.7}$$

where $\mathbf{A}$ is a periodic function in y such that $\mathbf{A}(x,y,z) = \mathbf{A}(x,y \pm m\Lambda, z)$ and k_y is the Bloch wavevector.

The so-called *Bloch wave* $\mathbf{U}(x,y,z)$, is a complex, periodic, amplitude distribution with a period equal to the spacing of the stratification, and is simply the normal mode of the periodic system. The field of the Bloch wave can be represented as a set of interfering spatial harmonics ($\mathbf{a}_n$), as shown in equation 3.8, provided the resulting field pattern in the y-direction has a period that is consistent with the period of the system, Λ in this case [45]. To ensure this requirement, Bloch's theorem demands that the y-component of the wavevectors of the participating spatial harmonics are separated by integral amounts of the reciprocal lattice vector $G_L = \frac{2\pi}{\Lambda}$, such that,

$$\mathbf{U}(x,y,z) = \sum_m [\mathbf{a}_m(x,y,z)\exp(imG_L y)]\exp i(k_y^0 y) = \mathbf{A}(x,y,z)\exp i(k_y^0 y). \tag{3.8}$$

Here, k_y^0 is the y-component of the reduced wavevector that lies within the first Brillouin zone ($|k_y^0| \leq \frac{\pi}{\Lambda}$) of the reciprocal lattice and is the fundamental wavevector of the Bloch wave. Higher order zones are accessed through the addition of integer multiples m of the reciprocal lattice vector G_L, which correspond to higher order spatial harmonics

[52], as shown in equation 3.9.

$$k_y = k_y^0 + mG_L.$$ (3.9)

However, it is evident from equations 3.8 and 3.9 that any elastic wave propagating with a wavevector which lies outside the first Brillouin zone can be described with an equivalent wavevector which lies within the first Brillouin zone, since $\exp i(mG_L\Lambda) = 1$.

Bloch's result is evident on the wavevector diagram of a periodic system. In this case the wavevector diagram is a periodic array of the loci of real valued wavevectors separated by the reciprocal lattice vector G_L. As the frequency of the elastic waves is increased, the fundamental circle of radius $|\mathbf{k}^0|$ representing the spatial dispersion of elastic waves originating in the first Brillouin zone becomes penetrated by those circles representing the spatial dispersion of elastic waves originating in higher order zones. For sufficient contrast of the elastic properties of the layers of the unit cell, stop-bands are found to open up, which are separated by the reciprocal lattice vector [45], [52]. At exactly the Bragg condition (for the unit cell see equation 3.10), the elastic waves will be Bragg reflected from the unit cell and thus, will not propagate through the multilayer stack,

$$p_1 d_1 + p_2 d_2 = n\pi.$$ (3.10)

Here p_1 represents the component of the wavevector normal to the interfaces of the multilayer stack, in medium 1, and d_1 corresponds to the thickness of medium 1 of the unit cell etc.

For waves incident upon the stack with a β value in the range $|\mathbf{k}_1| > \beta > |\mathbf{k}_2|$ for example, the elastic wave will decay in layer 2 and if layer 2 is thin enough, the elastic wave will tunnel through to layer 1 in which the wave is real and propagating. Thus, if such a stack is allowed to reach equilibrium the elastic waves will become localised in alternate layers of the stack and will propagate along them harmonically.

For waves incident upon an interface within the stack with a β value which corresponds to a position within a stop-band, the elastic waves will be evanescent. The stop-bands are separated in k-space by the reciprocal lattice vector G_L, and so even for extremely strong density modulation across the layers of the stack, a frequency corresponding to a wavevector of at least $\frac{G_L}{2}$ is required in the associated media to grow a stop-band (see figure 3.3) [18], [52].
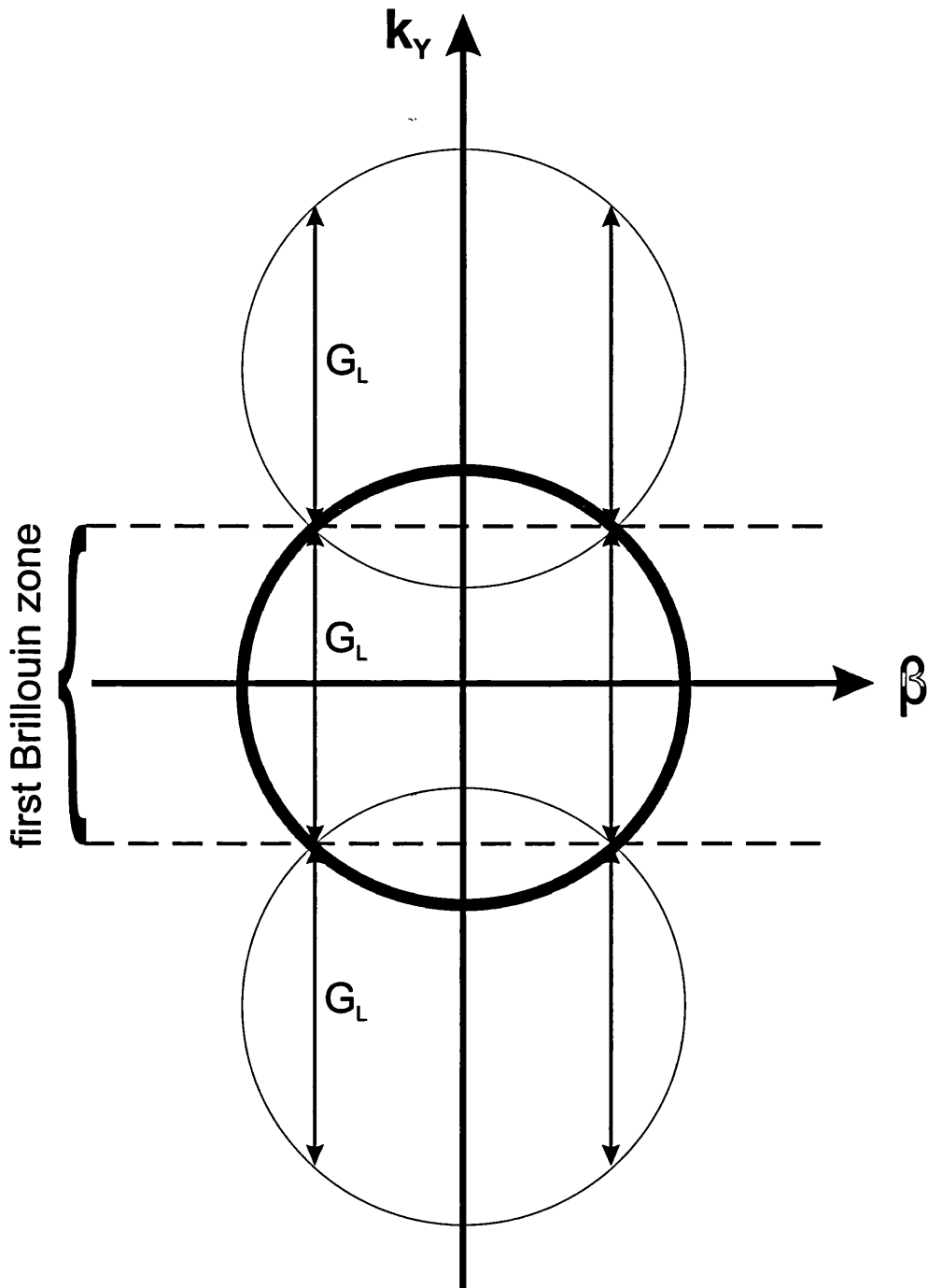
Figure 3.3: Wavevector diagram of anti-plane waves in a multilayer stack which is periodic over two layers that have similar elastic properties. For sufficiently strong contrast in elastic properties, stop-bands will develop at the Bragg condition separated by the reciprocal lattice vector G_L. The periodic nature of the system is evident along the y-axis, while the mirror symmetry in the y-axis demonstrates equivalent $\pm\beta$ propagation.

Formulating the Transfer Matrix

The transfer matrix is a useful tool in relating the field at any particular interface within a stratified composite to the field at any other interface or horizon within the structure. This is achieved through satisfying the boundary conditions at each interface. The technique has been applied to systems incorporating EM [18], [19], [20] and elastic waves [21], [22], [23], [24] in generating wavevector diagrams, dispersion diagrams and band edge plots (see chapters 4, 5, 6) and is further applied here in developing the understanding of elastic wave propagation in layered systems.

For a stack composed of elastic layers which are welded, the boundary conditions simply require the conservation of particle displacement (kinematic boundary condition) and stress tensor components normal to the interface (dynamic boundary condition). In this way the displacement of the wave can be mapped through the stack by analysing the displacement and stress components at each interface. Thus, the so-called *displacement-stress* vector at the beginning of the stack can be related to the displacement-stress vector at *any* interface.

The transfer matrix method is a special case of the eigenvalue problem where for some matrix $\mathbf{A}$, eigenmode $\mathbf{u}$ and eigenvalue l, the equation,

$$\mathbf{Au} = l\mathbf{u} \tag{3.11}$$

can be written. Now in considering the propagation of an elastic wave through the periodic stack, one must consider an eigenmode or simply a mode. Thus, following the application of the transfer matrix to a mode at some position within a particular unit cell of the stack, equation 3.11 requires the modulus of the eigenvalue to be unity if the same mode is to exist at an equivalent position in a neighbouring unit cell. With reference to 3.7 and without loss of generality, the eigenvalues can be expressed as $\exp(\pm ik_y\Lambda)$ [18].

Since the stack is periodic in the y-direction, a translation in either the positive or negative y-directions is equivalent to two Bloch waves, which differ only in the sign of the wavevector. Therefore, the transfer matrix as applied to a given mode will produce two eigenvalues corresponding to the forward and backward propagating waves and so will be the reciprocal of each other. It can be shown that if the product of eigenvalues of a given matrix is 1 then the determinant of the matrix must be one also. In short, for the propagation of a mode the transfer matrix must be unimodular. (In fact, the transfer matrix is a particular type of matrix - the Symplectic matrix - for which the

eigenvalues occur in pairs that are the reciprocal of one another).

3.2.1 Anti-Plane Polarised Waves

As previously stated in section 2.3, the displacement of an anti-plane wave is given by

$$\mathbf{U^{ap}} = \left(\frac{\partial \psi_y}{\partial x} - \frac{\partial \psi_x}{\partial y} \right) \hat{\mathbf{k}} \tag{3.12}$$

and the only stress tensor component which requires conserving at the interface is,

$$\tau_{23} = \mu \frac{\partial U_z}{\partial y}. \tag{3.13}$$

The anti-plane wave in layer j (j=1,2) of period N is described by the shear potential, which is composed of the incident component and the component reflected from the interface [39]. Thus, in satisfying the boundary conditions, solutions to equation 2.24 in layer j of period N are found to have the form,

$$\psi_j^N = \left(\psi_{Aj} \cos[p_{Sj}(y - y_j^N)] + \psi_{Bj} \sin[p_{Sj}(y - y_j^N)] \right) \exp -i(\beta x - \omega t) \tag{3.14}$$

where y_j^N represents the value of y at the beginning of the jth layer of period N, ψ_{Aj} and ψ_{Bj} are arbitrary complex coefficients and p_{Sj} the shear wavevector component normal to the interface in layer j. The use of trigonometric functions as opposed to exponential solutions is preferred since the former allow for an easier identification of the symmetric and antisymmetric modes (see section 6.1.2).

From equation 3.12, the anti-plane wave displacement in layer j of period N is given by,

$$U_{zj}^N = \psi_{Aj} \left(-i\beta \cos[p_{Sj}(y - y_j^N)] + p_{Sj} \sin[p_{Sj}(y - y_j^N)] \right) \exp -i(\beta x - \omega t) +$$

$$\psi_{Bj} \left(-i\beta \sin[p_{Sj}(y - y_j^N)] - p_{Sj} \cos[p_{Sj}(y - y_j^N)] \right) \exp -i(\beta x - \omega t) \tag{3.15}$$

and τ_{23} in layer j of period N is given by,

$$\tau_{23,j}^N = \psi_{Aj}\mu_j\left[i\beta p_{Sj}\sin[p_{Sj}(y-y_j^N)] + p_{Sj}^2\cos[p_{Sj}(y-y_j^N)]\right]\exp{-i(\beta x - \omega t)}+$$

$$\psi_{Bj}\mu_j\left[-i\beta p_{Sj}\cos[p_{Sj}(y-y_j^N)] + p_{Sj}^2\sin[p_{Sj}(y-y_j^N)]\right]\exp{-i(\beta x - \omega t)} \qquad (3.16)$$

where μ_j is the shear modulus in layer j.

The matrix propagator for the entire period, i.e. the relation between the displacement-stress vector at the beginning of layer j in period N to the displacement-stress vector at the equivalent position in layer $N+1$ [18], [19], is determined by the product of matrices $\mathbf{M_{j+1}.M_j} = \mathbf{M_P^{ap}}$, where $\mathbf{M_j}$ represents the matrix propagator across layer j of the period etc. The elements of $\mathbf{M_P^{ap}}$ are given below in matrix 3.17.

$$\begin{pmatrix} \cos(d_1p_{S1})\cos(d_2p_{S2}) - \frac{\sin(d_1p_{S1})\sin(d_2p_{S2})}{p_{S2}\mu_2} & \frac{\sin(d_1p_{S1})\cos(d_2p_{S2})}{p_{S1}\mu_1} + \frac{\cos(d_1p_{S1})\sin(d_2p_{S2})}{p_{S2}\mu_2} \\ -\cos(d_1p_{S1})\cos(d_2p_{S2})p_{S1}\mu_1 & \cos(d_1p_{S1})\cos(d_2p_{S2}) - \frac{\sin(d_1p_{S1})\cos(d_2p_{S2})}{p_{S1}\mu_1} \end{pmatrix}.$$
$$(3.17)$$

Thus,

$$\begin{pmatrix} U_z \\ \tau_{23} \end{pmatrix}_j^{N+1} = \mathbf{M_P^{ap}}\begin{pmatrix} U_z \\ \tau_{23} \end{pmatrix}_j^N. \qquad (3.18)$$

The unimodular property of the matrix propagator is exploited in analysing the propagation characteristics of the waves in question, in this case the anti-plane waves. Referring to equation 3.8 and 3.18, it follows that for the propagation of a mode, i.e. a Bloch wave,

$$\begin{pmatrix} A & B \\ C & D \end{pmatrix}\begin{pmatrix} U_z \\ \tau_{23} \end{pmatrix}_j^N = \exp(ik_{Sy}^0\Lambda)\begin{pmatrix} U_z \\ \tau_{23} \end{pmatrix}_j^N \qquad (3.19)$$

where A, B, C and D represent those elements of $\mathbf{M_P^{ap}}$ (equation 3.17) and k_{Sy}^0 is the Bloch wavevector of the S waves. The phase factor, $\exp(ik_{Sy}^0\Lambda)$, is nothing more than an eigenvalue of the matrix propagator $\mathbf{M_P^{ap}}$ and so the dispersion relation for anti-plane waves is obtained when the following condition is satisfied,

$$det\left(\mathbf{M_P^{ap}} - \mathbf{I}\exp(ik_{Sy}^0\Lambda)\right) = 0, \tag{3.20}$$

where $\mathbf{I}$ is a 2×2 identity matrix.

The unimodular property of the matrix propagator ensures that the product of eigenvalues is 1. Therefore, the eigenvalues of $\mathbf{M_P^{ap}}$ will be the reciprocal of each other and can be written in general terms as,

$$\exp(\pm ik_{Sy}^0\Lambda) = \frac{1}{2}(A+D) \pm \left(\left[\frac{1}{2}(A+D)\right]^2 - 1\right)^{\frac{1}{2}}. \tag{3.21}$$

In solving equation 3.20, the relation between ω, β and k_{Sy}^0 is found to be,

$$k_{Sy}^0 = \frac{1}{\Lambda}\arccos\left(\frac{1}{2}(A+D)\right). \tag{3.22}$$

Regimes where $|\frac{1}{2}(A+D)| < 1$ correspond to real k_{Sy}^0 and thus to propagating Bloch waves. However, when $|\frac{1}{2}(A+D)| > 1$, the Bloch wavevector $k_{Sy}^0 = \frac{\pi}{\Lambda} + ik_{iSy}^0$, will have an imaginary component k_{iSy}, and so the Bloch wave will be evanescent. This condition relates to the so-called forbidden bands of the periodic medium, the edges of which are located at positions determined when $|\frac{1}{2}(A+D)| = 1$ [18]. Given this relationship (equation 3.22) between ω, β and k_{Sy}^0, wavevector diagrams, dispersion curves and band edge diagrams can be explored.

3.2.2 In-Plane Polarised Waves

As before, the L and S potentials must satisfy the respective wave equation in each layer of the stack. In satisfying the wave equations 2.23 and 2.24, the L potential in layer j is found to have the form,

$$\phi_j^N = [\phi_{Aj}\cos(p_{Lj}(y-y_j^N)) + \phi_{Bj}\sin(p_{Lj}(y-y_j^N))]\exp-i(\beta x - \omega t) \tag{3.23}$$

and the S potential,

$$\psi_{zj}^N = [\psi_{Aj} \cos(p_{Sj}(y - y_j^N)) + \psi_{Bj} \sin(p_{Sj}(y - y_j^N))] \exp{-i(\beta x - \omega t)} \qquad (3.24)$$

where p_{Lj} represents the L wavevector component normal to the interface in layer j, and ϕ_{Aj} and ϕ_{Bj} are arbitrary complex coefficients of the L waves within layer j. This situation is complicated by the coupling of the two polarisation states at the interfaces between the layers 1 and 2. The total displacement of the medium in layer j is given by,

$$\mathbf{U_j^{ip}} = \left(\frac{\partial \phi_j}{\partial x} + \frac{\partial \psi_{zj}}{\partial y}\right)\hat{\mathbf{i}} + \left(\frac{\partial \phi_j}{\partial y} - \frac{\partial \psi_{zj}}{\partial x}\right)\hat{\mathbf{j}} \qquad (3.25)$$

and the stress components which require conserving at the interface in layer j are,

$$\tau_{21,j} = \mu_j \left(\frac{\partial U_{yj}}{\partial x} + \frac{\partial U_{xj}}{\partial y}\right) \qquad (3.26)$$

and

$$\tau_{22,j} = \lambda_j \frac{\partial U_{xj}}{\partial x} + (\lambda_j + 2\mu_j)\frac{\partial U_{yj}}{\partial y}. \qquad (3.27)$$

Thus, it is obvious for this system four boundary conditions need satisfying which indicates that the matrix propagator will involve sixteen terms as compared to the previous case of four [39]. It is also evident that neither the L nor the SV wave excites a tensor component in the z-direction and so no SH component will be produced.

Upon splitting 3.25 into its constituent x and y-components, the x-displacement in layer j of period N of the stack can be written as,

$$U_{xj}^N = [-i\beta\phi_{Aj}\cos(p_{Lj}(y - y_j^N)) - i\beta\phi_{Bj}\sin(p_{Lj}(y - y_j^N))$$

$$-p_{Sj}\psi_{Aj}\sin(p_{Sj}(y - y_j^N)) + p_{Sj}\psi_{Bj}\cos(p_{Sj}(y - y_j^N))]\exp{-i(\beta x - \omega t)}. \qquad (3.28)$$

Similarly, for the y-component and the two stress components, it is found that

$$U_{yj}^{N} = [-p_{Lj}\phi_{Aj}\sin(p_{Lj}(y-y_{j}^{N})) + p_{Lj}\phi_{Bj}\cos(p_{Lj}(y-y_{j}^{N}))$$

$$+i\beta\psi_{Aj}\cos(p_{Sj}(y-y_{j}^{N})) + i\beta\psi_{Bj}\sin(p_{Sj}(y-y_{j}^{N}))]\exp-i(\beta x - \omega t), \qquad (3.29)$$

$$\tau_{21,j}^{N} = [2i\beta p_{Lj}\mu_{j}\phi_{Aj}\sin(p_{Lj}(y-y_{j}^{N})) - 2i\beta p_{Lj}\mu_{j}\phi_{Bj}\cos(p_{Lj}(y-y_{j}^{N}))$$

$$+(\beta^{2}-p_{Sj}^{2})\mu_{j}\psi_{Aj}\cos(p_{Sj}(y-y_{j}^{N})) + (\beta^{2}-p_{Sj}^{2})\mu_{j}\psi_{Bj}\sin(p_{Sj}(y-y_{j}^{N}))]\exp-i(\beta x - \omega t)$$

$$(3.30)$$

and

$$\tau_{22,j}^{N} = [(\beta^{2}-p_{Sj}^{2})\mu_{j}\phi_{Aj}\cos(p_{Lj}(y-y_{j}^{N})) + (\beta^{2}-p_{Sj}^{2})\mu_{j}\phi_{Bj}\sin(p_{Lj}(y-y_{j}^{N}))$$

$$-2i\beta p_{Sj}\mu_{j}\psi_{Aj}\sin(p_{Sj}(y-y_{j}^{N})) + +2i\beta p_{Sj}\mu_{j}\psi_{Bj}\cos(p_{Sj}(y-y_{j}^{N}))]\exp-i(\beta x - \omega t).$$

$$(3.31)$$

In formulating the matrix propagator for the coupled system, it is found that the matrix is most useful if the displacement-stress vector is conserved across each layer of the stack in the format, $(U_{x}U_{y}\tau_{21}\tau_{22})_{j}^{T}$, where T indicates the transpose operation. Whilst the symmetry of the elements in the off diagonal is evident in the matrix propagator for each individual layer, the symmetry in the matrix propagator for the whole period is only obtained at normal incidence, $\beta = 0$. However, the determinant of the matrix across the period is unity and so the analysis of the coupled waves proceeds in a similar manner to anti-plane waves.

Since the determinant of the matrix propagator for coupled waves is 1, the product of eigenvalues for the matrix propagator will be 1 also. However, for coupled waves the matrix propagator will produce four eigenvalues which can be expressed as $\exp\pm(ik_{Ly}^{0}\Lambda)$ and $\exp\pm(ik_{Sy}^{0})$, where k_{Ly}^{0} and k_{Sy}^{0} can be considered to be the Bloch wavevector of the L and S waves, respectively. Thus, proceeding in a similar manner to that described in the previous section, the dispersion relation for coupled waves is determined when,

$$det\left(\mathbf{M}_{\mathbf{P}}^{\mathbf{ip}} - \mathbf{I}\exp\pm(ik_{(L,S)y}^{0})\right) = 0, \qquad (3.32)$$

where $\mathbf{I}$ is a 4×4 identity matrix, and $\mathbf{M}_{\mathbf{P}}^{\mathbf{ip}}$ is the matrix propagator for coupled waves, the elements of which are given in appendix A. Therefore, wavevector diagrams, dis-

person curves and band edge plots for coupled L and S waves can be generated using equation 3.32.

3.3 Normalised Parameters

In modelling elastic waves in a multilayer stack, it is convenient to use a set of normalised parameters. In specifying Λ, c_{L1} and ρ_1 as characteristic of the length, speed (in medium 1) and mass (density per unit volume of medium 1) respectively, any physical property of the stack can expressed through various combinations of these parameters.

The normalised parameters include a normalised frequency ν, a set of normalised wavevectors, κ, b and q, a relative layer thickness t_1, a density ratio ρ_R, and a set of elastic indexes, n_{L2}, n_{S1} and n_{S2} as defined below.

$$\omega = \frac{\nu c_{L1}}{\Lambda}, \mathbf{k} = \frac{\kappa}{\Lambda}, \beta = \frac{b}{\Lambda}, p = \frac{q}{\Lambda}$$

$$t_1 = \frac{d_1}{\Lambda}, (1 - t_1) = \frac{d_2}{\Lambda}, \rho_R = \frac{\rho_2}{\rho_1} \tag{3.33}$$

$$n_{L2} = \frac{c_{L2}}{c_{L1}}, n_{S1} = \frac{c_{S1}}{c_{L1}}, n_{S2} = \frac{c_{S2}}{c_{L1}}$$

3.4 The Scattering Matrix

The scattering matrix relates the waves incident from infinity on a scattering system to the waves going away to infinity. The elements of the scattering matrix have a particular meaning depending on the type of wave incident upon and departing from the interface and include the reflection and transmission coefficients [39]. In calculating these coefficients for a multilayer stack (or any other scattering system), it is sufficient to consider the system as a "black box", which is only characterised by its matrix propagator $\mathbf{M}$, since the latter is easily related to the scattering matrix.

If one considers the situation depicted in figure 3.4, with the waves incident from infinity upon the stack as represented through subscript a, and those propagating toward infinity through subscript b, then the anti-plane wave field components across
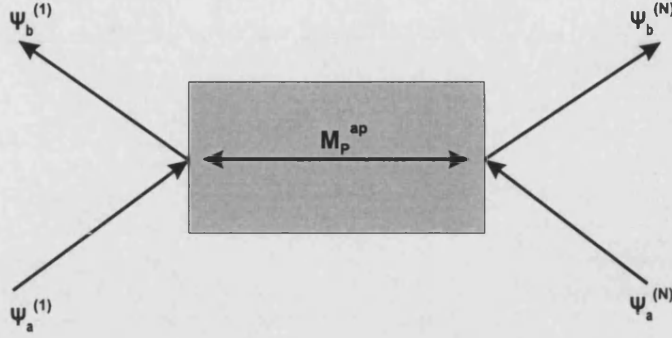
Figure 3.4: Schematic illustration of the notation used in formulating the scattering matrix. Here the multilayer stack is considered as a black box.

the stack from period 1 to period N, can be written as,

$$\mathbf{L} \begin{pmatrix} \psi_a^N \\ \psi_b^N \end{pmatrix} = \mathbf{M}.\mathbf{L} \begin{pmatrix} \psi_a^1 \\ \psi_b^1 \end{pmatrix} \qquad (3.34)$$

where matrix $\mathbf{L}$ relates the potentials to the physical displacements and stresses.

Now, the scattering matrix, $\mathbf{S}$ has the relation [21]

$$\begin{pmatrix} \psi_b^1 \\ \psi_b^N \end{pmatrix} = \mathbf{S} \begin{pmatrix} \psi_a^1 \\ \psi_a^N \end{pmatrix} \qquad (3.35)$$

and so expanding and re-grouping the terms in equation 3.34 in such a way as to construct equation 3.35, it is found that,

$$\mathbf{N_b^{ap}} \begin{pmatrix} \psi_b^1 \\ \psi_b^N \end{pmatrix} = \mathbf{N_a^{ap}} \begin{pmatrix} \psi_a^1 \\ \psi_a^N \end{pmatrix}. \qquad (3.36)$$

Here,

$$\mathbf{N_b^{ap}} = \begin{pmatrix} -h_{12} & 1 \\ -h_{22} & 0 \end{pmatrix} ; \mathbf{N_a^{ap}} = \begin{pmatrix} h_{11} & 0 \\ h_{21} & -1 \end{pmatrix} \qquad (3.37)$$

where h_{ij} is element (i,j) of the matrix $\mathbf{H} = \mathbf{L}^{-1}.\mathbf{M}.\mathbf{L}$. Similarly, for the in-plane polarised waves, it is found that

$$\mathbf{N}_{b}^{ip}\begin{pmatrix}\phi_{b}^{1}\\\phi_{b}^{N}\\\psi_{b}^{1}\\\psi_{b}^{N}\end{pmatrix}=\mathbf{N}_{a}^{ip}\begin{pmatrix}\phi_{a}^{1}\\\phi_{a}^{N}\\\psi_{a}^{1}\\\psi_{a}^{N}\end{pmatrix}\tag{3.38}$$

where,

$$\mathbf{N}_{b}^{ip}=\begin{pmatrix}-h_{12}&1&-h_{14}&0\\-h_{22}&0&-h_{24}&0\\-h_{32}&0&-h_{34}&1\\-h_{42}&0&-h_{44}&0\end{pmatrix};\mathbf{N}_{a}^{ip}=\begin{pmatrix}h_{11}&0&h_{13}&0\\h_{21}&-1&h_{23}&0\\h_{31}&0&h_{33}&0\\h_{41}&0&h_{43}&-1\end{pmatrix}.\tag{3.39}$$

For both the anti-plane and in-plane polarised waves, the scattering matrix is given by [39],

$$\mathbf{S}=(\mathbf{N_{b}})^{-1}.\mathbf{N_{a}}\tag{3.40}$$

where $\mathbf{N}$ relates to the anti-plane or in-plane polarised waves.

3.4.1 Amplitude Scattering Coefficients

The scattering matrix obtained in the previous section provides a collective account of all the reflection and transmission coefficients of the physical displacements of the elastic waves. The coefficients take the same form as that for the potentials but scale differently. The magnitude of the L wave in layer j is given by $|U_{Lj}| = k_{Lj}\phi_{j}$, and similarly, that for the S wave is $|U_{Sj}| = k_{Sj}\psi_{j}$ (see equations 2.19 and 2.20). The scattering matrix for the amplitudes of in-plane waves ($\mathbf{S}_{A}^{ip}$) can be written explicitly in terms of the scattering matrix for the potentials and this is shown here to illustrate the scaling factors involved in this transformation.

$$\mathbf{S}_{A}^{ip}=\begin{pmatrix}V_{LL}&\frac{|k_{Lj}|}{|k_{L(j+1)}|}\tilde{T}_{LL}&\frac{|k_{Lj}|}{|k_{Sj}|}V_{SL}&\frac{|k_{Lj}|}{|k_{S(j+1)}|}\tilde{T}_{SL}\\\frac{|k_{L(j+1)}|}{|k_{Lj}|}T_{LL}&\tilde{V}_{LL}&\frac{|k_{L(j+1)}|}{|k_{Sj}|}T_{SL}&\frac{|k_{L(j+1)}|}{k_{S(j+1)}|}\tilde{V}_{SL}\\\frac{|k_{Sj}|}{|k_{Lj}|}V_{LS}&\frac{|k_{Sj}|}{|k_{L(j+1)}|}\tilde{T}_{LS}&V_{SS}&\frac{|k_{Sj}|}{|k_{S(j+1)}|}\tilde{T}_{SS}\\\frac{|k_{S(j+1)}|}{|k_{Lj}|}T_{LS}&\frac{|k_{S(j+1)}|}{|k_{L(j+1)}|}\tilde{V}_{LS}&\frac{|k_{S(j+1)}|}{|k_{Sj}|}T_{SS}&\tilde{V}_{SS}\end{pmatrix}.\tag{3.41}$$

V and T are the reflection and transmission coefficients of the potentials respectively, such that V_{LS} corresponds to the reflection of an L wave into an S wave in layer j and $\tilde{T}_{SL}$ corresponds to the excitation of an L wave in medium j from an S wave incident in layer $(j+1)$; the tilde denotes incidence from layer $(j+1)$ [39].

3.4.2 Scattering Coefficients of Energy

The energy flow associated with an elastic wave was shown in section 2.4 to be dependant on the velocity vector of the elastic wave and the stress tensor. In considering the re-distribution of energy associated with an elastic wave that impinges upon a scattering system, the detail of the interaction is obtained through the consideration of the energy flow normal to the interfaces.

Now, if we are to make use of the matrix propagator, the scattering matrix for the power flow must relate to linear potentials. This distinction is made since the power associated with a given elastic wave is, of course, related to the square modulus of the respective potential [39], [48]. However, the matrix propagator does not operate on squared potentials. Initially therefore, the analysis proceeds with the consideration of the square root of power.

The "root power" for L and S waves incident upon a scattering system (subscript a) is given below in terms of the respective potentials,

$$
\underbrace{\begin{pmatrix} \sqrt{P_1^L} \\ \sqrt{P_2^L} \\ \sqrt{P_1^S} \\ \sqrt{P_2^S} \end{pmatrix}_a}_{\sqrt{P_a}} = \frac{1}{2} \underbrace{\begin{pmatrix} (\omega\mu_1 p_{L1} k_{S1}^2)^{\frac{1}{2}} & 0 & 0 & 0 \\ 0 & (\omega\mu_2 p_{L2} k_{S2}^2)^{\frac{1}{2}} & 0 & 0 \\ 0 & 0 & (\omega\mu_1 p_{S1} k_{S1}^2)^{\frac{1}{2}} & 0 \\ 0 & 0 & 0 & (\omega\mu_2 p_{S2} k_{S2}^2)^{\frac{1}{2}} \end{pmatrix}}_{R_a} \underbrace{\begin{pmatrix} \phi_1 \\ \phi_2 \\ \psi_1 \\ \psi_2 \end{pmatrix}_a}_{\Phi_a}.
$$

$$(3.42)$$

Similarly, for waves departing the scattering system, the relevant relationship between "root power" and potential is obtained by replacing a for b in equation 3.42. Thus, for in-plane polarised waves incident upon a scattering system, characterised only by its scattering matrix $\mathbf{S}$ (which is itself derived from the matrix propagator), the "root power" distribution through the system can be written as,

$$
\left(\sqrt{\mathbf{P_b}}\right) = \underbrace{(\mathbf{R_b})^{-1}.\mathbf{S}.\mathbf{R_a}}_{\sqrt{\mathbf{S^P}}} \cdot \sqrt{\mathbf{P_a}}.
$$

$$(3.43)$$

The actual power departing the system $\mathbf{P_b}$, is obtained by multiplying $\sqrt{\mathbf{P_b}}$ by $\sqrt{\mathbf{P_b}}^T$, and so the actual reflectance and transmittance coefficients are revealed through the matrix $\mathbf{S^P}$ which is given below.

$$\mathbf{P_b} = \left(\sqrt{\mathbf{P_a}}\right)^T . \underbrace{(\sqrt{\mathbf{S^P}})^T . \sqrt{\mathbf{S^P}}}_{\mathbf{S^P}} . \sqrt{\mathbf{P_a}} \qquad (3.44)$$

The above equation is, of course, nothing more than a statement of the conservation of energy and so we can write,

$$(\mathbf{S^P})^T . \mathbf{S^P} = \mathbf{I}. \qquad (3.45)$$

Chapter 4

The Wavevector Diagram

Chapter 4 introduces the concept of the wavevector diagram, which is used to illustrate the spatial dispersion of elastic waves in 1D systems.

The wavevector diagrams showing the propagation characteristics of anti-plane and in-plane polarised elastic waves in a periodic multilayer stack having a unit cell incorporating a type I interface (i.e. $c_{L1} > c_{L2} > c_{S1} > c_{S2}$) are shown in figures 4.1-4.4. The circular construction lines (described in section 2.3.2) of the figures are included for guidance and to contrast elastic wave propagation in the multilayer stack with elastic wave propagation in bulk media.

The analysis of this type of interface has been arbitrarily chosen. It is to be understood that the generation of wavevector diagrams for multilayer stacks incorporating a type II or type III interface can be obtained in an identical manner to the following.

4.1   Anti-Plane Polarised Waves

Anti-plane polarised wave propagation in a multilayer stack is shown in figure 4.1 as a function of increasing wave frequency. Each plot is constructed from equation 3.20, which expresses the eigenvalues of the transfer matrix for anti-plane waves in terms of an exponential function of the Bloch wavevector.

The eigenvalues of the transfer matrix are functions of frequency (ω) and wavevector for the S (k_S) waves in each layer of the unit cell. By choosing an operating frequency, and fixing the phase velocity for the waves in each layer of the unit cell so that they

relate to the desired materials, the plot can be constructed by varying the variable β and solving the resulting equation for real valued Bloch wavevectors. As with any computer generated result, the term "real valued" will be a relative value; the Bloch wavevector will typically always have an imaginary component. Therefore, for the purposes of defining a real valued wavevector, the solutions of equation 3.20 which had an imaginary component of magnitude $< 10^{-10}$ were taken as being real.

For the system shown in figure 4.1, the density contrast between the layers was arbitrarily chosen to be $\rho_R = 0.898$ and the relative layer thickness was chosen to be $t_1 = 0.59$. It has been shown by Boumaiza [53] that porous silicon films can be grown having a periodic density modulation. In the circumstances, multilayer stacks formed of porous silicon having a periodic variation in porosity seem an attractive material in which to test the underlying theory of elastic waves in periodic composites since a large, tailored variation in density contrast is possible.

The speed of the S waves in each layer of the unit cell was expressed using elastic indexes ($n_{S1} = 1.75$, $n_{S2} = 2.0$) in accordance with the relations shown in equation 3.33. The reference speed was taken to be the speed of L waves in bulk silica (5960m/s) since photonic crystal fibre is manufactured using silica, and it is photonic crystal fibre which forms the basis of part II of this thesis. Accordingly, layer 1 of the unit cell was assumed to be silica and the density and acoustic phase velocities of the waves in layer 2 were varied in an attempt to understand the effect of unit cell make-up on elastic wave propagation.

Referring to figure 4.1, for frequencies which create wavevectors of magnitude less than $\frac{G_L}{2}$ (as seen in figure 4.1a), no stop-bands develop and the propagation is similar to propagation in bulk media. In this regime the wavelengths of the elastic waves are much longer than the thickness of either layer of the unit cell and accordingly, the waves see an effective medium with mechanical properties intermediate to the properties of the separate layers of the unit cell. However, as seen in figure 4.1a, the propagation demonstrates a small amount of anisotropy, as revealed through the slightly elongate central region [54].

As the frequency is increased, the waves propagating in the first Brillouin zone develop into adjacent zones and *vice versa*, with stop-bands developing at the Brillouin zone boundary $|k_y| = \frac{\pi}{\Lambda}$, due to the Bragg condition [45], [52]. As the frequency is further increased, stop-bands also begin to develop at the zone centre as shown in figure 4.1e. In all cases the stop-bands are separated along the y-direction by the reciprocal lattice vector.

The group velocity of the waves is given by $\nabla_k \omega(\mathbf{k})$ and points in the direction of

increasing wave frequency. At the stop-band edge the group velocity points in the direction of β and so the energy flow is along the layers of the unit cell.

The width of the stop-band is largely dependent on the density contrast between the two media of the unit cell, although the relative thickness of the layers of the unit cell also has an influence (see [18] for the optical analogue). As $t_1 \to 0$ the waves begin to take on characteristics indicative of medium 2 and similarly as $t_1 \to 1$ the stack essentially becomes a homogeneous, isotropic body of medium 1. These extreme cases correspond the propagation of elastic waves in effectively a single medium in which the periodicity of the system becomes lost. Conversely, values of t_1 intermediate these extremes will produce a periodic system and so will influence the propagation of elastic waves.

The effect of density contrast on stop-band width is shown in figure 4.2 for decreasing values of $\rho_R = \frac{\rho_2}{\rho_1}$. As the density contrast increases, the stop-band width is seen to increase whereupon at a given contrast ratio ($\rho_R < 0.5$) and for a given set of operating conditions, the energy flow associated with the elastic waves is essentially along the layers of the system with little or no energy passing through the system.

4.2 In-Plane Polarised Waves

The wavevector diagram illustrating the spatial dispersion of in-plane polarised coupled waves in a multilayer stack having an identical composition to that analysed in the previous section, is illustrated in figure 4.3 as a function of increasing wave frequency. This diagram was constructed in an analogous manner to that for anti-plane polarised waves except in this case the eigenvalues of the transfer matrix for in-plane polarised waves were used, namely equation 3.32. In addition, the elastic indexes for the L waves were chosen to be $n_{L1} = 1.0$ and $n_{L2} = 1.25$.

Referring to figure 4.3, stop-bands for in-plane polarised waves can be seen to develop at the Brillouin zone boundary in a similar fashion to anti-plane polarised waves. The coupled waves differ from the anti-plane waves though in that stop-bands also develop in regions where the L and S circles intersect - figure 4.3c. These stop-bands are analogous to those at the Brillouin zone boundary and are also separated along the y-axis by the reciprocal lattice vector G_L. However, these "coupled wave" stop-bands appear to differ from those at the Brillouin zone boundary in that as the wave frequency increases, their width decreases to zero, as shown in figures 4.3c-e.

The effect of density contrast on the stop-band width is also shown for coupled waves

Figure 4.1: Wavevector diagram for anti-plane polarised waves propagating in a multilayer stack defined by $\rho_R = 0.898, t_1 = 0.59$. The spatial dispersion (bold line) and stop-band development are shown for increasing frequency (normalised); (a) $\nu = 1$, (b) $\nu = 1.7$, (c) $\nu = 2.4$, (d) $\nu = 3.4$, (e) $\nu = 4.2$.

Figure 4.2: Wavevector diagram for anti-plane polarised waves propagating in a multi-layer stack, defined by $t_1 = 0.59$, with a normalised frequency of $\nu = 2.4$. The spatial dispersion (bold line) and stop-band development are shown for decreasing density ratio ρ_R; (a) $\rho_R = 0.8$, (b) $\rho_R = 0.6$, (c) $\rho_R = 0.5$, (d) $\rho_R = 0.4$, (e)$\rho_R = 0.2$.

in figure 4.4. As the density contrast is increased, the stop-band width is also found to increase, similar to the anti-plane waves. Moreover, the coupled L and S waves begin to propagate in regions beyond the scope of conventional L and S waves. See figures 4.4c - 4.4e for example; the S waves of figure 4.4e propagate in regions of k-space outside the boundary of the S circles. For sufficiently large density contrast, the S waves that are localised in alternate layers of the multilayer stack propagate along the layers in a manner similar to flexural waves on a free plate (analogous to waves on a skipping rope - see section 11.1) with a phase velocity that is less than the phase velocity of S waves in bulk media and thus have a larger wavevector.
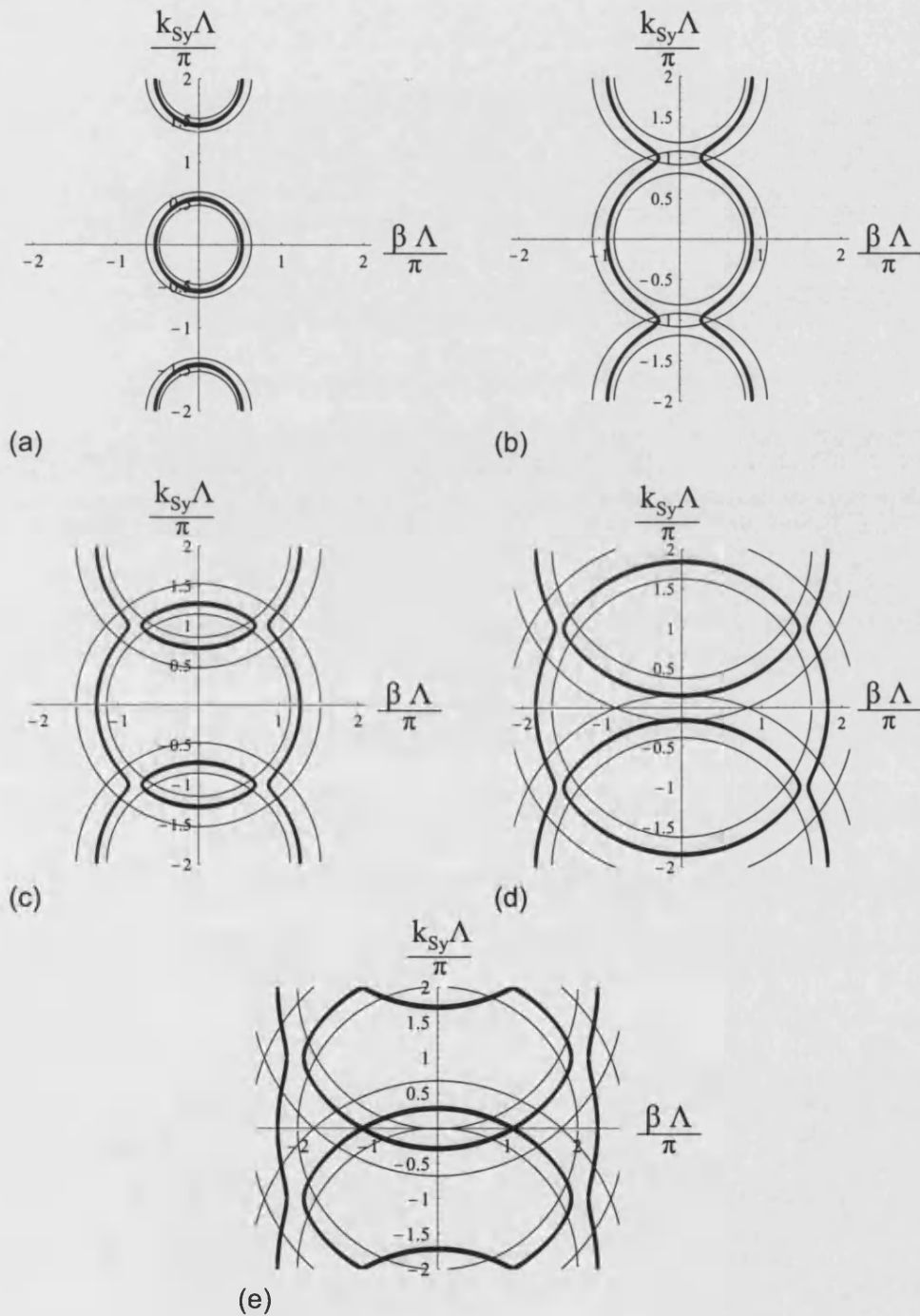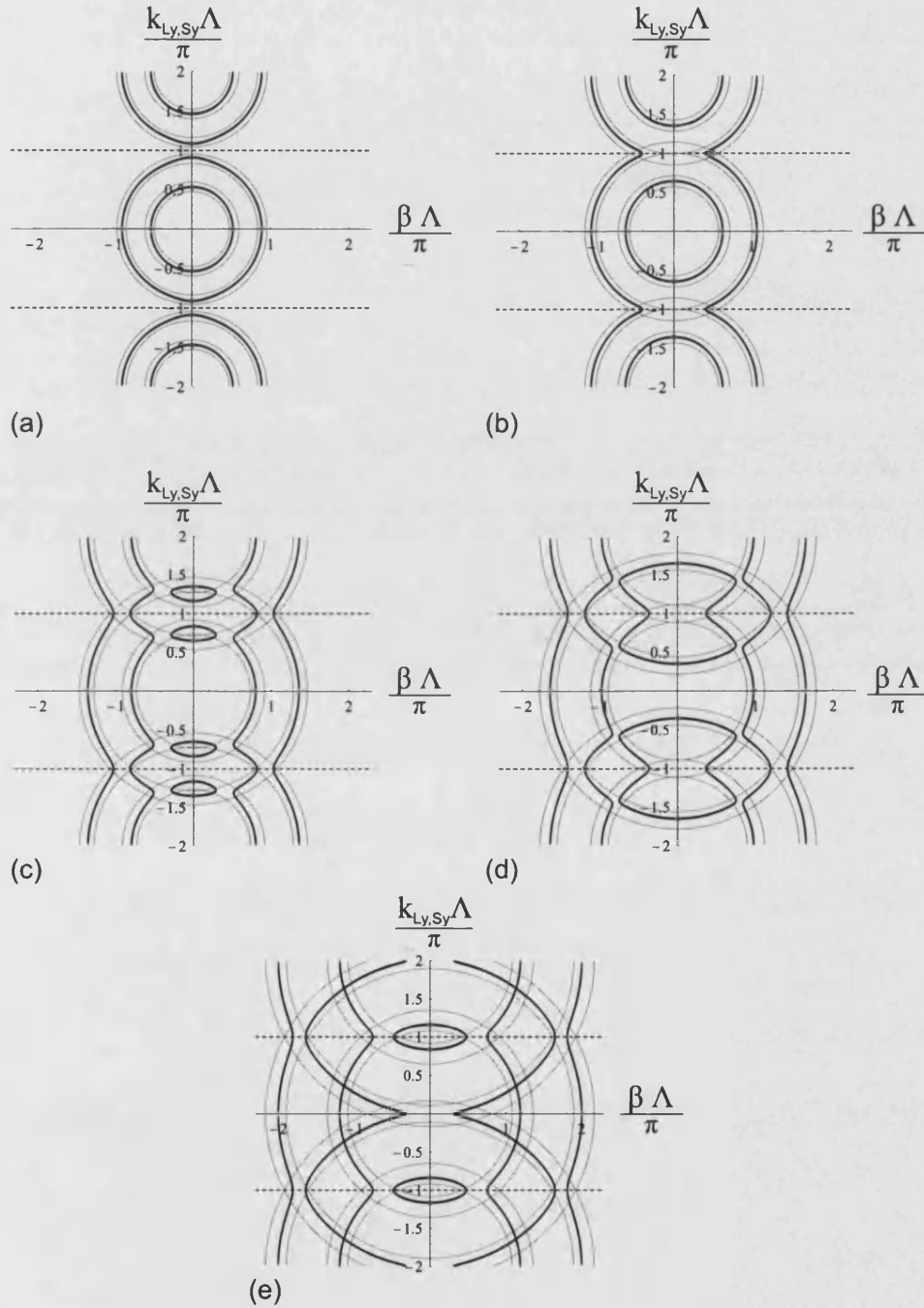
Figure 4.3: Wavevector diagram for in-plane polarised waves propagating in a multi-layer stack defined by $\rho_R = 0.898$ and $t_1 = 0.59$. The spatial dispersion (bold line) and stop-band development are shown for increasing frequency (normalised); (a) $\nu = 1.5$, (b) $\nu = 1.8$, (c) $\nu = 2.3$, (d) $\nu = 2.8$, (e) $\nu = 3.1$. The first Brillouin zone is shown bounded by dashed lines.

46

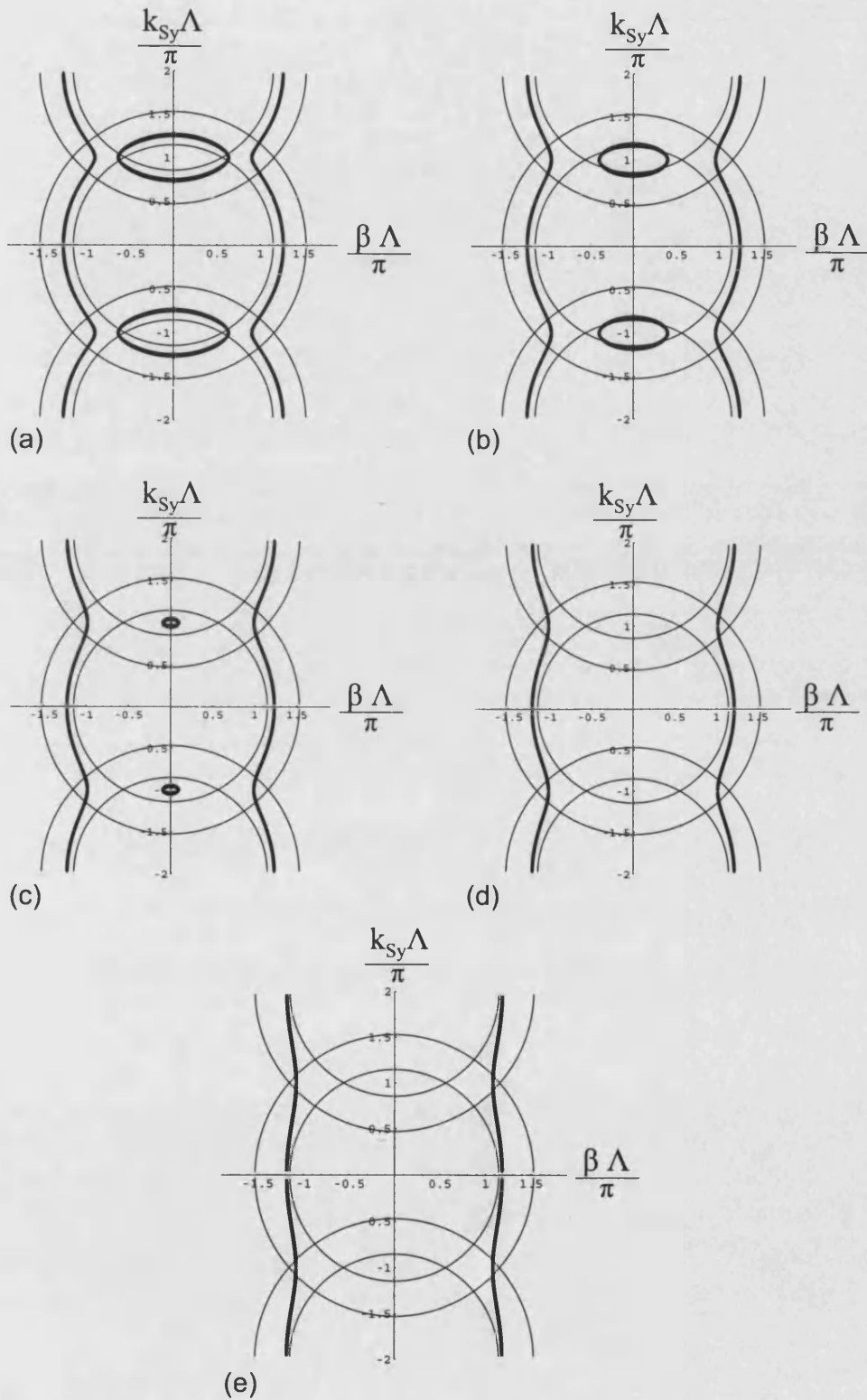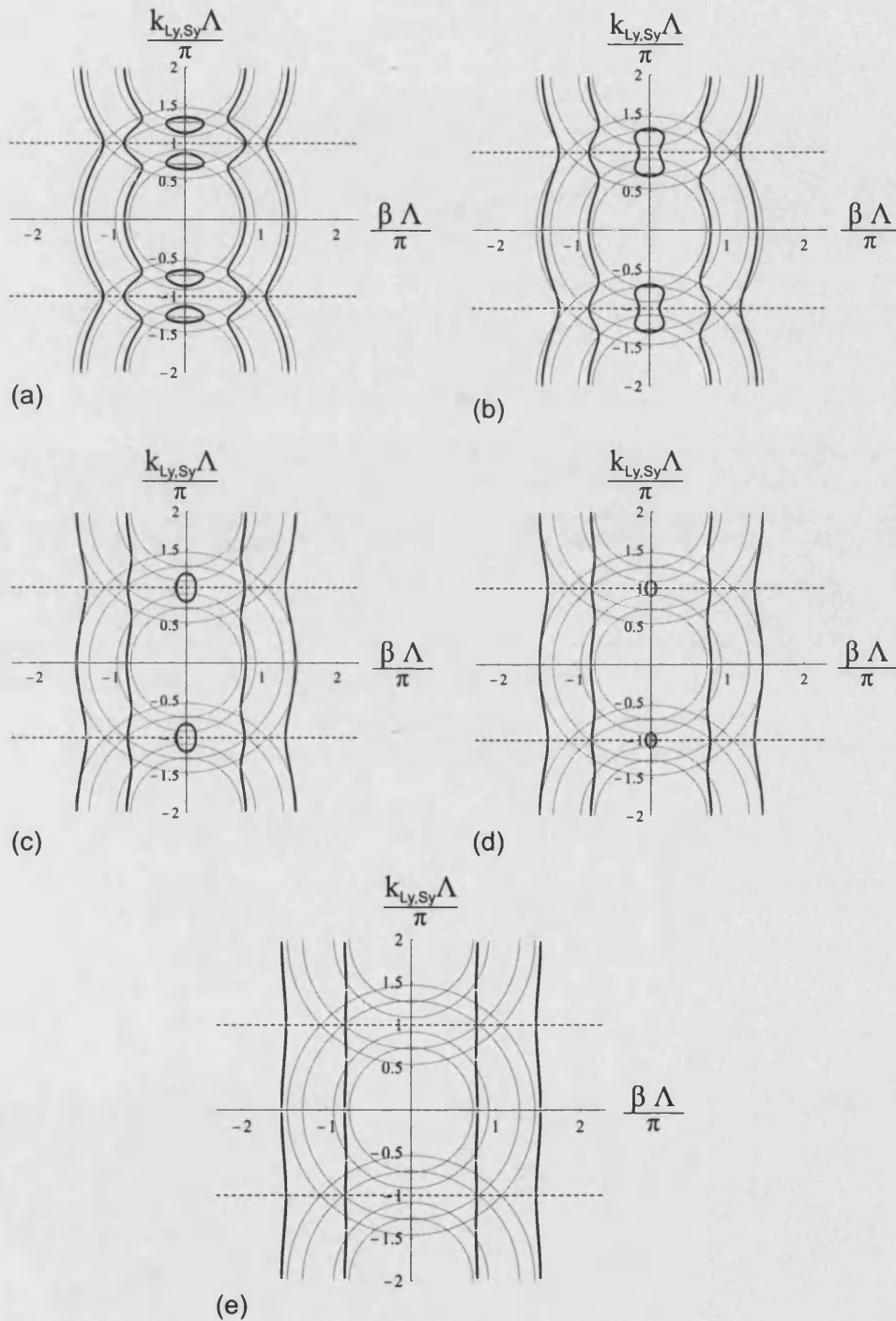Figure 4.4: Wavevector diagram for in-plane polarised waves propagating in a multi-layer stack, defined by $t_1 = 0.59$, with a normalised frequency of $\nu = 2.3$. The spatial dispersion (bold line) and stop-band development are shown for decreasing density ratio ρ_R; (a) $\rho_R = 0.8$, (b) $\rho_R = 0.6$, (c) $\rho_R = 0.4$, (d) $\rho_R = 0.35$, (e)$\rho_R = 0.2$. The first Brillouin zone is shown bounded by dashed lines.

Chapter 5

Brillouin Diagrams for Normal and Oblique Incidence

Chapter 5 presents the dispersion of elastic waves in various multilayer stacks and highlights the coupled longitudinal and shear stop-bands.

5.1 Anti-Plane Polarised Waves

Brillouin diagrams, or dispersion curves, are a plot of frequency against allowed real wavevectors. The slope $(\partial\omega/\partial k)$ of the plot at any point along the dispersion curve gives the group velocity of the wave for that particular frequency and wavevector.

The typical dispersion of anti-plane polarised elastic waves propagating in a direction normal to the interfaces $(\beta=0)$ in a multilayer stack, is shown in figure 5.1 [25]. The composition of the multilayer stack is the same as that studied in the previous chapter, however, it is re-stated here for clarification: $\rho_R = 0.898$, $t_1 = 0.59$, $n_{L1} = 1$, $n_{S1} = 1.75$, $n_{L2} = 1.25$ and $n_{S2} = 2.0$.

The dispersion diagrams were again constructed using equation 3.20, however this time, the β value was fixed and real valued solutions for the Bloch wavevector were calculated as the frequency ω, was varied.

As can be seen in figure 5.1, the group velocity of the anti-plane waves approaches zero at the band edges and the band centre, which is consistent with the implication that phonons cannot travel and therefore transport energy in the frequency range of
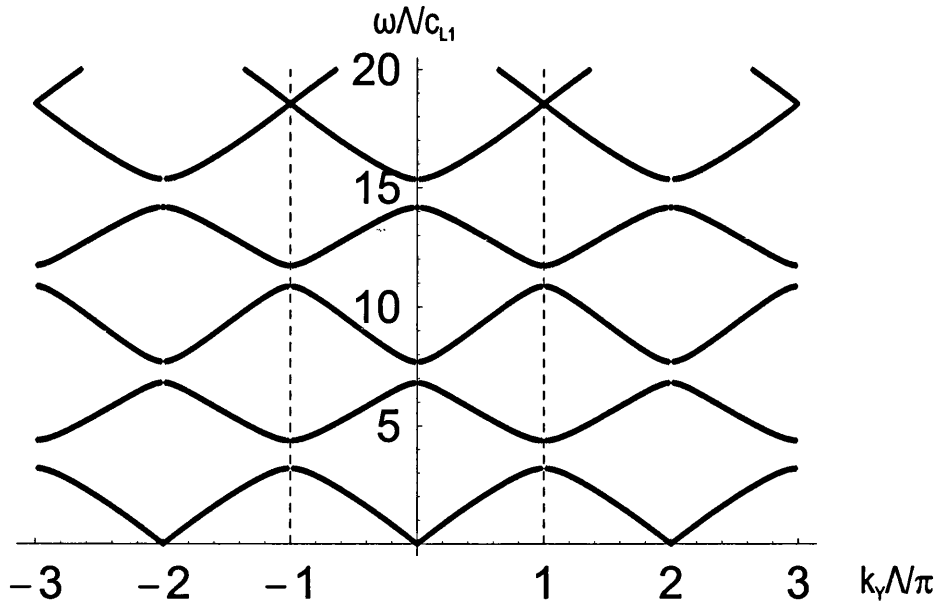
Figure 5.1: Typical dispersion curve of anti-plane polarised waves in a multilayer stack propagating at normal incidence ($b = 0$) to the interfaces. The first Brillouin zone is shown bounded by the dashed lines.

a phononic stop-band. At the band edge, the anti-plane polarised waves do not travel through the multilayer stack as the wavevector becomes imaginary. In this case the waves are totally reflected.

More generally, the dispersion of anti-plane polarised waves propagating in the multilayer stack at some angle to the interface (i.e. finite β value) is shown in figure 5.2 and it is seen that stop-bands open up at the band edge and band centre from zero frequency.

The dispersion curves shown in figures 5.1 and 5.2 are characteristic of the *folded* variety [50], whereby wavevector values greater than $|\frac{k_y \Lambda}{\pi}| = 1$ are shown in the first Brillouin zone. This illustration is possible due the periodic nature of the multilayer stack and is of course a consequence of Bloch's theorem as discussed in section 3.2.

The number of modes per unit frequency range supported by the system is found to have a reciprocal relation with the group velocity. Since the group velocity varies across the Brillouin zone, the *density of states*, or modes will vary also and at the Brillouin zone boundary where the group velocity becomes zero, the density of states become re-distributed into regions where the density of states is very large. These regions are separated by a frequency interval, namely the stop-band, in which the density of states is zero and thus relate to a range of frequencies for elastic waves (propagating at a given β value) which are not supported by the system.

49
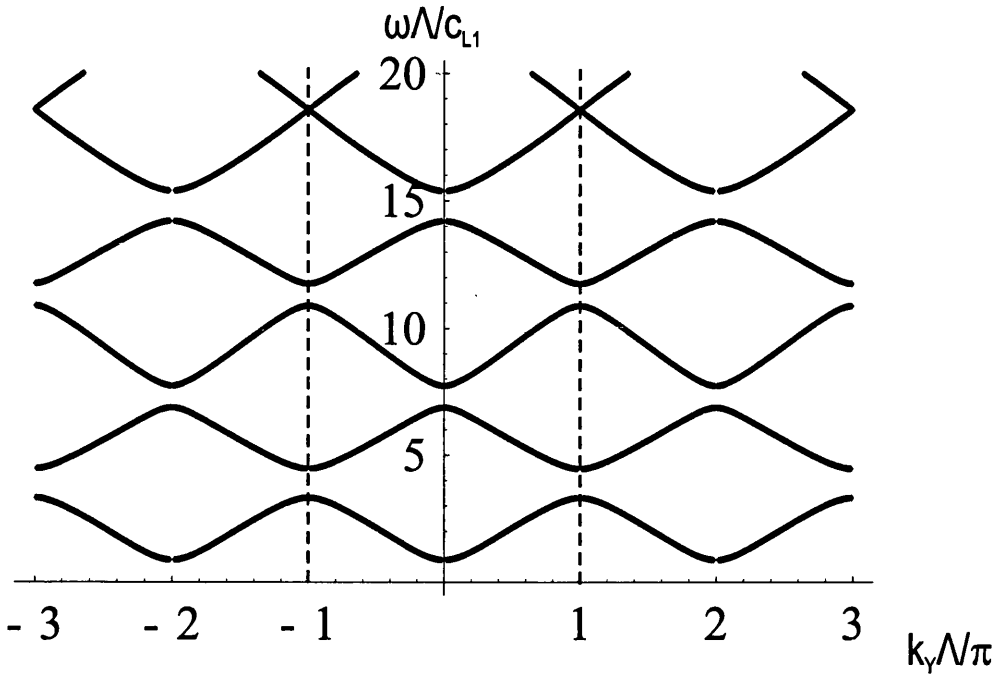
Figure 5.2: Dispersion curve of anti-plane polarised waves in a multilayer stack propagating at a finite β value, $b = 1.3$. The first Brillouin zone is shown bounded by the dashed lines.

Anti-plane polarised elastic waves present similar dispersion properties to TE and TM modes in a multilayer stack [18]. Significant differences are seen however with in-plane polarised elastic waves, which are coupled for finite β values and therefore complicate the dispersion, as shown in the next section.

5.2   In-Plane Polarised Waves

Figure 5.3a shows the dispersion of in-plane polarised elastic waves propagating at normal incidence to the interfaces of a multilayer stack [25] [26], the composition of which is that defined in the previous section. The dispersion diagrams were constructed using equation 3.32 by fixing β and solving for the Bloch wavevector as the frequency is varied, as discussed above. The linear red and blue lines of figure 5.3 correspond to the propagation of L and S waves respectively, in an effective medium that has elastic properties intermediate to that of layers 1 and 2 of the unit cell. The intersection of these construction lines determine the centre position of the stop-bands and it can be seen that where the L line intersects the S line coupled stop-bands develop. The coupled nature of the L and S waves however, is not evident on this plot as all elastic waves are uncoupled at normal incidence and since the system is isotropic, the SH and SV modes are degenerate at normal incidence. Moreover, the stop-bands at the

Brillouin zone boundaries of figure 5.3a are exclusive to the L and S waves, separately.

Figure 5.3b on the other hand, illustrates the coupling of L and SV waves which takes place at a finite β value (b=0.5). It can be seen that the group velocity goes to zero in places other than integer values of $k_y = \frac{\pi}{\Lambda}$. The high and low frequency sides of these coupled stop-bands do not occur at the same value of wavevector, despite Bragg's condition being satisfied. At these points, shown magnified in figure 5.4, the net transport of energy associated with the L (SV) wave of the coupled pair at the low frequency side of the stop-band is zero, however, the SV (L) wave at the high frequency side of the stop-band, has a finite group velocity and can therefore transport energy.
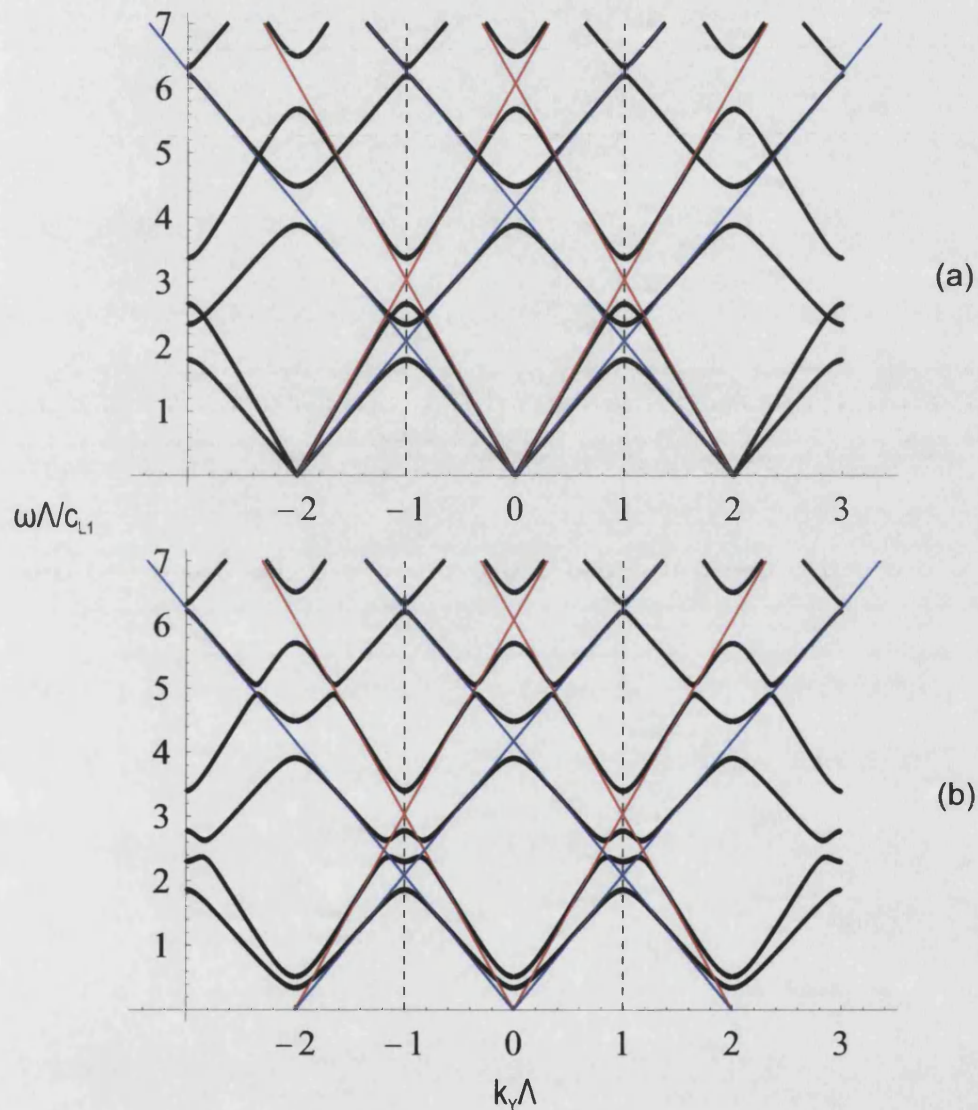
Figure 5.3: Typical dispersion curve of in-plane polarised waves in a multilayer stack propagating at (a) normal incidence ($b = 0$) to the interfaces and (b) at finite β value, $b = 0.5$. The first Brillouin zone is shown bounded by the dashed lines. The red and blue lines correspond to the dispersion of L and S waves respectively, propagating in an effective solid that has elastic properties intermediate to that of the properties of layers 1 and 2 of the period.
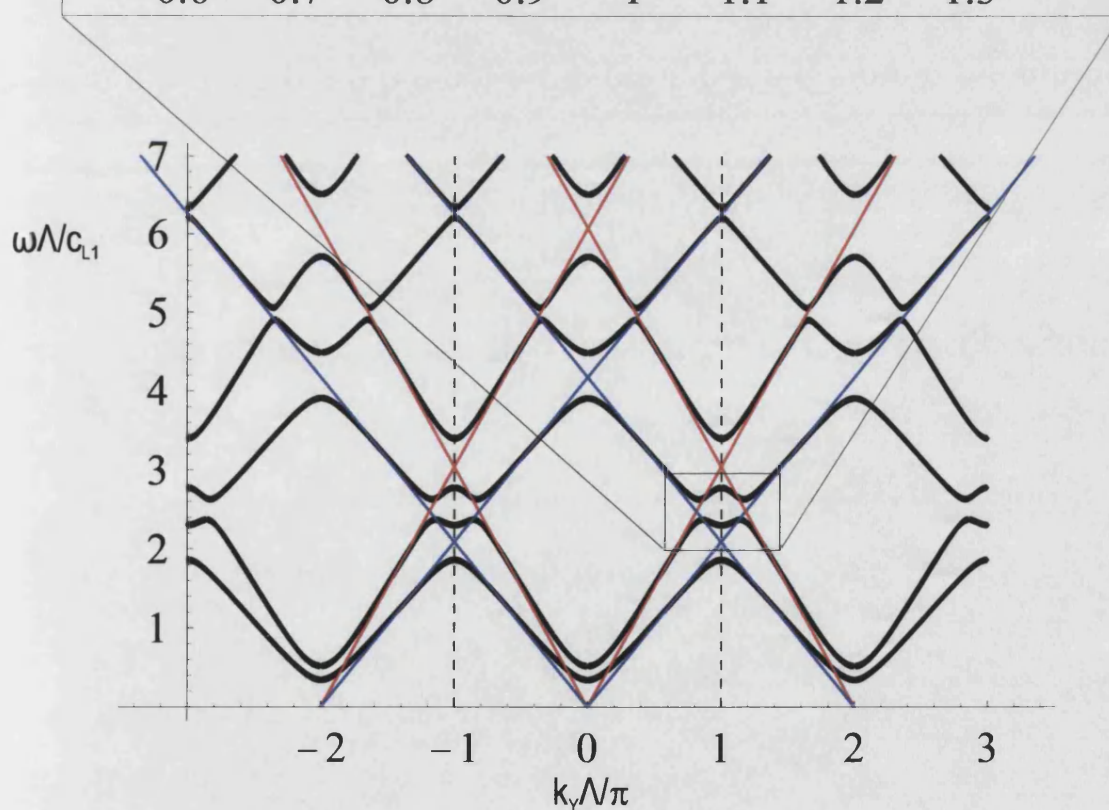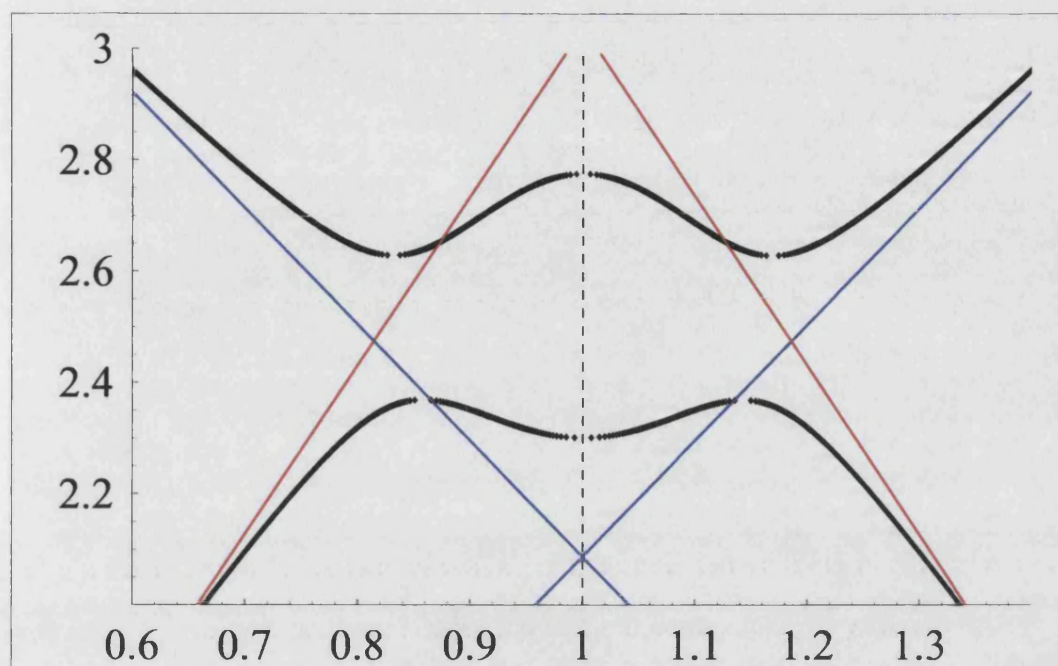
Figure 5.4: Magnification of the dispersion of in-plane polarised waves at a coupling point. The dispersion is shown for waves propagating at finite β value, $b = 0.5$, in the multilayer stack. The red and blue lines correspond to the L and S waves respectively, propagating in an effective solid that has elastic properties intermediate to that of the properties of layers 1 and 2 of the period.

Chapter 6

Band Edge Diagrams

Chapter 6 is concerned with the properties of stop-bands and the factors affecting them. The dispersion of coupled elastic waves is also presented for the interesting case of a plate in a vacuum.

Band edge diagrams map the position of the stop-band edges in frequency as the incident angle (i.e. the β value) is varied (see Russell *et. al* [18] for the band edge diagram for the optical modes of a periodic multilayer stack). This is useful since it allows one to map the propagation characteristics of the elastic waves in regions outside of the stop-bands. The diagram is a plot of frequency (ω) against β and the stop-bands are located at points where the moduli of the eigenvalues of the appropriate transfer matrix deviate simultaneously from unity, i.e. where the determinant of the transfer matrix is no longer 1.

The wavevector diagrams shown in chapter 4 illustrate the dispersion of elastic waves in a multilayer stack at a particular frequency (ω), as the incident angle (β) is varied. Conversely, the dispersion diagrams shown in chapter 5 present the dispersion of elastic waves in the multilayer stack at a fixed incident angle (β) as the frequency (ω) is varied. The band edge diagram however, combines these two dispersion presentations into a single diagram to describe the complete dispersion for elastic waves in the multilayer stack.
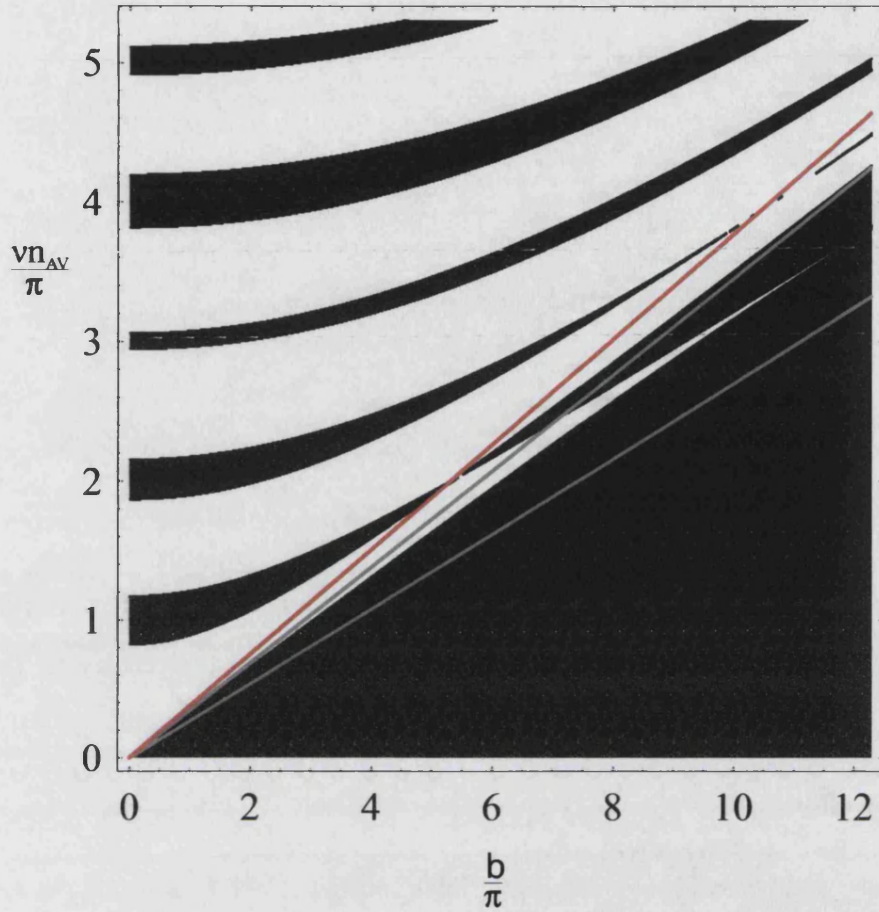
Figure 6.1: Band edge diagram for anti-plane polarised waves in a multilayer stack (type I) defined by ρ_R=0.898 and $t_1 = 0.59$. The linear grey lines are representative of the phase velocity of S waves in medium 1 and 2 and the linear red line corresponds to the first order anti-reflection condition. Here n_{AV} is the effective elastic index of the unit cell for anti-plane waves, defined as $n_{AV} = n_{S1}t_1 + n_{S2}(1 - t_1)$.

6.1   Anti-Plane Polarised Waves

The band edge diagram mapping the position of the stop-bands for anti-plane polarised waves in a multilayer stack having a unit cell incorporating a type I interface, is shown in figure 6.1. The composition of the stack is the same as that analysed in chapters 4 and 5 for comparison. The stop-bands are indicated by the shaded regions, in contrast to the unshaded regions in which the elastic waves can propagate. The slope of each linear grey line is proportional to the reciprocal of the relevant elastic index and is characteristic of the phase velocity of the elastic wave. For the stack in question, the steepest slope is representative of the phase velocity of anti-plane polarised waves in medium 1.

These so-called *soundlines* separate the band edge diagram into essentially three

regimes of propagation, the first being one in which free propagation is hampered by the appearance of stop-bands and is defined by $\beta < \frac{\omega}{c_{S1}}$. As the value of β increases beyond $\frac{\omega}{c_{S1}}$, the anti-plane waves will become evanescent in medium 1 and medium 2 will begin to support a micro-resonance. This regime is defined as $\frac{\omega}{c_{S1}} \leq \beta \leq \frac{\omega}{c_{S2}}$ and is termed the band window region. Values of $\beta > \frac{\omega}{c_{S2}}$ define the third regime, coined "cut-off" and relates to the region in which the elastic waves are evanescent in both layers of the unit cell.

6.1.1 Anti-Reflection Conditions

When the round trip phase difference across the unit cell becomes equal to an integral number of 2π the Bragg condition is satisfied and it is this condition which seeds the development of a stop band. This round trip must take into account the phase change upon reflection at an interface as well as the total path difference. In opposition to this, when the total round trip phase difference across each layer of the unit cell is separately and concurrently an odd multiple of π, each layer will be anti-reflecting. Thus, when the Bragg condition for the unit cell coincides with an anti-reflection condition from each layer, the width of the stop band will be reduced to zero [47].

For anti-plane polarised waves the phase change upon reflection is either 0 or π depending on whether the elastic wave is reflected from a medium which has a lower or greater density, respectively. However, since anti-plane waves reflected from the front and rear surface of any given layer within the multilayer stack always separately involve one soft and one hard reflection, the condition for anti-reflection and thus the positions of zero stop-band width are given by,

$$\frac{p_{S1}d_1}{m_1} = \frac{p_{S2}d_2}{m_2} = \pi \tag{6.1}$$

where $m_1 + m_2 = m$ with m_1 and m_2 being integers satisfying the anti-reflection condition in layers 1 and 2 respectively, and m is the mth order Bragg condition.

Solving equation 6.1 with normalised units yields,

$$b = \frac{\nu}{\pi} \sqrt{\frac{n_{S1}^2 - n_{S2}^2 q^2}{1 - q^2}} \tag{6.2}$$

and corresponds to an anti-reflection from each layer of the unit cell, with

$$q = \frac{(1 - t_1)m_1}{t_1 m_2}.$$ (6.3)

This reduction in stop-band width is shown in figure 6.1 with the linear red line. In places where the anti-reflection condition ($m_1 = m_2 = 1$) coincides with the stop-band position, the width of the stop band is seen to be reduced to zero. The similar situation occurs when the stop-band position coincides with the Brewster like condition, as discussed in section 2.3.3. Thus for anti-plane waves, the opening of a stop-band can be destroyed by two mechanisms.

6.1.2 Guided Modes of a Low Density Layer

The band window region, as bounded by the linear grey lines of figure 6.1, allows the guidance of S waves in only one of the layers of the unit cell of the multilayer stack. In such circumstances, if the system is allowed to reach a steady state of elastic deformation, the S waves which are evanescent in alternate layers of the stack will tunnel to adjacent layers [55] in which the waves are real and will thus be guided.

The dispersion of anti-plane waves in a layer bonded onto a substrate has been be obtained analytically by Love, whilst Lamb [56] has studied the characteristics of coupled L and S waves in a free plate (i.e. a plate in a vacuum). Brekhovskikh [57] derived the dispersion relation for elastic waves in laminar media through the consideration of the reflection coefficients at each interface within the laminate. This is a useful approach since neither the form of the field in adjacent layers nor the consideration of the boundary conditions are required. However, in formulating the dispersion of anti-plane waves here, it is thought more instructive to describe the form of the field in each layer of the laminate (in this case the multilayer stack) as this allows the modes to become separated according to their symmetry.

A good approximation to the dispersion of bound anti-plane waves in alternate layers of the multilayer stack, can be achieved through the consideration of bound anti-plane waves propagating in a low density layer of thickness d that is rigidly bonded between two semi-infinite media of higher density, as shown in figure 6.2. The form of the potentials describing the waves must cause the waves to decay outside of the layer and so for bound anti-plane waves the shear potential in the surrounding half-spaces (identified through subscript 2) can be written as,
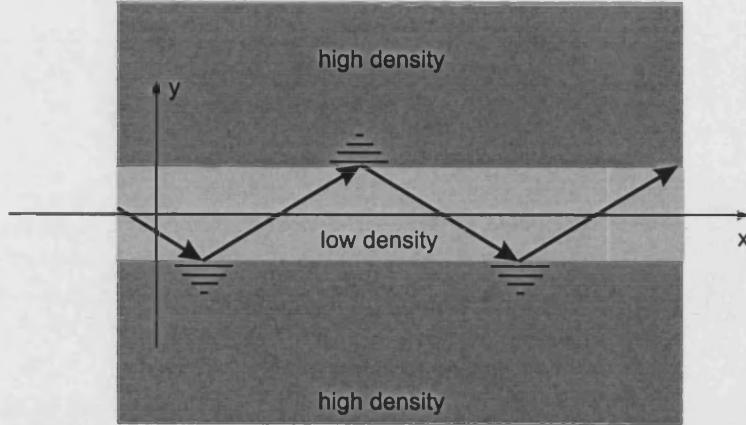
Figure 6.2: Schematic illustration showing the orientation of the low density layer rigidly bonded between two media of greater density.

$$\Psi_2 = [\underbrace{C \exp -(p'_{S2}y)}_{y \geq \frac{d}{2}} + \underbrace{D \exp (p'_{S2}y)}_{y \leq \frac{-d}{2}}] \exp -i(\beta x - \omega t) \tag{6.4}$$

which is seen to approach zero as $y \to \pm\infty$.

In writing the form of the evanescent waves as shown in equation 6.4, it should be noted that the wavevector component normal to the interface in the surrounding half-spaces has been made real in order to achieve the desired evanescence. The component normal to the interface has been re-defined as,

$$p'_S = ip_S = \sqrt{\beta^2 - \left(\frac{\omega}{c_S}\right)^2}. \tag{6.5}$$

The form of the potential describing the propagation within the layer (identified through subscript 1) can be written in terms of trigonometric functions so that the symmetric and antisymmetric modes can be readily identified. Thus, for the region defined by $|y| \leq \frac{d}{2}$, the shear potential becomes,

$$\Psi_1 = [A \cos(p_{S1}y) + B \sin(p_{S1}y)] \exp -i(\beta x - \omega t). \tag{6.6}$$

Now, in analysing the symmetric and antisymmetric modes of the layer, it is necessary to consider the symmetry of the displacement (i.e symmetry about the x-axis, see figure 6.3, which shows the surface displacement of a plate in a vacuum created by the passage
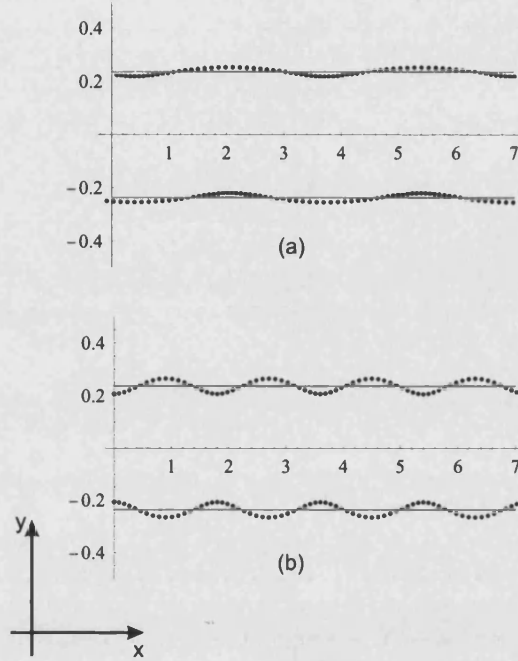
Figure 6.3: Plot showing the surface displacement of a plate in a vacuum during the passage of (a) an anti-symmetric and (b) a symmetric mode of coupled L and S waves. The undisturbed plate is shown bounded by the solid grey lines.

of coupled L and S waves) and not the symmetry of the potentials. The displacement of anti-plane waves is derived from equation 2.29 and in considering the displacement associated with such waves within the layer, equation 2.29 reveals,

$$U_z = \underbrace{(-i\beta A - p_{S1}B)\cos{(p_{S1}y)}}_{symmetric\ component} + \underbrace{(p_{S1}A - i\beta B)\sin{(p_{S1}y)}}_{antisymmetric\ component}. \tag{6.7}$$

Similarly, for anti-plane waves decaying into the surrounding half-spaces, the displacement is derived from equation 2.29 and can be shown to be of the form,

$$U_z = \underbrace{(-i\beta - p'_{S2})C\exp{(p'_{S2}y)}}_{y<-\frac{d}{2}} + \underbrace{(-i\beta + p'_{S2})D\exp{-(p'_{S2}y)}}_{y>\frac{d}{2}}. \tag{6.8}$$

The dispersion relation for bound anti-plane waves is governed by the boundary conditions at the interface between the layer and surrounding half-spaces. As previously stated (section 2.3.1), the boundary conditions for two solid media which are bonded require the conservation of the normal component of stress tensor and the conservation of displacement. The stress profile τ_{23} across the layer and in each half-space is given

59

below.

$$\tau_{23} = \underbrace{p_{S1}\mu_1(i\beta A + p_{S1}B)\sin(p_{S1}y) + p_{S1}\mu_1(p_{S1}A - i\beta B)\cos(p_{S1}y)}_{|y|\leq\frac{d}{2}} \qquad (6.9)$$

$$\tau_{23} = \underbrace{p'_{S2}\mu_2(-i\beta - p'_{S2})C\exp(p'_{S2}y)}_{y<\frac{-d}{2}} + \underbrace{p'_{S2}\mu_2(-p'_{S2} + i\beta)D\exp-(p'_{S2}y)}_{y>\frac{d}{2}}. \qquad (6.10)$$

The analysis is simplified if the symmetric and anti-symmetric modes are considered separately. This is achieved by imposing the conditions,

$$p_{S1}A = i\beta B$$

$$(-i\beta - p'_{S2})C = (-i\beta + p'_{S2})D \qquad (6.11)$$

which removes the anti-symmetric component from the analysis, and

$$i\beta A = -p_{S1}B$$

$$(i\beta + p'_{S2})C = (p'_{S2} - i\beta)D \qquad (6.12)$$

which removes the symmetric component.

Upon satisfying the boundary conditions at $y = \pm\frac{d}{2}$ and solving the relevant secular equation, the dispersion relation for the symmetric and anti-symmetric modes become, respectively,

$$\tan\left(\frac{p_{S1}d}{2}\right) = \frac{\mu_2 p'_{S2}}{\mu_1 p_{S1}} \qquad (6.13)$$

$$\tan\left(\frac{p_{S1}d}{2}\right) = -\frac{\mu_1 p_{S1}}{\mu_2 p'_{S2}}. \qquad (6.14)$$

The dispersion of these modes are shown in figure 6.4a for a layer/half-space density contrast identical to the density contrast of the layers of the multilayer stack analysed in

figure 6.1, i.e $\rho_R = 0.898$. The superposition of the band edge diagram of figure 6.1 with figure 6.4a is shown in figure 6.4b. The evolution of the first symmetric mode into the narrow white region is testament to the fact that as β increases the mode adopts more characteristics of wave propagation in a bulk medium which is that of the layer medium, and becomes more tightly bound within the layer. Although somewhat unclear from figure 6.4, it should be noted that the modal line representing the dispersion of the first symmetric mode, actually extends to $\omega = \beta = 0$ - there is not cut-off frequency for the first symmetric mode [38].

6.2 In-Plane Polarised Waves

The band edge diagram for coupled L and S waves in a multilayer stack having the same characteristics as the multilayer stack used to construct figure 6.1, is shown in figure 6.5. In contrast with figure 6.1, figure 6.5 can be divided into essentially five propagation regimes, again by the series of soundlines. As the β value increases at a given operating frequency, the waves become localised according to their phase velocity with the slowest wave becoming localised last; all waves will be evanescent for $\beta > \frac{\omega}{c_{S2}}$.

In considering the localisation and guidance of L and S waves in alternate layers of the multilayer stack it is useful to consider their simplified propagation in an infinite plate situated in a vacuum. Such a system provides a useful insight into their typical dispersion characteristics in the various propagation regions of figure 6.5, as discussed above.

The dispersion of coupled L and S waves in a plate has been previously calculated by Lamb [56]. For a plate orientated as shown in figure 6.6, the dispersion of the symmetric and antisymmetric modes can be obtained by satisfying the boundary conditions at the interface, which require the stress components to vanish at $y = \pm\frac{d}{2}$. In this manner the dispersion associated with the symmetric modes can be shown to be,

$$\frac{\tan\left(\frac{p_S d}{2}\right)}{\tan\left(\frac{p_L d}{2}\right)} = \frac{-4\beta^2 p_L p_S}{(\beta^2 - p_S^2)^2} \tag{6.15}$$

and the dispersion of the anti-symmetric modes can be shown to be,
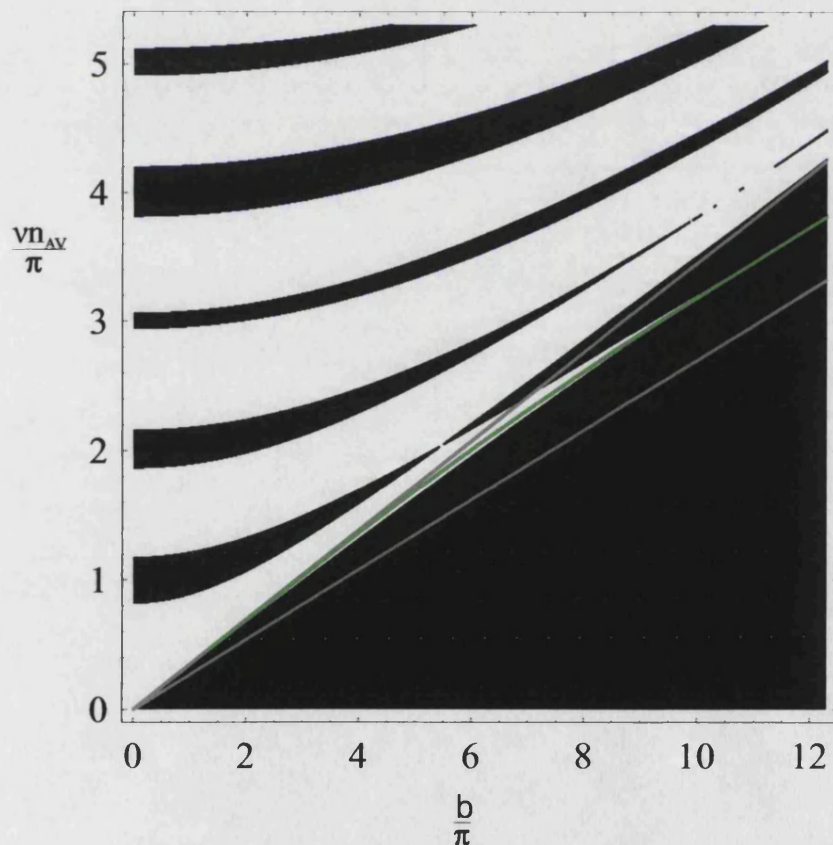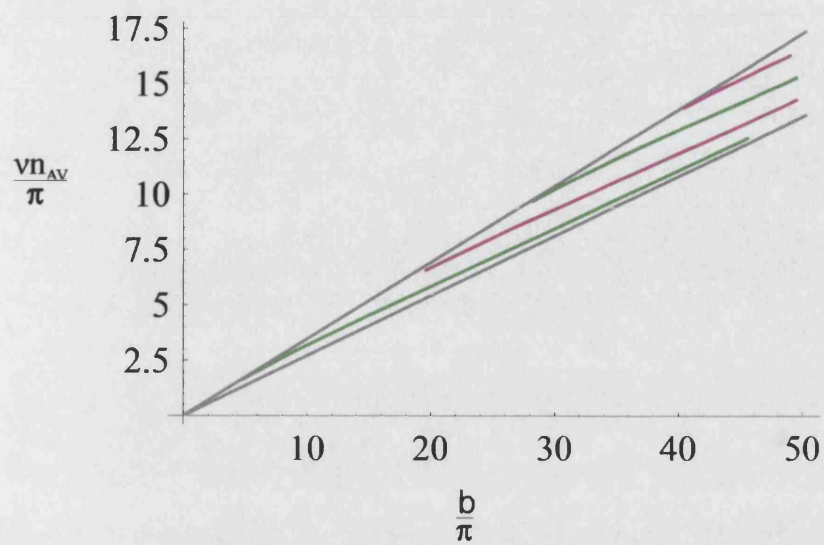
Figure 6.4: (a) Plot showing the dispersion of bound symmetric (green line) and bound anti-symmetric (pink line) anti-plane polarised waves propagating in the low density layer of figure 6.2. (b) Band edge diagram of figure 6.1 superposed with the dispersion of the first symmetric mode.
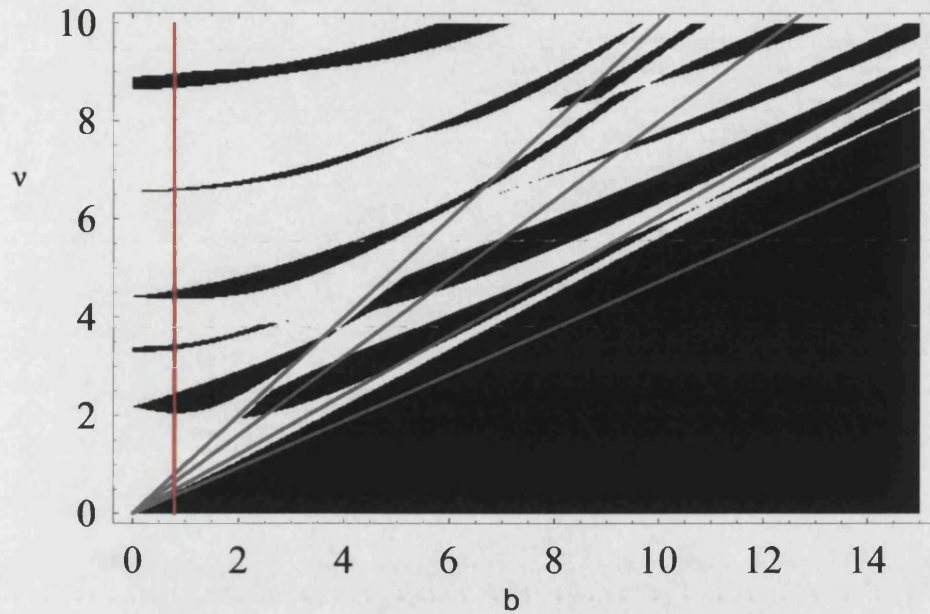
Figure 6.5: Band edge diagram for coupled waves. The soundlines are represented by the linear grey lines whilst the red line highlights the stop-bands which influence coupled L and S wave propagation at $h = 0.8$, as the frequency is varied.

$$\frac{\tan\left(\frac{p_S d}{2}\right)}{\tan\left(\frac{p_L d}{2}\right)} = \frac{(\beta^2 - p_S^2)^2}{-4\beta^2 p_L p_S}$$

$$\frac{\tan\left(\frac{p_S d}{2}\right)}{\tan\left(\frac{p_L d}{2}\right)} = \frac{(\beta^2 - p_S^2)^2}{-4\beta^2 p_L p_S}. \tag{6.16}$$

The dispersion of these modes are shown in figure 6.7. It is noted that the dispersion curves for modes of the same family do not cross each other, though a curve for a symmetric (anti-symmetric) mode may cross a curve for an anti-symmetric (symmetric) mode. For the second symmetric mode it is seen (highlighted in figure 6.8) that as β increases from zero, the value of ω initially decreases; the group velocity ($V_g = \frac{\partial \omega}{\partial k}$) is negative whilst the phase velocity is positive. Thus, the energy of the elastic waves is
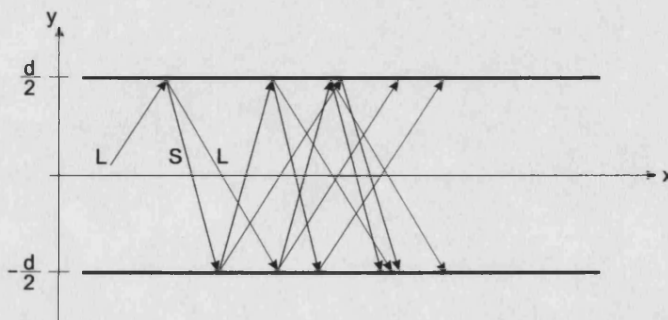
Figure 6.6: Cross-sectional view of the infinite plate in a vacuum. The coupling of the L and S waves at the interface is seen to become complicated after only a few reflections from the upper and lower surface.

63
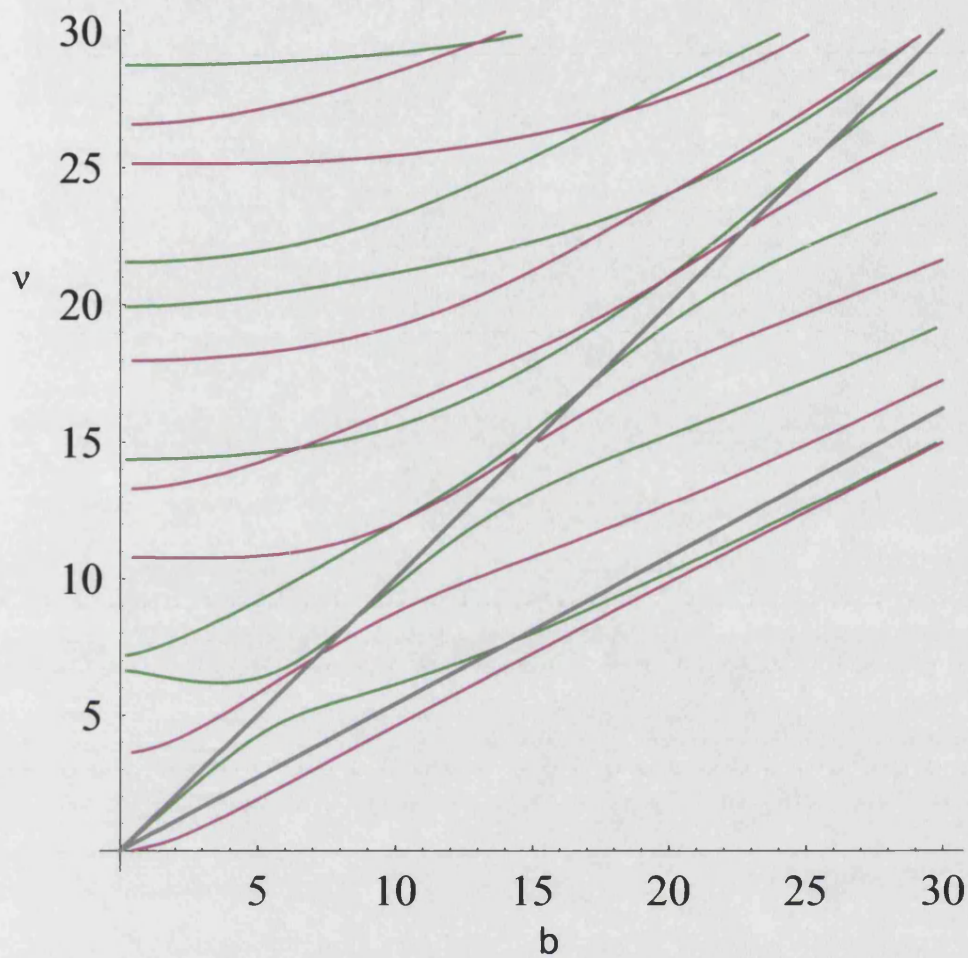
Figure 6.7: Dispersion of symmetric (green lines) and anti-symmetric (pink lines) coupled L and S modes of a plate in a vacuum. The grey lines are representative of the phase velocity of the L and S waves in a bulk medium of the plate material.

transported in a direction opposite to the direction in which the wave travels. This idea of "negative group velocity" has been previously studied by Mindlin [44], Meitzler [58] and Tolstoy *et al.* [59] to name but a notable few and experimentally confirmed by Holland [60], and is found to occur for both symmetric and anti-symmetric modes.

6.2.1   Anti-Reflection Conditions

The anti-reflection conditions discussed in section 6.1.1 are not representative of the complete set of anti-resonance conditions that can take place with coupled L and S waves. It has been determined during this study that in addition to the typical anti-reflection process whereby a forward propagating and backward propagating wave can interfere destructively to produce little or no reflected wave, coupled in-plane waves
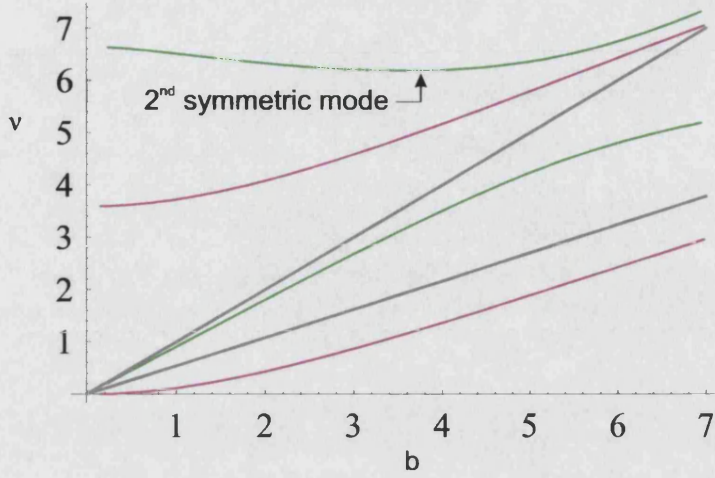
Figure 6.8: Magnification of the second symmetric mode which demonstrates the so-called negative group velocity. The grey sound lines correspond to the L and S phase velocity in a bulk medium of the plate material.

also facilitate further anti-reflection processes which involve multiple passes within a given layer and which can involve both polarisation states of the coupled waves.

Equations 6.17-6.20 represent the four types of anti-reflections that can take place with in-plane polarised, coupled waves (normalised units are considered here):

$$\frac{p_{L1(S1)}t_1}{m_1} = \frac{p_{L2(S2)}(1-t_1)}{m_2} = \pi \qquad (6.17)$$

$$\frac{p_{L1(S1)}t_1}{m_1} = \frac{p_{S2(L2)}(1-t_1)}{m_2} = \pi \qquad (6.18)$$

$$\frac{p_{L1(S1)}t_1}{m_1} = \frac{(p_{L2}+p_{S2})(1-t_1)}{2m_2} = \pi \; ; \; \frac{(p_{L1}+p_{S1})t_1}{2m_1} = \frac{p_{L2(S2)}(1-t_1)}{m_2} = \pi \qquad (6.19)$$

$$\frac{[(2\eta+1)p_{S1}+(2\xi+1)p_{L1}]t_1}{2m_1} = \frac{[(2\alpha+1)p_{S2}+(2\zeta+1)p_{L2}](1-t_1)}{2m_2} = \pi \qquad (6.20)$$

$$m_1 + m_2 = m \; ; \; (\eta,\xi,\alpha,\zeta)\epsilon Z^+$$

The first condition (equation 6.17) corresponds to the situation in which only L or S waves are anti-resonant in both layers separately, similar to anti-plane waves, whilst the second condition (equation 6.18) relates to anti-resonant L and S waves in alternate layers of the multilayer system.

The anti-reflection condition shown in equation 6.19 is an extension of those conditions expressed in equations 6.17 and 6.18. Equation 6.19 describes the situation in which one particular layer of the unit cell can support an anti-resonance involving a change of
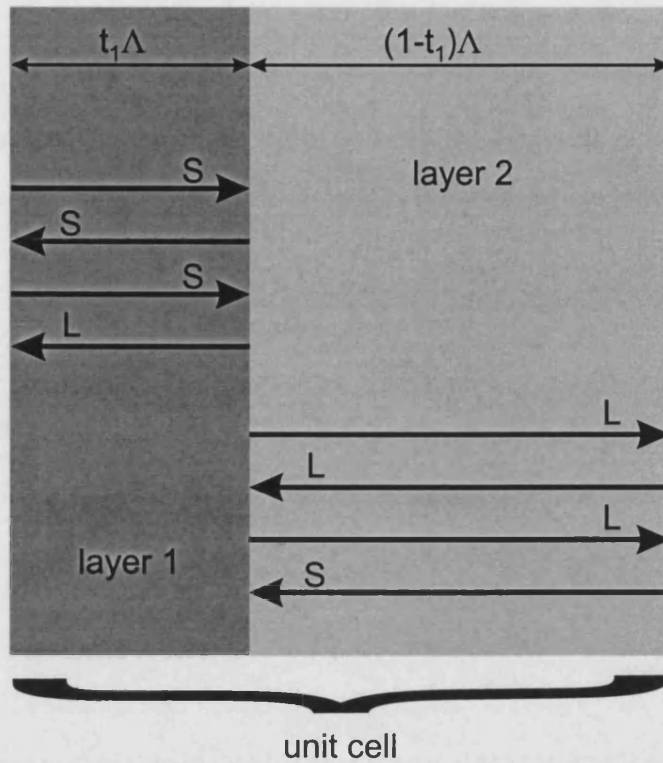
Figure 6.9: Illustration of the anti-resonant path with $\eta = \xi = 1$ and $\xi = \alpha = 0$ for the coupled waves in the layers of the unit cell

polarisation in completing a round trip of that layer, with the adjacent layer supporting an L or S wave anti-resonance only (as in equations 6.17 and 6.18).

The anti-resonant condition involving a change of polarisation in both layers of the unit cell is given in equation 6.20. In addition however, equation 6.20 also makes the provision for L and S waves that make multiple passes within each layer of the unit cell in satisfying the anti-resonant condition.

For example, taking $\eta = \zeta = 1$ and $\xi = \alpha = 0$ corresponds to the situation shown in figure 6.9, whereby the anti-reflection criterion in each layer is satisfied through performing two round trips of each layer, each involving a single change of polarisation.

These predictions are confirmed in figure 6.10, in which the frequency position of the stop band is mapped using t_1 as the independent parameter. The diagram is constructed for in-plane waves incident with a normalised β value of 0.8 (which corresponds to the red line in figure 6.5). The plot reveals a distinct beating pattern in the stop-bands as t_1 is varied, with the nodal positions being predicted by the anti-resonant conditions of equations 6.17-6.20.
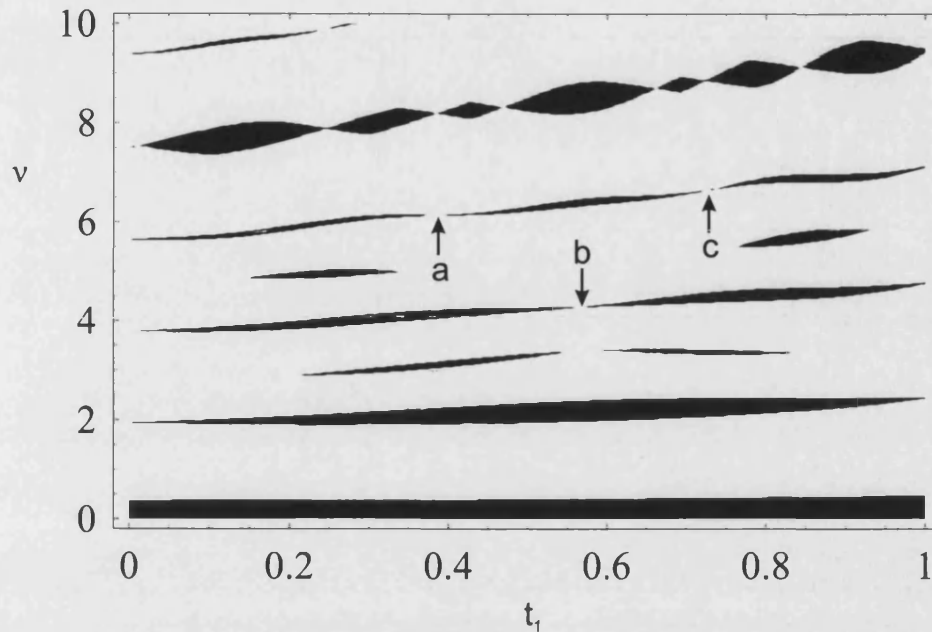
Figure 6.10: Band edge diagram for coupled L and S waves at a fixed β value ($b = 0.8$) in a stack defined as $\rho_R = 0.698$. The stop-bands are plotted as a function of the position of the interface in the unit cell.

The coupling between the L and S waves in figure 6.10 is weak since the waves are incident at near normal incidence ($\beta \approx 0$). Consequently, the wider stop-bands are largely due to pure S and L waves. In fact, the majority of the stop-bands shown in figure 6.10 are due to S waves; the S waves have the largest wavevector and so become resonant first. The nodes identified through labels a, b and c correspond to a conversion resonance ($\eta = \xi = \zeta = \alpha = 0$ from equation 6.20) and since $\beta \approx 0$ the stop-band width is noticeably thinner than for the pure S anti-resonances.

6.3 Elastic Wave Propagation - Summary

L and S wave stop-bands have been shown in chapters 4 and 5 to develop once a threshold frequency has been reached. Thereafter, the width of the stop-band will be determined largely by the density contrast between the layers and the relative layer thickness. In this chapter, anti-reflection conditions have been derived for coupled waves and these have been shown to cause the width of the stop-band to reduce. It is believed that the derivation of these conditions for coupled waves, wherein the waves can undergo multiple passes within each layer to generate an anti-resonance, is a new result.

Chapters 1-3 of Part I were provided to serve a general understanding of elastic wave

propagation in singly periodic systems while chapters 4-6 illustrated their complex propagation. The experimental analysis of elastic wave propagation in doubly periodic systems is undertaken in Part II, whereby their propagation characteristics are inferred from light scattering measurements. More particularly, it is the intention of Part II of this thesis to develop the understanding of the influence of elastic wave guidance in photonic crystal fibre, on the optical modes propagating therein.

Part II

Brillouin Scattering in Photonic Crystal Fibre

Chapter 7

Introduction and Literature Review

Chapter 7 provides a general introduction to the interaction of elastic waves with light in 2D structures, in particular the photonic crystal fibre.

Brillouin scattering is the scattering of light by phonons. In optical media, light is scattered by fluctuations in the dielectric constant. These can arise from static inclusions or impurities that scatter the light elastically with no frequency change (Rayleigh scattering), or dynamic fluctuations such as molecular vibrations and density variations. The thermally activated density variations [61] in fibres act as centres for the generation of light at different frequencies and can corrupt signals which rely on narrow bandwidth laser light [62]. In bulk media the magnitude of the scattered signal is found to be a function of the scattering angle, being zero in the forward direction and a maximum in the backward direction [63]. Optical fibres however, present a 2D confinement to the guided modes and so the scattered light or Stokes signal is restricted (at least in single mode optical fibres [64],[65]) to the backward propagating direction only.

Brillouin scattering is a non-linear effect and occurs at the lowest threshold power of all the non-linearities. Stimulated Brillouin scattering, or SBS, was first observed in conventional optical fibre by Ippen and Stolen [66] in 1972 and since then has received much attention. Yeniay *et al.* [67] have experimentally studied the behaviour of Brillouin scattering in single mode fibres with different waveguide characteristics, in terms of the elastic modes. Yeniay used GeO_2 doped core fibres which facilitated total internal reflection of the elastic modes, whilst Shibata *et al.* [68] have studied the gain spectra for single mode fibres which had pure silica, GeO_2 and P_2O_5 doped cores, and thus different index profiles. The spectral shape of the gain spectra was found to

be dependent on the waveguide structure, in particular the index profile, whilst the bandwidth was found to be dependent on the doping materials of the core.

Brillouin scattering can become stimulated in optical fibres at optical powers apparently lower than the predictions of conventional theory due to external feedback. This has been reported by Dämmig [69] and Gaeta [70], and can lead to fibre based Brillouin lasers [72]. The external feedback can be provided in the form of a mirror system which encloses the optical fibre, or simply by the perpendicularly cleaved end facets of the fibre. In such cases the pump and Brillouin shifted light undergo multiple passes through the optical fibre which enhances the acoustooptic interaction and thus lowers the threshold power, and results in a Brillouin signal emanating from both ends of the fibre.

Since Brillouin scattering is inherently concerned with the interaction of light with elastic waves, it is no surprise that Brillouin scattering can also reveal information about the elastic modes of the structure. However, conventional single mode fibre does not provide the necessary waveguide characteristics to guide elastic waves and so it is inappropriate to speak of modes. In order to guide elastic waves in conventional fibre, the index contrast must be reversed as compared with the optical case. Shibata *et al.* [73] have studied the Brillouin gain spectra in specially prepared fibre that is capable of guiding elastic waves. The gain measurements were performed at 1286nm and 1550nm in GeO_2 doped core fibre with a pure silica cladding; several L modes were identified through analysing the phase velocity of the elastic waves. However, the optical modes involved in the scattering event were not guided in the core of the fibre by total internal reflection, but by reflection at the boundary between the fibre cladding and surrounding environment.

In this part of the thesis, the optical fibre in question is manufactured from pure silica with an index contrast between core and cladding that is suited for the guidance of optical modes by total internal reflection. However, the *photonic crystal fibre* also permits a further guidance mechanism which allows for the *simultaneous* guidance of elastic waves in the *same* core region. In such a waveguide, the acoustooptic overlap is expected to be significant and as such, it is expected that this will lead to departures from the conventional understanding of SBS theory which will hopefully reveal new information as to the guidance of the elastic waves.

Chapter 8

An Overview of Photonic Crystal Fibre

Chapter 8 provides an account, albeit succinct, of the photonic crystal fibre and alludes to alternative guidance mechanisms and properties thereof.

Today, optical fibres play a role in almost everyone's life. At first sight these structures seem nothing more than hair-thin strands of glass, yet are capable of conveying data signals on a global scale at speeds comparable to the speed of light.

The science behind the success of conventional fibres has remained unchanged since the early 1980's and is based on the concept of total internal reflection. Conventional fibres are formed from two types of glass, which between them constitute the central core region and the cladding region which surrounds the core as shown in figure 8.1. The core and cladding have different refractive indicies with the core having a higher index than the cladding. This mismatch in index is achieved by doping the core with typically germanium oxide and permits the incidence of rays of light at shallow enough angles upon the core-cladding interface to be totally reflected and therefore confined within the core region [74].

In contrast to conventional optical fibres, photonic crystal fibres (PCF) use just one material, typically fused silica, and comprises an array of microscopic air holes running along its length. The structure is such that when the cleaved end is viewed under a microscope the arrangement of air holes is reminiscent of a crystal lattice. The light is guided in the core of the fibre, which either comprises a missing capillary (hollow core) [75], [76] or a silica rod (solid core) [77], [78], by the honeycomb cladding, which strongly scatters the light, blocking its escape from the core.
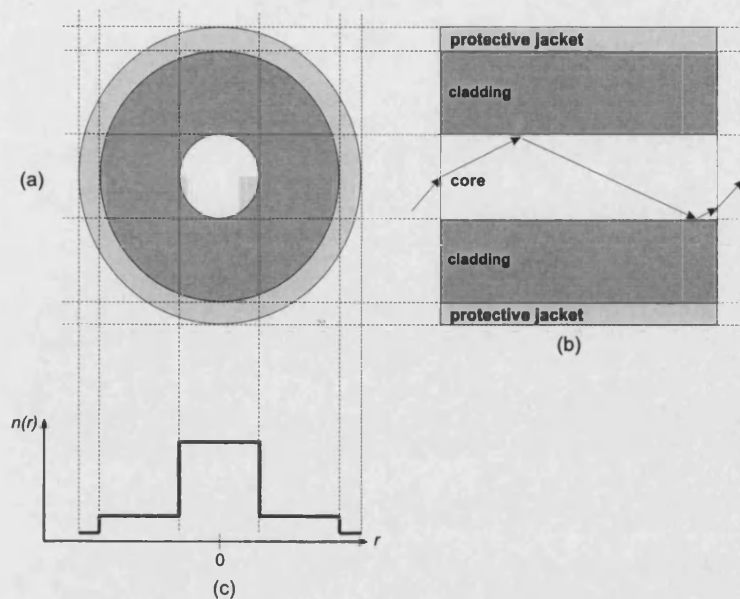
Figure 8.1: A cross-sectional view through the (a) short and (b) long axis of conventional optical fibre. The the refractive index profile along the short axis is shown in (c).

The air holes running along the length of the fibre alter the propagation properties of light in remarkable ways, owing as much to the average index of the cladding as to the arrangement of air holes. Figure 8.2 shows the far field pattern of red light exiting a solid core PCF. The central core is clearly visible along with the surrounding array of air holes. The fibre, which is shown at the top of the figure, is lossy at this wavelength and thus the red light is seen to spread out from the core into the surrounding cladding.

The properties of PCF are governed primarily by the size and shape of the pattern of air holes and so is limited at first instance to the researcher's imagination. However, the original idea for this type of fibre dates back to 1991 and it was not until 1995 that the fabrication problems were resolved and the first "working" PCF was realised.

8.1 The Influence of Photonic Crystal Fibre on Light

Unlike conventional fibres, PCF supports two mechanisms by which light can be trapped within the core and therefore guided along it. The first mechanism relates to a hybrid of conventional total internal reflection, while the second refers to the new effect of a *photonic band gap* (PBG).

For hollow core PCF, i.e. an air core, the refractive index contrast does not permit guidance by total internal reflection. However, the structure of the cladding creates
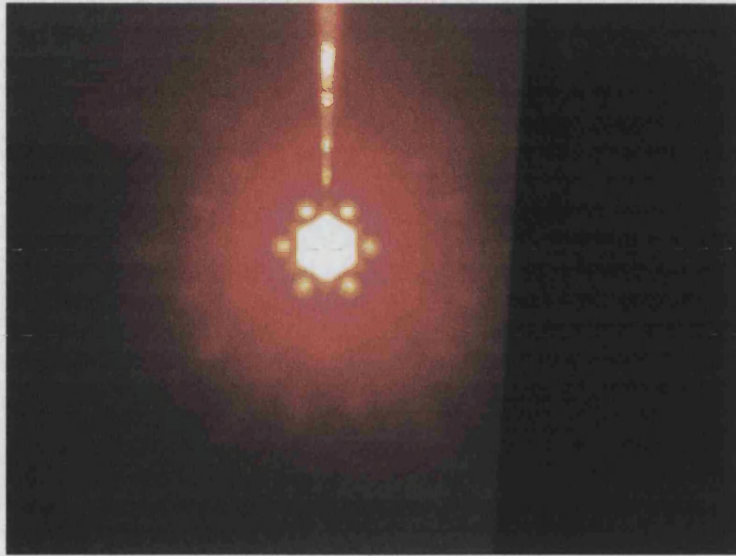
Figure 8.2: Far field pattern of red light exiting a solid core PCF which is shown at the top of the figure.

coherent backscattering of light into the core for certain wavelengths of light incident at certain angles upon the core-cladding interface. This is evident if white light is passed into a hollow core PCF - the exit facet is usually coloured indicating the guidance of several wavelengths.

Solid core PCF on the other hand does have a cladding region which has an area-averaged refractive index which is lower than the core and so in addition to band gap guidance, it also permits light to be guided in the core by a modified form of total internal reflection - the air holes surrounding the solid core act as barriers to the various modes which can exist in the core.

The most significant parameters in designing PCF are the hole diameter and hole spacing. As the ratio of hole diameter to hole spacing increases, successive higher order modes become trapped because the silica bridges holding the core within the cladding get thinner and thinner. This has the effect of restricting the leakage of the modes from the core. For small enough holes, the fibre becomes single mode and remains single mode at all wavelengths where the glass remains transparent - a property termed *endlessly single-mode* [79].

Interestingly, the unique structure of PCF is predicted to have a novel effect on elastic wave propagation. The effects are expected to lead to new ways of enhancing/supressing phonons by altering the density of states within the core region. It is thought that altering the density of states could affect the power limitation imposed by stimulated Brillouin scattering and the associated frequency shift (see chapter 9). Accordingly, it

is these concepts which are considered here.

Chapter 9

Brillouin Scattering in Conventional Optical Fibre

Chapter 9 summarises the essential concepts and parameters of Brillouin scattering in conventional optical fibres.

In optical fibres, Brillouin scattering manifests through the generation of a backward propagating Stokes wave that carries most of the input energy. The scattering effects are generally undesirable in, for example, systems incorporating parametric amplification, however, SBS can also be used advantageously, for example, as strain sensors or temperature sensors in hostile environments where electrical instruments would fail [80],[81].

Brillouin scattering can become stimulated in optical fibres due to the high optical intensity in the core and long interaction lengths afforded by these waveguides. The stimulated process is seeded from the random distribution of phonon energies available to the pump signal in the fibre at room temperature. The pump wave selects from this phonon distribution those phonons that phase match it to the Stokes wave (alternatively, the seeding process can be considered to be due to a virtual Stokes photon which propagates in the opposite direction to the pump, within the core of the fibre). The interference of the counter-propagating pump and Stokes waves excites an elastic wave through the process of electrostriction and leads to a coupling between the pump and Stokes waves. The incident pump wave thus stimulates a periodic modulation of the core density and therefore the refractive index that moves at the phase velocity of the elastic wave. This travelling index grating scatters the pump light to the downshifted (Brillouin shifted) Stokes wave because of the Doppler effect.
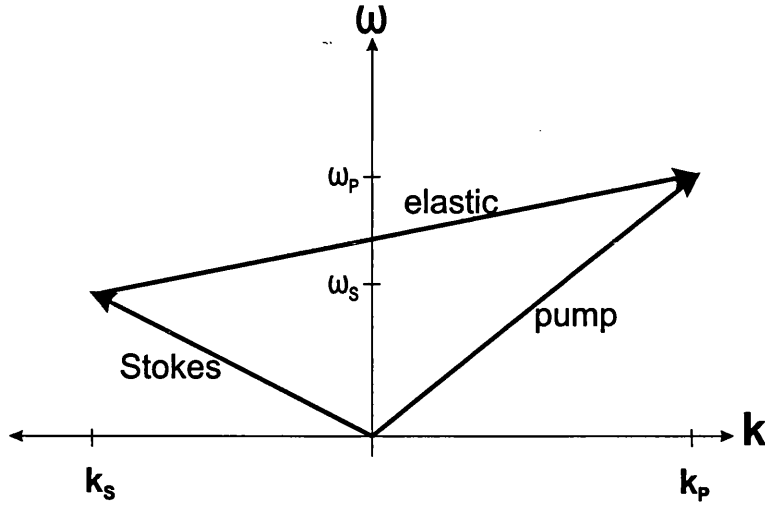
Figure 9.1: An illustration of the conservation of energy (ω) and momentum (k) during Brillouin scattering.

Since both energy and momentum must be conserved during the scattering events, the angular frequency (ω) and wavevectors (k) of the participating waves can be written using the four-vector equation as,

$$[\mathbf{k_P}, \omega_P] - [\mathbf{k_S}, \omega_S] = [\mathbf{k_E}, \omega_E] \tag{9.1}$$

where the subscripts refer to the pump (P), Stokes (S) and elastic (E) waves respectively. The scattering event is shown exaggerated in figure 9.1.

In single mode optical fibres, the phase matching condition is satisfied only for the backward direction. However, for elastic waves that are guided in the core, spontaneous scattered light is also evident in the forward direction due to thermally excited elastic waves propagating transversally to the fibre axis. This is known as Guided Acoustic Wave Brillouin Scattering (GAWBS) [82]. In conventional optical fibres however, the density contrast between core and cladding does not permit total internal reflection for elastic waves and so GAWBS is typically a weak effect.

SBS can severely limit the optical power that can be transmitted through an optical fibre and so inevitably, it has been the subject of extensive research in optical systems. The characteristic frequency shift, threshold power and Brillouin gain spectra associated with Brillouin scattering are found to be strongly dependent on fibre geometry and core composition and accordingly, are outlined in detail in the following sections.

9.1 The Governing Equations for Conventional Optical Fibres

9.1.1 SBS Threshold Power and Gain

The mutual interaction between the pump and Stokes waves is governed by a set of coupled equations. Since the frequency difference between the pump and Stokes waves is approximately five orders of magnitude smaller than the pump and Stokes frequencies, it is assumed that $\omega_P \approx \omega_S$. For the same reason it is assumed that the fibre loss (α) is the same for the pump and Stokes waves. Therefore, under steady state conditions, the coupled intensity equations for the pump and Stokes waves can be written as,

$$\frac{dI_P}{dz} = -g_B I_S I_P - \alpha I_P \tag{9.2}$$

$$\frac{dI_S}{dz} = -g_B I_P I_S + \alpha I_S \tag{9.3}$$

where g_B is the peak value of the Brillouin gain coefficient and occurs at the frequency value, $f = f_B$ (where f_B is the Brillouin frequency shift).

Ignoring the effects of pump depletion, the Stokes intensity is found to grow exponentially in the backward direction according to the relation,

$$I_S(0) = I_S(L)\exp(g_B P_0 L_{eff}/A_{eff} - \alpha L) \tag{9.4}$$

where $P_0 = I_P(0)A_{eff}$ and A_{eff} is the effective core area. L_{eff} is the effective interaction length given by,

$$L_{eff} = \frac{1}{\alpha}(1 - \exp(-\alpha L)) \tag{9.5}$$

and defines the fibre length over which the Stokes field grows appreciably, and is less than the actual fibre length due to the attenuation. (Here the attenuation is measured in units of m^{-1}).

The Brillouin threshold is found to occur at a critical pump power P_{th} approximated by the relationship,

$$P_{th} \approx \frac{21 A_{eff}}{g_B L_{eff}}. \tag{9.6}$$

The numeric factor (21 in this case) is dependent on the relative polarisation between the pump and Stokes waves and the Brillouin gain linewidth. For the condition whereby the pump and Stokes waves are completely scrambled along the fibre, this factor can increase by a factor of 2, however, this factor will typically vary between 1 and 2 [83],[84].

The spectral linewidth of the Brillouin gain is dependent on the damping time of elastic waves, or phonon lifetime (T_B, which for conventional fibres is in the nanosecond range). If the elastic waves are assumed to decay as $\exp -t/T_B$, the Brillouin gain has a Lorentzian spectral profile given by,

$$g_B(f) = \frac{(\Delta f_B/2)^2}{(f - f_B)^2 + (\Delta f_B/2)^2} g_B(f_B) \tag{9.7}$$

where Δf_B is the full width at half maximum of the Brillouin line, and is related to the phonon lifetime by $\Delta f_B = (\pi T_B)^{-1}$. The peak value of the Brillouin-gain coefficient occurring at $f = f_B$ is given by,

$$g_B(f_B) = \frac{2\pi n^7 p_{12}^2}{c \lambda_P^2 \rho v_E \Delta f_B} \tag{9.8}$$

where p_{12} is the longitudinal elasto-optic coefficient, ρ is the material density, v_E is the elastic wave phase velocity and λ_P is the pump wavelength [63].

For continuous wave (or quasi continuous) pump sources, the Brillouin gain can be reduced if the pump spectral width exceeds the Brillouin spectral width. For a pump having a Lorentzian spectral profile of width (FWHM) Δf_P, the Brillouin gain spectrum as given by 9.7 becomes,

$$\tilde{g}_B = \frac{\Delta f_B}{\Delta f_B + \Delta f_P} g_B(f_B). \tag{9.9}$$

9.1.2 Brillouin Frequency Shift

The frequency shift associated with the pump wave can be derived from the simple consideration of the interference of a forward propagating wave at a frequency f_1 and a backward propagating wave at a frequency f_2. The phase velocity of the resulting interference pattern can be shown to be,

$$\frac{\omega_1 - \omega_2}{k_1 + k_2} \tag{9.10}$$

which must be phase matched to the phonon. Alternatively, equation 9.10 can be written as,

$$\frac{\omega_1 - \omega_2}{k_1 + k_2} = v_E = \frac{f_1 - f_2}{n_1/\lambda + n_2/\lambda} \tag{9.11}$$

and since $n_1 \approx n_2$,

$$f_1 - f_2 = f_B \approx \frac{2n v_E}{\lambda} \tag{9.12}$$

Alternatively, the approximation to f_B can proceed from the conservation of momentum and energy (equation 9.1) as shown by Agrawal [63]. As seen above, the Brillouin shift is directly proportional to the phase velocity of the elastic wave and so any waveguide which facilitates the simultaneous guidance of both elastic and EM waves could be expected to produce several Brillouin shifted lines due to the discrete nature of the elastic modes.

9.2 Elastic Waves in Photonic Crystal Fibre

The effects of elastic wave guidance on the Brillouin spectrum become significant when the wavelength of the elastic wave becomes comparable to the core diameter of the PCF. For large core diameters, it is expected the elastic wave will demonstrate bulk-like propagation characteristics, producing a Brillouin shifted frequency which is indicative of the phase velocity of elastic waves in a bulk media and moreover, predictable by conventional theory.

For core sizes which are comparable to the elastic wavelength of the elastic wave, it is expected that the continuum of elastic states available in bulk solids will separate into discrete modes of a defined frequency. It is anticipated that this small core regime will produce the most dramatic changes to the Brillouin spectrum.

As stated previously, the guidance mechanism associated with conventional fibres is the well-known total internal reflection, and since the condition for total internal reflection is only suited to elastic waves or EM waves separately, the effects of elastic wave guidance on EM waves in conventional fibres is very weak. For solid core PCF, the elastic waves can be guided by a phononic band gap whilst the EM waves can be guided by a modified form of total internal reflection (and/or a photonic band gap). It is this double handed guidance of PCF which makes them such an attractive waveguide in understanding the effects elastic wave guidance on SBS and thus from which we can harvest information about the elastic modes. Ultimately however, SBS should allow us to experimentally demonstrate the guidance of elastic waves by a phononic band gap [85].

The effects of a phononic band gap on the Brillouin spectrum is expected to be one in which several Brillouin shifted lines are produced. The strength, i.e. the intensity of a particular Stokes line will be dependent on the overlap between the EM mode and the elastic mode participating in the scattering event.

Arguments pertaining to the effects of elastic wave guidance on threshold power are less conclusive. On the one hand, it is speculated that their guidance will produce a very low threshold power for SBS since the elastic waves can propagate with low loss. However, it is also arguable that a structure which permits guidance also shields, and so it may be the case that the cladding of the PCF reduces the density of states within the core by shielding the core from the noisy environment, thus creating a very high threshold power.

Whatever the findings, PCF and SBS are well partnered to study the effects of elastic wave guidance by a phononic band gap.

Chapter 10

Measuring the Brillouin Frequency Shift

Chapter 10 is concerned with the experimental determination of the threshold power and frequency shift associated with Brillouin scattering, in photonic crystal fibre, using a heterodyne technique and also the technique which utilises the Fabry-Perot interferometer.

10.1   The Heterodyne Method

If the Stokes wave generated through the Brillouin scattering process can be hetero-dyned (i.e. mixed) with the pump wave then electrical spectral analysis can be performed on the signal rather than optical analysis. Heterodyning has the advantage of a higher spectral resolution for the measurement of the Brillouin shift and spectral linewidths. The experimental arrangement for the heterodyne analysis of the Stokes signal is shown in figure 10.1.

The signal from a Photonetics ECL was amplified by an Er-doped fibre amplifier. Approximately 1% of the pre-amplified signal was used as a local oscillator for the self-heterodyne detection. The amplified signal was passed to the test fibre via a circulator which chanelled the backscattered Brillouin signal into the detection system. The PCF used in this experiment had a larger NA than conventional SMF and so a high NA fibre was used to couple the signal into the PCF. The high NA fibre and PCF were mounted on a high precision Melles-Griot translation stage and the signal was butt-coupled into the PCF under the view of an optical microscope. The initial butt couple alignment
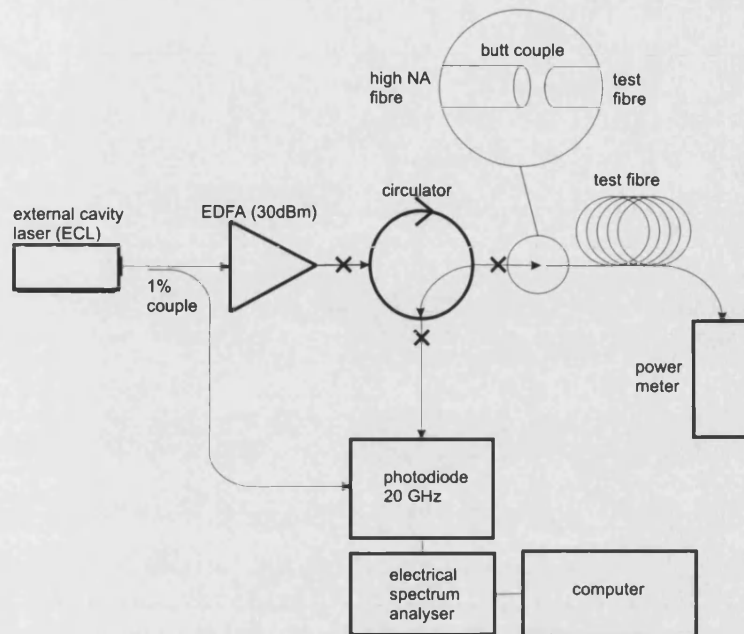
Figure 10.1: Experimental system for measuring the Brillouin shift in optical fibre using a heterodyning method

was performed using an optical power of 3dBm and the coupling loss was estimated by measuring the output power with an optical power meter. Careful alignment resulted in a coupling loss of 0.5dB. The spectrum of the backscattered light was recorded using an electrical spectrum analyser and the integrated power was measured with an optical power meter.

The experiment was performed at three wavelengths, 1530nm, 1550nm and 1570nm. At each wavelength the Brillouin spectrum was recorded with the launch power increasing from below the threshold power, to above the threshold value, and in order to maintain consistency, the measurements at each wavelength were made with the same initial coupling alignment.

10.1.1 Results

An SEM of the PCF studied is shown in figure 10.2. The all-silica fibre had a core diameter of 5.2μm, a pitch of 3.4μm and a loss of 3dB/km @ 1550nm. The effective length (equation 9.5) of the fibre was calculated to be 408m with a fibre length of 480m.
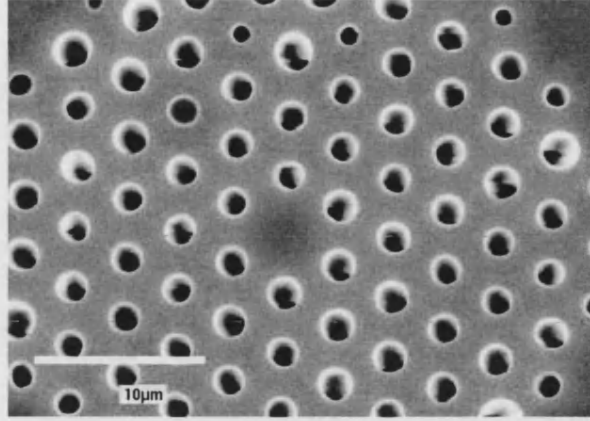
Figure 10.2: An SEM of the PCF under investigation.

The Stokes Spectra

The Brillouin spectra for each pump wavelength is shown in figure 10.3. The frequency shift at 1550nm was measured to be 11.07GHz which was intermediate to the frequency shift at 1530nm (10.93GHz) and 1570nm (11.22GHz), and was greater than the theoretical frequency shift (equation 9.12) of 10.85GHz.

It was shown by Boyd [61] that the lineshape $S(\omega)$, of the Stokes signal initiated by thermal noise in conventional fibres (see equation 10.1) evolves from a Lorentzian profile below threshold, $G \ll 1$, to a Gaussian above threshold, $G \gg 1$:

$$S(\omega) = \frac{8\pi\hbar\omega_s(\bar{n}+1)}{ncA_{eff}\Gamma} \left[\exp\left(\frac{G(\Gamma/2)^2}{\omega^2 + (\Gamma/2)^2} \right) - 1 \right].$$ (10.1)

Here Γ is the phonon decay rate, $\bar{n}$ is the mean number of phonons per mode of the elastic field, A_{eff} is the effective cross sectional area of the gain medium and the single pass gain G is defined as,

$$G = g_B I_L(0) L_{eff}.$$ (10.2)

This evolution in lineshape was also found to be true for PCF. In the undepleted pump high gain regime $(G \gg 1)$, the Gaussian form of equation 10.1 reveals as,

$$S(\omega) = \frac{8\pi\hbar\omega_s(\bar{n}+1)}{ncA\Gamma} \exp(G) \exp\left(-\frac{4G\omega^2}{\Gamma^2} \right)$$ (10.3)
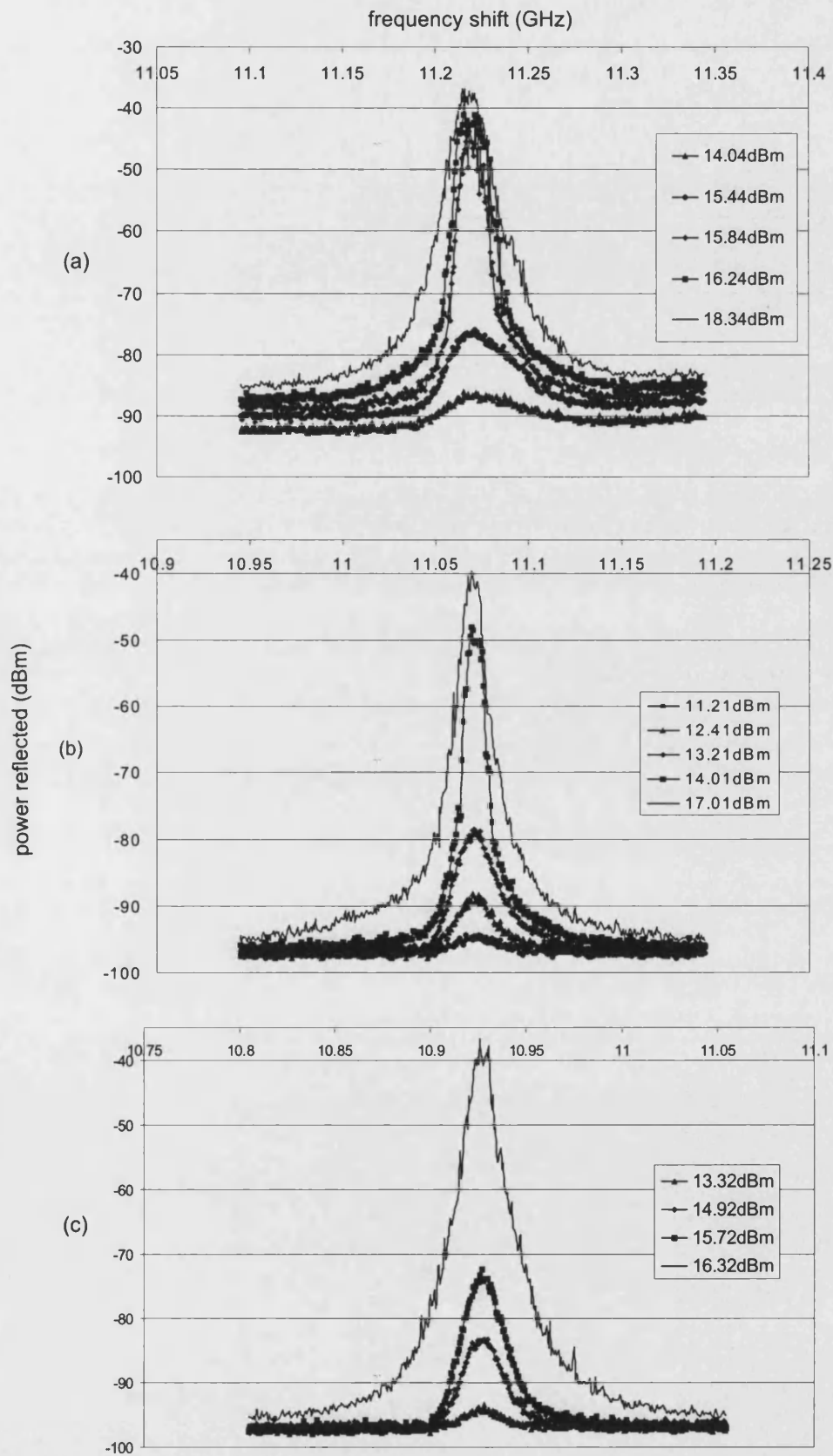
Figure 10.3: Brillouin spectra obtained from the PCF, recorded for different pump wavelengths. (a) 1530nm, (b) 1550nm and (c) 1570nm
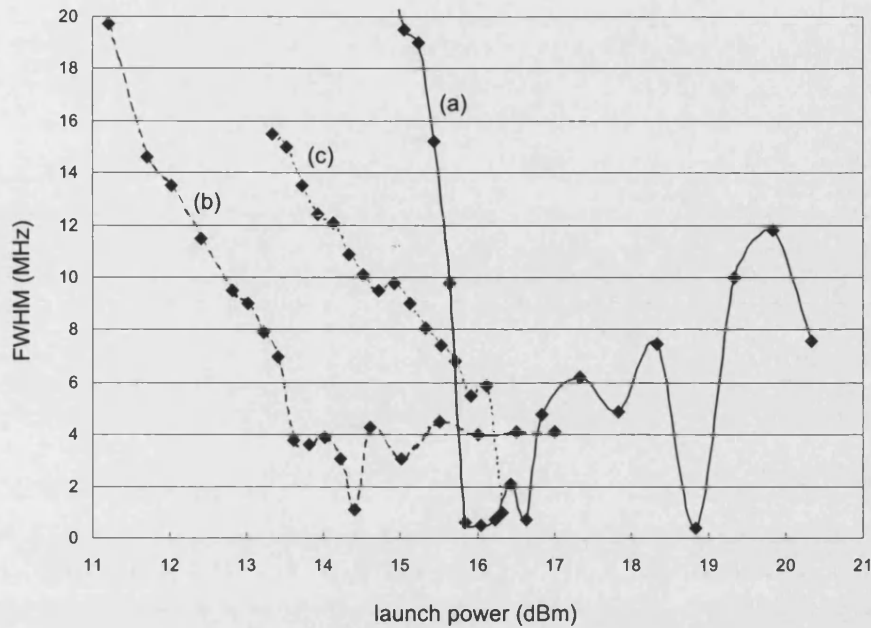
Figure 10.4: FWHM of Stokes spectra at (a) 1530nm (solid) (b) 1550nm (long dash) and (c) 1570nm (short dash).

which has a 3dB linewidth given by,

$$\Delta\omega = \Gamma \left(\frac{Ln(2)}{G} \right)^{1/2}. \tag{10.4}$$

The 3dB linewidth of the spectra shown in figure 10.3 was calculated by fitting a Lorentzian or Gaussian to the appropriate spectrum. The results are shown in figure 10.4 for increasing values of launch power.

As the launch power is increased the FWHM is seen to decrease and becomes more rapid as the threshold power is approached. Beyond threshold, the FWHM appears to fluctuate. The plot shows near coincidence of the threshold power at 1530nm and 1570nm ($\sim$37mW), whereas the curve at 1550nm suggests a lower threshold power ($\sim$22mW). The launch power (i.e the power entering the PCF) was estimated by noting the power output from the amplifier and the power transmitted through the PCF. By considering the combined loss in the system (i.e. fibre losses, splice losses etc) the coupling loss could be estimated and therefore the power launched into the PCF. However, this estimate assumed the coupling between the high NA fibre and PCF remained constant. The fact that the measured threshold power was lower at 1550nm than at 1530nm and 1570nm suggests that there was some discrepancy in the estimation of the coupling loss. Despite this, it is possible to calculate the lifetime of the phonons in

the PCF using 10.4. Assuming an effective area A_{eff}, of $\pi(2.6 \times 10^{-6})^2$ and an effective length of 408m, the lifetime of the phonons created with optical pump wavelength of 1550nm launched with a power of 17dBm and a linewidth of 4MHz, is calculated to be 2.9ns. This is similar to the previously recorded value by Wait [86] *et al.* of 1.5ns. The comparable lifetime of the phonons in this PCF as compared with conventional fibres suggest that these phonons are not guided by a phononic band gap, since guidance would imply a longer phonon lifetime.

SBS Threshold and Lasing

The threshold power is best determined by analysing the variation in transmitted and reflected power with launch power. There are a number of definitions of the threshold power for SBS in optical fibres. These include (i) the input optical power at which the reflected power equals the input power, (ii) the input power at which the reflected and transmitted powers are equal and (iii) the input power at which the reflected power begins to increase rapidly and the transmitted power begins to plateau. The first of these seems impractical since it implies that the reflected power is about to exceed the power input. The definition used here is the latter of the three. The power reflected from and transmitted through the PCF were recorded as the input power was increased. The results are shown in figure 10.5 for 1530nm, 1550nm and 1570nm.

Figure 10.5a shows a rapid increase in the reflected power at $\sim$42mW and is accompanied by a more shallow slope to the transmitted power. At 1550nm, the reflected power is seen to rise sharply at $\sim$37mW whilst the knee in the transmitted power occurs at a lower launch power of $\sim$22mW. The result at 1570nm is consistent with that at 1530nm; the threshold for SBS appears to be at 37mW.

The apparent lack of trend in the measured transmitted and reflected powers and their lack of agreement of the threshold, was the cause of some concern. This was particularly the case for the results shown in figure 10.5a (note the larger axis scale as compared with 10.5b and c); the transmitted and reflected powers showed no definite correspondence or trend typical of the Brillouin process, particularly for high launch powers.

This was initially thought to be due to variations in the coupling alignment (as evident in figure 10.5b), however, the threshold power for this fibre was also influenced by the Fresnel reflection of the forward and backward going beams at the end facets of the fibre. The fibre ends were cleaved perpendicularly to the fibre axis and so provided $\sim 4\%$ reflection. This reflection was found to be sufficient to cause the fibre to lase
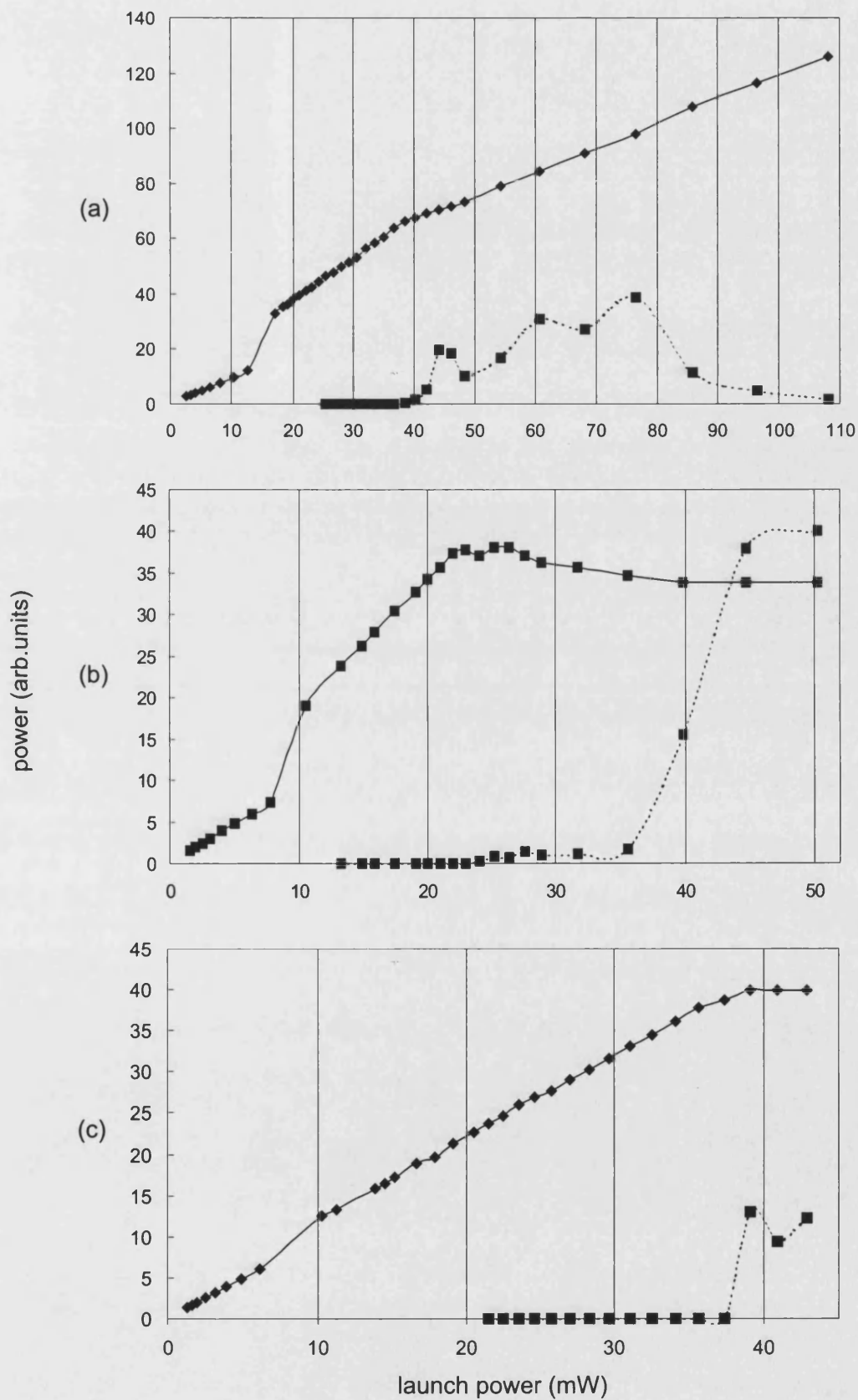
Figure 10.5: Plots showing power reflected from (dashed line) and transmitted through (solid line) the PCF using a (a) 1530nm (b) 1550nm and (c) 1570nm pump.

88

(even though the fibre loss was ~ 10 times that of conventional SMF) and thus, was thought to be the cause of the instability in the transmitted powers of figures 10.5a-c and the variation in FWHM measurements shown in figure 10.4.

Dammig [69] has studied the influence of feedback on SBS by controlling the amount of feedback within a fibre. This was achieved by placing the fibre end opposite to the power coupling end, in oils of varying refractive index, to control the level of index matching. In addition, the fibre end was glued to a mirror to significantly increase the feedback. The Stokes spectra output from the fibre was shown to include oscillations which had a period determined by the round trip time. Over longer timescales, the amplitude of the periodic oscillation was found to fluctuate. This is because the amplification of one lasing mode gives rise to an increased pump depletion which diminishes the amplification of a subsequent mode.

Gaeta [70] has also studied the effect of feedback on SBS and has found that the threshold for SBS in the presence of feedback can be lower than the threshold for SBS involving only a single pass of the Stokes signal through the fibre.

Figure 10.6a gives an expanded view (in a window of 20MHz) of the peak of the Stokes signal generated with a launch power of 13.8dBm and a wavelength of 1550nm.

Figure 10.6b shows the cavity modes at the peak of the Stokes signal in a narrower window of 1.2MHz. These cavity modes are characteristic of a laser and are separated by the free spectral range (FSR) of the PCF. The FSR is given by,

$$FSR = \frac{c}{2nd} \tag{10.5}$$

where c is the speed of light in a vacuum, n the refractive index of the medium (i.e. silica) and d is the separation of the end facets (i.e. the length of the fibre). The theoretical FSR of the fibre was calculated to be 214kHz using equation 10.5, and is found to be in excellent agreement with the experimental result; the separation of the lasing modes as measured using the electrical spectrum analyser was 217kHz.

The theoretical threshold power for stimulated scattering can be calculated using equation 9.6 and is found to be 35mW, which is in close agreement with the experimentally derived value. However, the inset to figure 10.6b reveals how index matching the end of the PCF causes a 10 fold decrease in the gain of the Brillouin signal. (Since PCF is a holey fibre, when the fibre is index matched in oil, the oil quickly moves through the holes in the fibre destroying its waveguiding ability. In order to reduce the feedback in
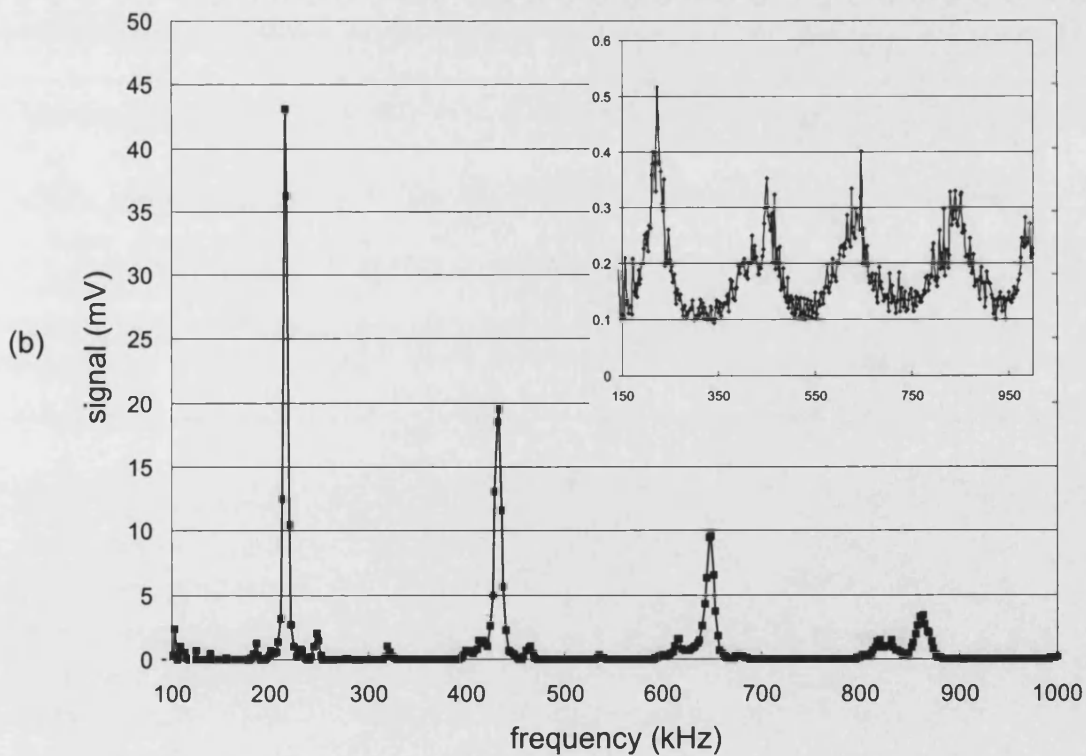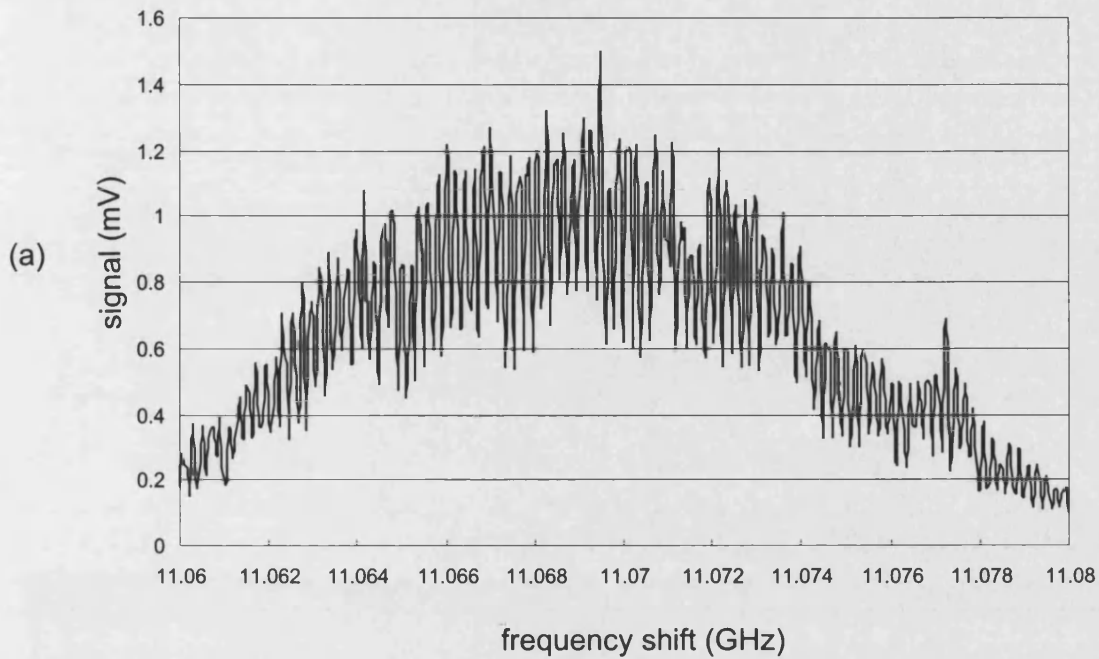
Figure 10.6: (a) Magnified plot of the peak of the Stokes signal generated with a wavelength of 1550nm and a launch power of 13.8dBm. (b) Lasing modes of the PCF at 1550nm. The inset corresponds to the same operating conditions, but with the end of the PCF index matched to a fluid. The lasing modes are still present but on a greatly reduced scale.
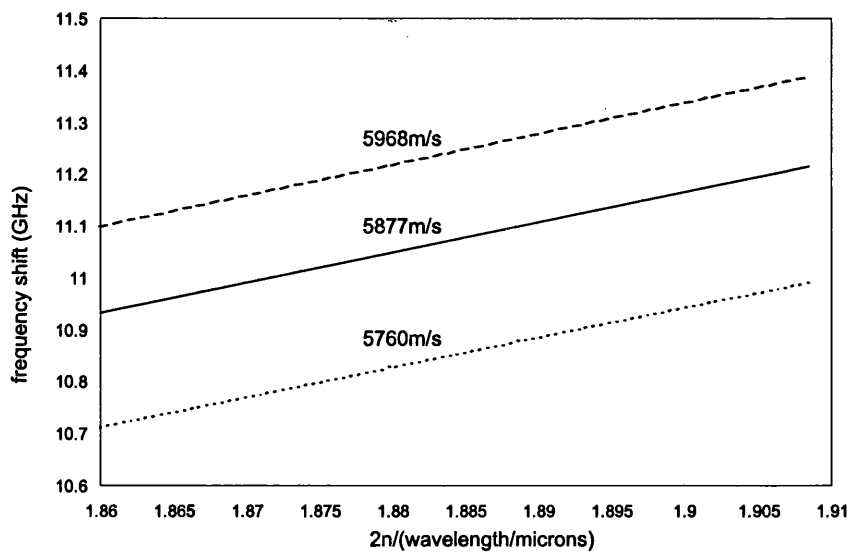
Figure 10.7: Plot to determine the phase velocity of the elastic mode responsible for Brillouin scattering (solid line). For comparison the frequency shift is calculated for elastic waves in bulk silica (long dash) and for a silica rod (short dash).

PCF it is better to angle cleave the end of the fibre.)

The spectra shown in figure 10.3 are asymmetric with respect to the centre frequency. This raised pedestal on the high frequency side is more noticeable at the shorter wavelength and is thought to be due to higher order elastic modes, which will of course have a faster phase velocity. This is possible with the PCF structure despite the reverse condition on density contrast between the core and effective cladding density for total internal reflection; the periodic structure provides an alternative guidance mechanism through the phononic band gap, which is insensitive to the sign of the density variation (the optical analogue being the hollow core PCF).

Given the frequency shift it is possible to calculate the phase velocity of the elastic mode that participates in Brillouin scattering using equation 9.12. Figure 10.7 gives a plot of the Brillouin shift as a function of inverse wavelength. The elastic wave phase velocity is calculated from the slope of the expected straight line and can be compared with the theoretical frequency shift expected in bulk silica ($v_E = 5968m/s$) and in a silica rod with the same diameter as the PCF core ($v_E = 5764m/s$). The figure shows the phase velocity of the elastic mode to be intermediate to that of bulk silica and rod waves.

Assuming the elastic wave is guided by a phononic band gap then the phase velocity of the mode would be expected to be similar to that for rod waves. Equation 10.6 gives the relationship between the phase velocity of the elastic waves in a rod and the rod

radius:

$$v_E = \sqrt{\frac{E}{\rho}} \left(1 - \sigma^2 \left(\frac{k_E r}{2} \right) \right). \tag{10.6}$$

Here E is Youngs Modulus and r is the radius of the rod. The measured phase velocity is lower than that of bulk silica but greater than rod waves. This suggests that the elastic wave sees a silica/air effective medium, with the holey region of the PCF lowering the effective density of the silica structure and thus the phase velocity of the elastic waves (see section 11.2), as compared with the phase velocity in bulk silica.

Thus, from the foregoing measurements of the Stokes spectra, phonon lifetime and elastic wave phase velocity, it suggests that the elastic waves are not guided within this PCF.

10.2   The Fabry-Perot Method

The results shown in section 10.1 were obtained whilst working at Lehigh University, Pennsylvania, USA. This section describes Brillouin scattering using a set-up constructed at Bath University, UK. Unfortunately, the 1550nm diode laser used at Lehigh was unavailable for the experimental set-up at Bath and so the Brillouin measurements obtained and discussed here refer to the use of a Kr-Ion laser operating at a wavelength of 647nm.

The Fabry-Perot (F-P) interferometer was the first instrument used to analyse Brillouin scattering in optical fibres. It has the advantage that the system is relatively easy to set up, but has the disadvantage that frequency resolutions better than a few MHz are difficult to achieve. There are many varieties of F-P interferometers, each designed for specific applications. The most studied arrangement consists of two plane, parallel, highly reflecting surfaces separated by some distance d. When both mirrors are fixed, the F-P is known as an etalon, but if one of the mirrors can move with respect to the other it is said to be an interferometer. The system used here to measure the Brillouin shift consisted of the latter arrangement with the reflecting surfaces defining an air cavity. The reflecting surfaces were dielectric mirrors each having a reflectivity of $\sim$ 99.5% at 647nm, and provided a theoretical resolving power of 80MHz and a finesse of 625. Unfortunately, neither of these specifications could be realised due to mirror surface contamination by dust and other airborne particles and so in practice a finesse of only 100 was attainable, corresponding to a minimum resolvable bandwidth of $\sim$
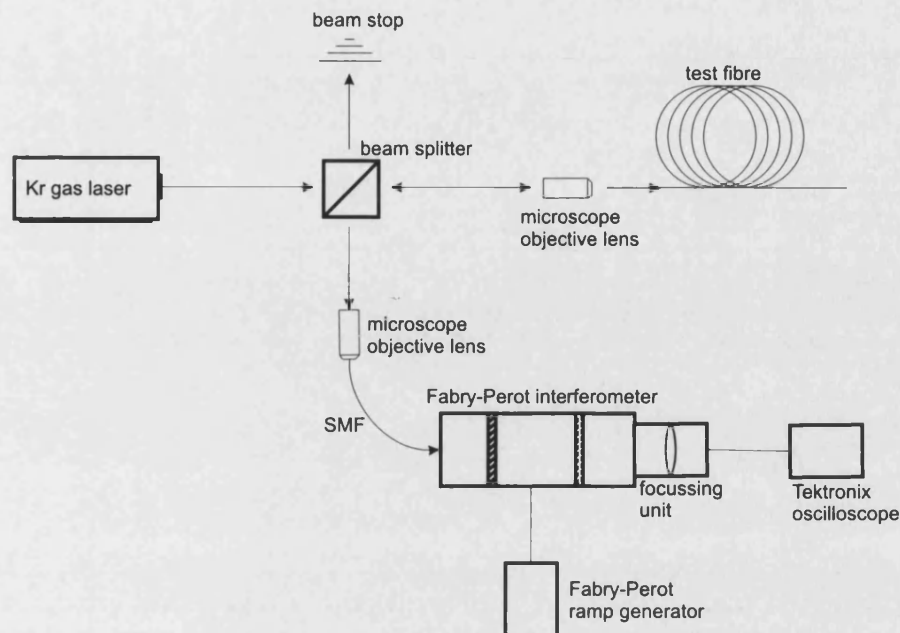
Figure 10.8: Experimental system for measuring the Brillouin shift in optical fibre using a Fabry-Perot Interferometer

350MHz.

The experimental set-up is shown in figure 10.8. The Kr-gas laser was operated at 647nm in single frequency operation.

A single laser line will consist of a number of closely spaced frequency components, but in single frequency operation all but one of these components can be suppressed with the use of an intra-cavity etalon. The etalon was used to filter out unwanted longitudinal modes from lasing and so reduced the linewidth of the laser to $\sim$ 30MHz thereby providing sufficient gain to the Brillouin signal (see equation 9.9). Higher order transverse modes were removed by carefully selecting the size of the intra-cavity aperture which exploited the smaller diameter of the TEM_{00} mode.

The laser beam was split at a 50:50 beam splitter (BS) with the forward going beam being coupled into the test fibre via an iris (which blocked any stray beams) and a microscope objective lens. The beam reflected from the BS was diffused in the closed unit of a beam stop. The Stokes signal together with the elastically scattered light which were reflected back out of the front facet of the test fibre were captured by the same objective lens and coupled into a short piece of single mode fibre (SMF) via the BS and second objective lens. The SMF stripped the laser beam of any higher order spatial modes, effectively cleaning the beam. This beam was then passed through the centre of the F-P cavity and focussed onto a Si-detector with the focussing unit.

The mirrors were scanned using the FPI-25 Ramp Generator, which also allowed for any fine adjustments to be made to the alignment of the two mirrors with the incident beam. The Brillouin signal was recorded for increasing values of laser power to track the progression from the spontaneous to the stimulated regime.

The output from the Si-detector was analysed with a Tektronix oscilloscope. This provided a means of measuring the Brillouin shift relative to the FSR using the timescale of the instrument. Given these values it is possible to calculate the Brillouin frequency shift (ν_B) using equation 10.7, once the absolute frequency is known for the FSR of the F-P cavity (FSR_f):

$$\frac{\nu_B}{FSR_f} = \frac{t_B}{FSR_t}.$$ (10.7)

Here, t_B and FSR_t represent the Brillouin shift and cavity FSR as measured using the timescale of the oscilloscope. The error associated with the Brillouin frequency shift ($\Delta\nu_B$) has contributions from the error associated with each of the three independent variables in equation 10.7, and is given by,

$$\Delta\nu_B = \frac{t_B}{FSR_t}|\Delta FSR_f| + \frac{FSR_f}{FSR_t}|\Delta t_B| + \frac{t_B FSR_f}{(FSR_t)^2}|\Delta FSR_t|$$ (10.8)

where ΔFSR_f signifies the error associated with the frequency measurement of the cavity FSR etc.

10.2.1 Calibration of the Fabry-Perot Cavity

In order to deduce the Brillouin frequency shift it is necessary to determine the FSR of the F-P cavity. Once the FSR is known, the frequency shift measurement can be calculated from equation 10.7. The FSR of the F-P is inversely proportional to the refractive index (n) of the medium between the mirrors, and to the mirror separation (d), as shown in equation 10.5. The calibration therefore reduces to that of finding the mirror separation since the cavity medium was air, which has a refractive index of approximately 1.

The mirror separation was measured with the instrument set up as an etalon i.e with the mirrors fixed. When used as an interferometer, the separation will of course vary as the mirrors are scanned. Each scan was found to produce approximately 5 transmission
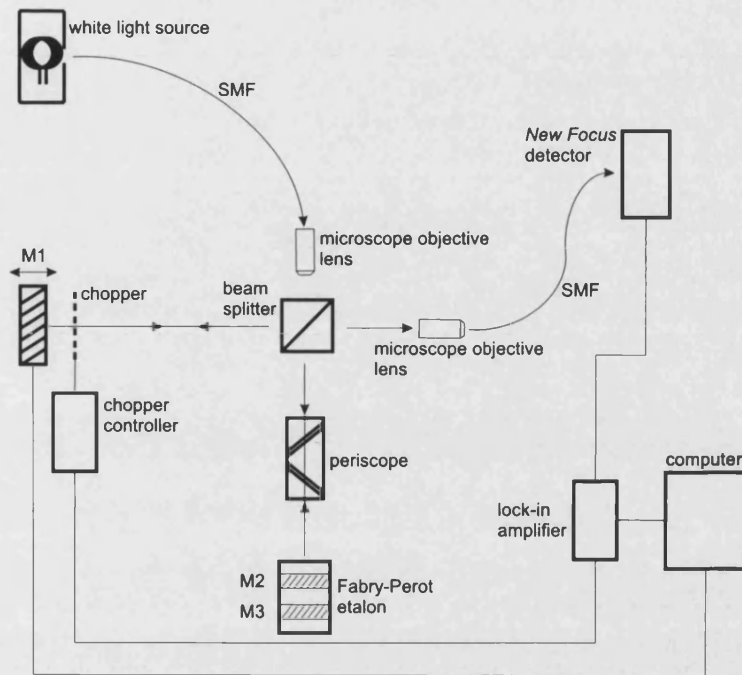
Figure 10.9: Experimental system for calibrating the F-P interferometer

orders which corresponds to 2 wavelengths and therefore a scan range of approximately 1.3μm. This variation from the measured fixed spacing manifests as an error in the overall measurement of the frequency shift, but can be minimised if the frequency shift is measured with respect to the first transmission order of the scan.

The fixed mirror spacing was measured by placing the F-P into one arm of a Michelson interferometer as shown in figure 10.9. The probing signal was derived from a white light source (S) which was passed through a filter to provide 10nm of necessary bandwidth in order to produce the interference fringes. This signal was split by a BS with 50% of the light passing through towards the F-P etalon and the remaining 50% toward a mirror M1 which could move to adjust the optical path length in that arm.

The inclusion of the periscope in the etalon arm was necessary as the F-P working height was above the plane of the BS and mirror M1. The mirrors comprising the periscope were metallic; this ensured there was no phase change on reflection and therefore no requirement for a similar periscope in the arm with mirror M1. The signals returning from mirror M1 and the mirrors of the F-P etalon (M2 and M3) were then recombined at the BS and coupled into a short piece of SMF, which passed the signal to a *New Focus* detector. This measurement was controlled by a chopper (placed in one arm of the interferometer) and a lock-in-amplifier which synchronously sampled the signal with the chopper, thereby reducing background levels of light in the measured signal.

Mirror M1 was mounted on a calibrated threaded bar such that a given rotation of the bar generated a specified translational movement of the mirror along it. The bar rotation was controlled by the computer which periodically stepped mirror M1 along the bar thereby allowing the interference signal to be recorded at each step in the translational range of M1.

It is well known that the interference of the recombining signals will depend on the optical path length difference in each arm. When this difference is zero, the signal in each arm will recombine and interfere constructively giving a large resultant signal. Conversely, when the optical path lengths are unequal the signals from each arm will interfere giving a very small signal. The interference of the recombining signal will also depend on the phase change dispersion occurring when radiations of different wavelengths (10nm bandwidth) are reflected at the surface of the dielectric mirrors of the Fabry-Perot [71]. The signal reflected from the surface of each mirror, M2 and M3, will undergo a phase change, which is equivalent to an apparent displacement of the mirror with respect to its true position. It is assumed that the phase change upon reflection from each mirror of the Fabry-Perot will be the same. Therefore, while it is difficult to ascertain their exact position from the BS, their relative separation can be accurately deduced.

The mirrors of the etalon were initially separated by approximately 5mm, as estimated by eye. This mirror separation was chosen prior to the calibration process to ensure the Brillouin shifted signal could be easily related to the correct transmission order of the F-P interferometer, and not overlap higher orders which would create confusion in the frequency shift measurement. The translational range of the mirror M1 was 25mm and so was sufficient to capture the condition of zero path length difference from each mirror of the F-P etalon in a single sweep.

The calibration was performed using wavelength filters of 850nm, 1000nm and without a wavelength filter, i.e. the white light source. It was necessary to choose a probing wavelength away from the high reflectivity bandwidth of the mirrors to allow sufficient signal to reach the rear mirror and participate in the interference of the recombined signal. The results are shown in figure 10.10. There are two sets of strong interference fringes and a third weaker set of fringes evident in each of the measurements. The first set of fringes correspond to the zero path length condition from the front mirror (M2) of the F-P etalon and the second set of fringes to the rear mirror (M3). The third set corresponds to a reflection from the rear mirror followed by a single round trip across the cavity before returning to the BS.

The mirror separation is derived from figure 10.10 by calculating the distance between the central peak of each set of fringes, and was found to be 4.044±0.009mm when an
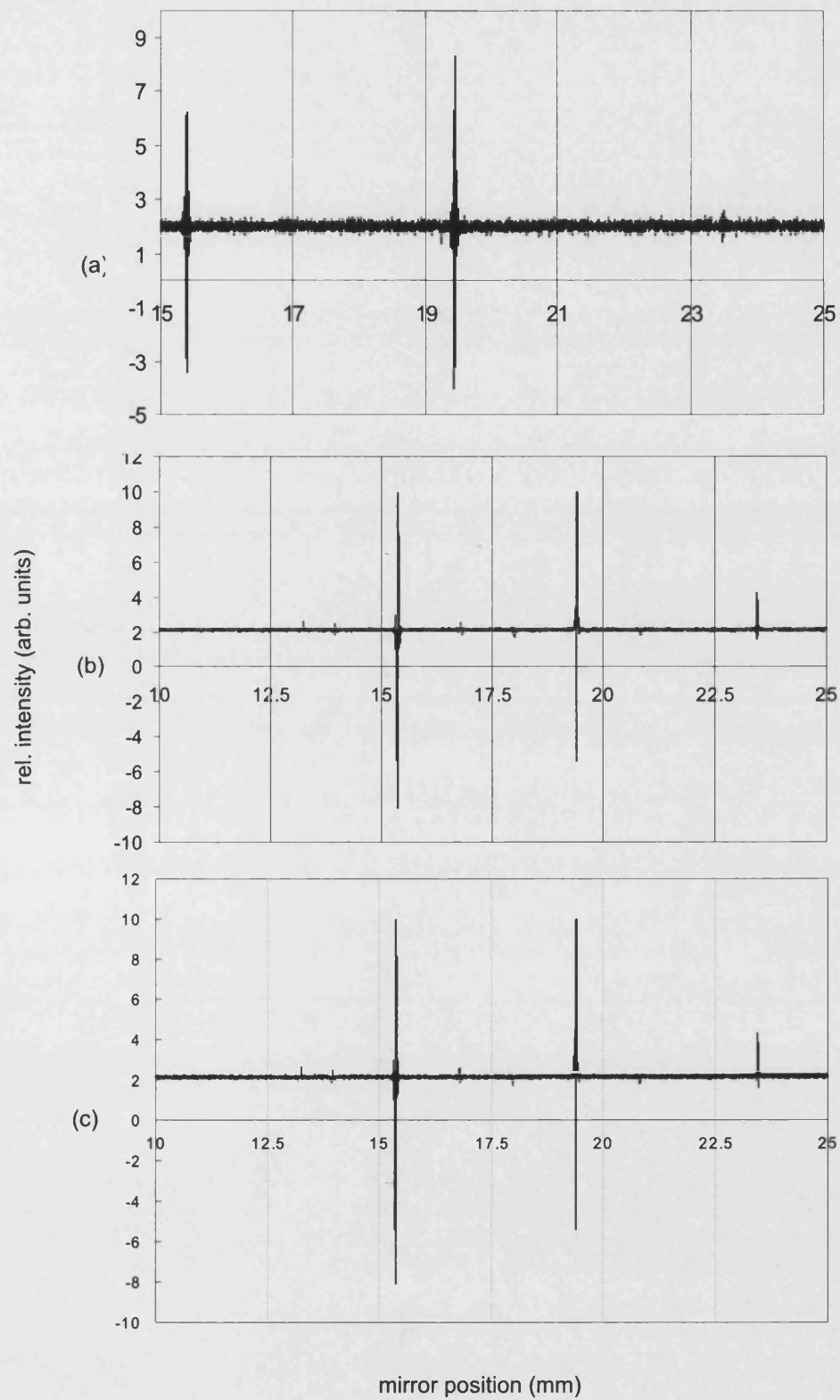
Figure 10.10: Calibration fringe patterns obtained using (a) 850nm filter, (b) 1000nm filter and (c) the white light source.

Fibre	Length(m)	Core diameter(μm)	Loss @ 647nm(dB/km)	Brillouin Shift(GHz)
Pirelli	3000	9	5	25.73±0.12
1	80	2.23	38	26.55±0.27
2	75	2.25	56	26.71±0.28
3	80	2.11	50	26.54±0.28
4	80	2.04	84	26.44±0.26
5	80	1.89	81	26.47±0.27
6	75	2.32	40	26.49±0.12
7	80	2.34	59	26.55±0.13
8	80	2.2	70	26.33±0.12
9	90	3.7	40	26.45±0.28
10	1130	2.5	51	26.57±0.28
11	130	1.2	130	26.04±0.38
12	110	1.1	130	25.86±0.38
13	120	1.1	140	25.8±0.38
14	115	1.1	150	25.82±0.38

Table 10.1: Table characterising the fibres analysed.

average is taken of each set of results. The variation in mirror separation obtained with the different probe signals was the major source of uncertainty in this calibration. The positioning of the mirror M1 along the threaded bar was accurate to within 0.1μm and the centre of the fringe pattern could be determined to an accuracy better than 1μm. The uncertainty in d is related to an uncertainty in the FSR as shown below.

$$|\Delta FSR| = \frac{c}{2nd^2}|\Delta d|. \tag{10.9}$$

Thus, using equations 10.5 and 10.9, the FSR of the F-P was calculated to be 37.09±0.08GHz.

10.2.2 Results

The minimum resolvable bandwidth of $\sim$350MHz of the F-P was too large to measure the Stokes linewidths which is of the order of 10's of MHz, so instead, the experiment concentrated on the frequency shift. This shift was measured for fourteen different PCF's which differed in core diameter and air-filling fraction, and also for a conventional single mode fibre which had a small concentration of Ge in the core (*Pirelli* SMF). The PCF's analysed had a length of 75-1130m, a loss of typically 70dB/km and a core size in the range from $\sim$1.1μm to $\sim$3.7μm. The results are shown in figure 10.11 and summarised in table 10.1.
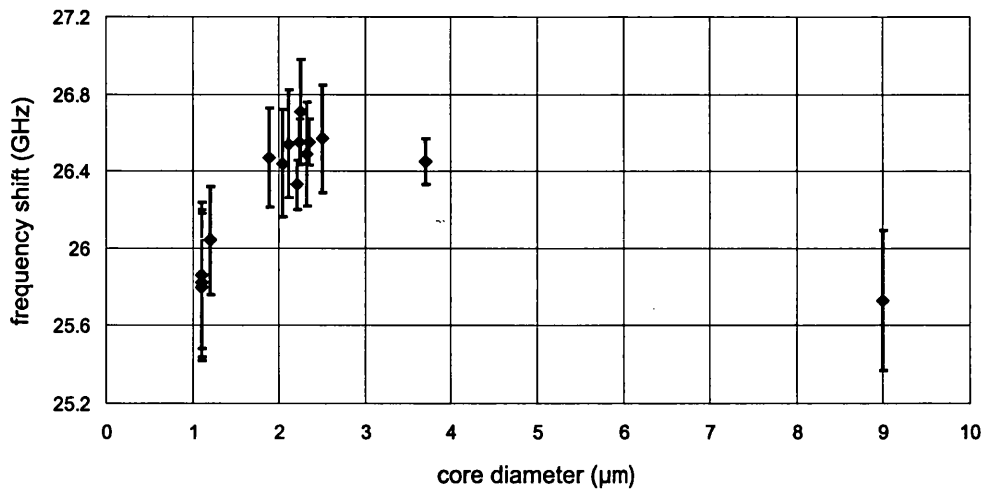
Figure 10.11: Plot showing the measured frequency shifts from 14 test PCF's and a conventional SMF (shown with the red point).

Fibres 1-14 of table 10.1 are made solely of fused silica whilst the *Pirelli* fibre had a fused silica core doped with a small concentration of Ge to provide the necessary index contrast for total internal reflection. Furthermore, fibres 11-14 which had a small core were so-called "cobweb" fibres because the silica bridges supporting the core at the centre of the cladding are very thin, reminiscent of a spiders web. Accordingly, these fibres had a very large air-filling fraction as compared with fibres 1-10.

The development of stop-bands (and thus the means for elastic wave guidance) is known to depend on the density contrast between the materials as well as the relative thickness of the materials which form the stop-band, as shown in Part I of this thesis. As a result, it would seem instructive to use the ratio $\frac{d}{\Lambda}$ as the control parameter in characterising SBS in PCF, where d is the diameter of the holes of the cladding of the PCF and Λ is the hole spacing. However, the core diameter was chosen as the control parameter to allow for the direct comparison of the experimental results with a theoretical model for the Brillouin frequency shift in PCF as described in chapter 11.

The frequency shift associated with the fibres having a core diameter $\sim 2\mu$m was measured to be ~ 750MHz greater than the SMF. The theoretical frequency shift at this wavelength (647nm) for a silica fibre is 25.99GHz (assuming a refractive index for silica of 1.46), which is still ~ 500MHz lower than the frequency shifts measured for the above-mentioned PCF's. For fibres which had a small core ($< 1.5\mu$m), the frequency shift was comparable to the SMF of 25.7GHz.

The oscilloscope traces obtained by scanning the F-P, were also found to contain a second smaller peak occurring at a frequency of approximately 9.7GHz, as shown in figure 10.12. This frequency shift corresponds to an elastic wave phase velocity of
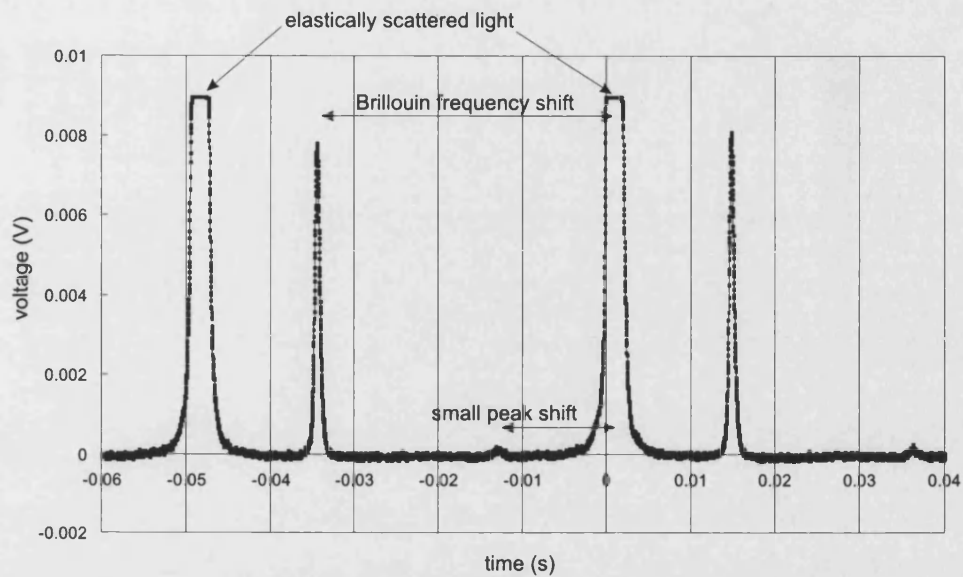
Figure 10.12: The oscilloscope trace as the mirrors of the F-P move through a distance of half a wavelength. The Stokes line and second smaller peak are seen between the peaks produced by the elastically backscattered light (shown clipped).

approximately 2150m/s, using equation 9.12, which is not typical of S waves or L waves in silica. This peak increased and decreased in accordance to the main Stokes line and was evident in the Pirelli fibre as well as the PCF's. The fibres analysed in this experiment were not single mode at 647nm and so it is thought that this smaller peak may be due to Brillouin scattering from a higher order optical mode in the fibres.

Chapter 11

Estimating the Brillouin Shift in Photonic Crystal Fibre

Chapter 11 describes a model used to estimate the Brillouin frequency shift in photonic crystal fibre and is based on the dispersion of compressional modes and the fundamental optical HE_{11} mode of a free silica rod.

It was shown in the previous chapter that the Brillouin frequency shift in those PCF's characterised in table 10.1 is greater than in conventional optical fibre and thus greater than what conventional theory predicts.

To speak of an elastic mode implies that the elastic field is quantised by the finite transverse dimensions of a waveguide and therefore, becomes guided by it. However, the previous chapter did not present any conclusive evidence of a phononic band gap which could have guided the elastic wave in the core of the PCF and since the density contrast is reversed for total internal reflection within the core, it is unlikely the elastic wave was guided within the fibre.

It is thought that a useful approximation to the interaction of elastic waves in the core of a PCF with the optical modes can be achieved by considering the simplified system of a silica rod in a vacuum. Brillouin scattering is dominated by the fundamental optical mode (HE_{11}) and so in modelling the frequency shift it is sufficient to consider the dispersion of the HE_{11} mode only. Given this dependence between ω and β it is possible to calculate the phase matching β value of the elastic mode (for a given operating optical pump frequency) responsible for coupling the forward propagating optical pump wave into the backward propagating Stokes wave and thus from the dispersion relation for the elastic waves, the expected frequency shift.

Figure 11.1: Schematic illustration of the orientation of the silica rod.
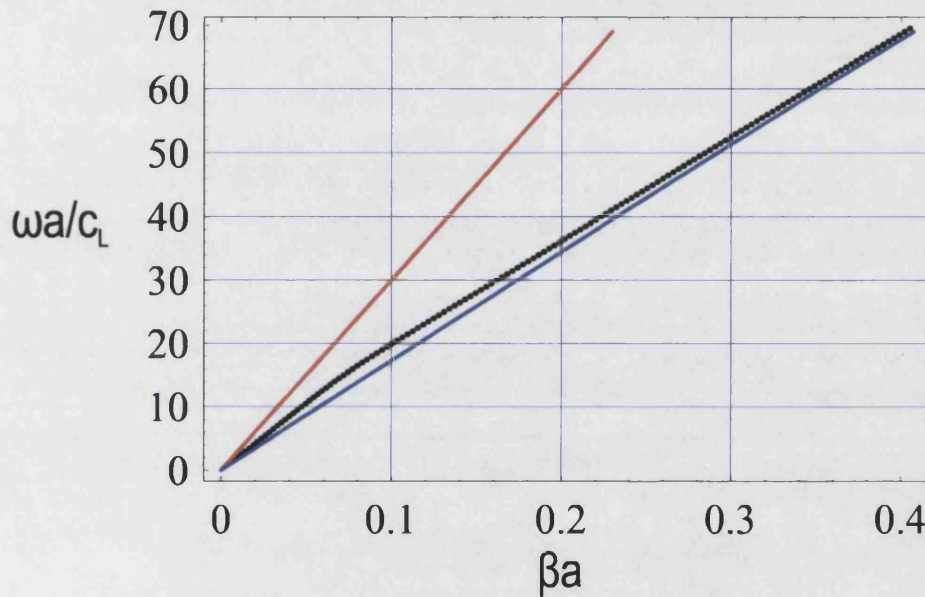
Figure 11.2: Dispersion of the fundamental HE_{11} mode of a silica rod of diameter $1.1\mu m$ (black line) at low frequency. The dispersion of EM waves in a vacuum and bulk silica is shown with the red and blue lines, respectively.

The orientation of the silica rod in question is shown in figure 11.1 and is described using cylindrical polar coordinates, (r, θ, z). Since this step-profiled waveguide (assumed infinite in length) is modelled as being in a vacuum, the dispersion relations for the EM and elastic waves will involve satisfying Neumann and Dirichlet boundary conditions respectively.

The dispersion relation for the optical modes of a free silica rod is derived in appendix B and the dispersion of the fundamental HE_{11} mode is shown in figure 11.2 in the long wavelength limit. The mode can be traced to $\omega = 0$ since there is no cut-off for the fundamental mode. The red line corresponds the dispersion of EM waves in a vacuum (i.e. $\omega/\beta = c$) and the blue line corresponds to the dispersion of EM waves in bulk silica ($\omega/\beta = c/n_{Si}(\omega)$).

Figure 11.2 only includes positive β values and therefore represents waves propagating towards infinity. The Stokes wave will of course be propagating in the opposite sense and so the magnitude of the β value of the elastic wave which couples the forward going pump to the backward going Stokes signal can be approximated as being twice the β value of the pump wave at the operating frequency of the pump. This is a good approximation since the frequency of the elastic wave is ~ 5 orders of magnitude smaller than the frequency of the pump and Stokes waves.

11.1 Dispersion of Elastic Waves in a Free Silica Rod

The calculation of the dispersion of elastic waves in a cylindrical waveguide [87], [88] proceeds in a manner similar to that employed in section 6.1.2 for a low density layer. In contrast to EM waves, the elastic waves will be totally confined to the waveguide since no physical disturbance can be supported in a vacuum. Thus, the discretisation of modes is produced by the boundary conditions which require the normal components of the stress tensor to be zero at the boundary to the vacuum.

The displacement vector $\mathbf{U}$, is derived from the scalar potential ϕ and vector potential $\mathbf{\Psi}$ as shown in section 2.2. For propagation along the rod axis (z), it is convenient to use cylindrical polar coordinates. In this case, equations 2.23 and 2.24 become,

$$\nabla^2 \phi - \frac{1}{c_L^2}\frac{\partial^2 \phi}{\partial t^2} = \left(\frac{\partial^2}{\partial r^2} + \frac{1}{r}\frac{\partial}{\partial r} + \frac{1}{r^2}\frac{\partial^2}{\partial \theta^2} + \frac{\partial^2}{\partial z^2} \right)\phi - \frac{1}{c_L^2}\frac{\partial^2 \phi}{\partial t^2} = 0 \qquad (11.1)$$

$$\nabla^2 \mathbf{\Psi} - \frac{1}{c_S^2}\frac{\partial^2 \mathbf{\Psi}}{\partial t^2} = \nabla(\nabla . \mathbf{\Psi}) - \nabla \times (\nabla \times \mathbf{\Psi}) - \frac{1}{c_S^2}\frac{\partial^2 \mathbf{\Psi}}{\partial t^2} = 0 \qquad (11.2)$$

The general solution to equation 11.1 can be written in the form,

$$\phi(r, \theta, z) = R(r)\Theta(\theta)\exp[-i(\beta z - \omega t)] \qquad (11.3)$$

and when substituted in 11.1, the equation for ϕ splits in two parts,

$$\frac{d^2 R}{dr^2} + \frac{1}{r}\frac{dR}{dr} + R(r)\left(\frac{\omega^2}{c_L^2} - \beta^2 \right) - R(r)\frac{m^2}{r^2} = 0 \qquad (11.4)$$

$$\frac{d^2\Theta}{d\theta^2} + m^2\Theta(\theta) = 0. \tag{11.5}$$

The Laplacian of the vector field $\boldsymbol{\Psi}$ (11.2), in cylindrical coordinates is shown below

$$\nabla^2\psi_r - \frac{\psi_r}{r^2} - \frac{2}{r^2}\frac{\partial\psi_\theta}{\partial\theta} + \frac{\omega^2}{c_S^2}\psi_r = 0 \tag{11.6}$$

$$\nabla^2\psi_\theta - \frac{\psi_\theta}{r^2} + \frac{2}{r^2}\frac{\partial\psi_r}{\partial\theta} + \frac{\omega^2}{c_S^2}\psi_\theta = 0 \tag{11.7}$$

$$\nabla^2\psi_z + \frac{\omega^2}{c_S^2}\psi_z = 0. \tag{11.8}$$

It is evident from the foregoing that ψ_r and ψ_θ are coupled and that solutions to 11.5 and 11.8 will take a similar form. The solutions of 11.5 are $\sin(m\theta)$ and $\cos(m\theta)$ where m is an integer to ensure continuity of $\Theta(\theta)$ circumferentially around the rod. Solutions to 11.4 are the well known Bessel functions and since the solutions must be finite at the coordinate origin the solutions will involve Bessel functions of the first kind only. Thus, equation 11.3 takes the form,

$$\phi = AJ_n(p_L r)\cos(m\theta)\exp{-i(\beta z - \omega t)} \tag{11.9}$$

and similarly, solutions to 11.8 are of the form,

$$\psi_z = BJ_n(p_S r)\sin(m\theta)\exp{-i(\beta z - \omega t)} \tag{11.10}$$

where A and B are constants to be determined from the boundary conditions.

The expressions for ψ_r and ψ_θ are, *a priori*, of the form

$$\psi_r = \psi_r(r)\sin(m\theta)\exp{-i(\beta z - \omega t)} \tag{11.11}$$

and

104

$$\psi_\theta = \psi_\theta(r) \cos(m\theta) \exp -i(\beta z - \omega t). \qquad (11.12)$$

The expression for ψ_r contains the term $\sin(m\theta)$ and the expression for ψ_θ contains the term $\cos(m\theta)$ because the coupling terms in equations 11.6 and 11.7 have differentials with respect to θ with different signs. Substituting equations 11.11 and 11.12 in equations 11.6 and 11.7 respectively, gives,

$$\frac{d^2\psi_r}{dr^2} + \frac{1}{r}\frac{d\psi_r}{dr} + \frac{1}{r^2}(-m^2\psi_r + 2m\psi_\theta - \psi_r) + p_s^2\psi_r = 0 \qquad (11.13)$$

$$\frac{d^2\psi_\theta}{dr^2} + \frac{1}{r}\frac{d\psi_\theta}{dr} + \frac{1}{r^2}(-m^2\psi_\theta + 2m\psi_r - \psi_\theta) + p_s^2\psi_\theta = 0. \qquad (11.14)$$

Adding and subtracting equations 11.13 and 11.14 gives two new equations whose solutions are,

$$\psi_r + \psi_\theta = 2DJ_{n-1}(p_S r) \qquad (11.15)$$

and

$$\psi_r - \psi_\theta = 2CJ_{n+1}(p_S r). \qquad (11.16)$$

Imposing the condition $\psi_r = -\psi_\theta$ gives $D = 0$ and so solutions to equations 11.13 and 11.14, together with the solutions for ϕ and ψ_z become,

$$\phi = AJ_n(p_L r) \cos(m\theta) \exp -i(\beta z - \omega t) \qquad (11.17)$$

$$\psi_z = BJ_n(p_S r) \sin(m\theta) \exp -i(\beta z - \omega t) \qquad (11.18)$$

$$\psi_r = CJ_{n+1}(p_S r) \sin(m\theta) \exp -i(\beta z - \omega t) \qquad (11.19)$$

$$\psi_\theta = -CJ_{n+1}(p_S r) \cos(m\theta) \exp -i(\beta z - \omega t) \qquad (11.20)$$

where A, B and C are unknown constants.

The components of the displacement (U_r along r, U_θ along θ and U_z along z) follow from 11.17-11.20 (see section 2.3) and are given below.

$$U_r = \frac{\partial \phi}{\partial r} + \frac{1}{r}\frac{\partial \psi_z}{\partial \theta} - \frac{\partial \psi_\theta}{\partial z} \qquad (11.21)$$

$$U_\theta = \frac{1}{r}\frac{\partial \phi}{\partial \theta} + \frac{\partial \psi_r}{\partial z} - \frac{\partial \psi_z}{\partial r} \qquad (11.22)$$

$$U_z = \frac{\partial \phi}{\partial z} + \frac{1}{r}\frac{\partial (r\psi_\theta)}{\partial r} - \frac{1}{r}\frac{\partial \psi_r}{\partial \theta}. \qquad (11.23)$$

The boundary conditions require the stress components normal to the surface of the rod ($T_{rr}, T_{r\theta}$ and T_{rz}) be zero at the surface ($r = a$). The stresses are given in respect of the aforementioned displacement components and the Lamé constants λ and μ, as shown below,

$$T_{rr} = \lambda S + 2\mu \frac{\partial U_r}{\partial r} \qquad (11.24)$$

$$T_{r\theta} = \mu \left[\frac{1}{r} \left(\frac{\partial U_r}{\partial \theta} - U_\theta \right) + \frac{\partial U_\theta}{\partial r} \right] \qquad (11.25)$$

$$T_{rz} = \mu \left(\frac{\partial U_r}{\partial z} + \frac{\partial U_z}{\partial r} \right) \qquad (11.26)$$

where S is the local dilatation given by,

$$S = \nabla \cdot \mathbf{U} = \frac{1}{r}\frac{\partial (rU_r)}{\partial r} + \frac{1}{r}\frac{\partial U_\theta}{\partial \theta} + \frac{\partial U_z}{\partial z}. \qquad (11.27)$$

Setting the three stress components to zero at the free surface of the rod ($r = a$), yields three linear homogeneous equations in the three unknowns A, B and C. Non-zero solutions exist only if the determinant of the coefficients is zero. The resulting expression relating ω to β and the circumferential order m gives the dispersion relation of the elastic waves in a rod.

For any m and real β there are an infinite number of roots i.e. modes, propagating along the z-coordinate. By virtue of the displacement components, these modes can be classified into three families: (i) *compressional modes* - these modes are axially symmetric with displacement components U_r and U_z that are independent of θ, (ii) *torsional modes* - waves which only possess a circumferential displacement U_θ that is independent of θ and r, and (iii) *flexural modes* - this family has displacement

components U_r, U_θ and U_z which are all dependent on r, θ and z.

The dispersion of elastic modes is determined by forming the matrix of coefficients A, B and C of equations 11.24, 11.25 and 11.26, and calculating the determinant of this matrix. The resulting equation will be a function of ω, β and the integer m. The essential features of compressional and torsional modes are conveniently presented with $m = 0$ and for flexural waves with $m = 1$. Therefore, by setting the necessary displacements to zero, the dispersion of each family of modes can be analysed separately, as shown in figure 11.3. Figure 11.3 presents the dispersion of the compressional, torsional and flexural waves in a free silica rod of diameter 1.1μm; the red and blue linear lines correspond to the dispersion of the L and S waves in bulk silica, respectively.

11.2 The Frequency Shift

Given the dispersion characteristics of the elastic modes, it is possible to determine the frequency of those modes which phase match the pump to the Stokes wave. Each phase matched mode can theoretically scatter the pump wave into the Stokes however, the strength of the scattering will depend on the overlap between the displacement profile of the elastic wave and the displacement created by the energy profile from the interference of the pump and Stokes waves through the process of electrostriction. It is this overlap which is important since the density variation within the rod created through electrostriction provides the gain to the elastic wave.

Assuming the interference of the pump and Stokes waves to have a Gaussian energy profile, as shown in equation 11.28,

$$E = E_O \exp - \left(\frac{r}{a}\right)^2 \tag{11.28}$$

the electrostrictive force on the medium of the rod is given by,

$$F = -\nabla E = \left(\frac{2r}{a}\right) E_O \exp - \left(\frac{r}{a}\right)^2 = E'_O r \exp - \left(\frac{r}{a}\right)^2 \tag{11.29}$$

and is directly proportional to the displacement that it produces. Thus, the modal overlap (C_i) as discussed above is given by,
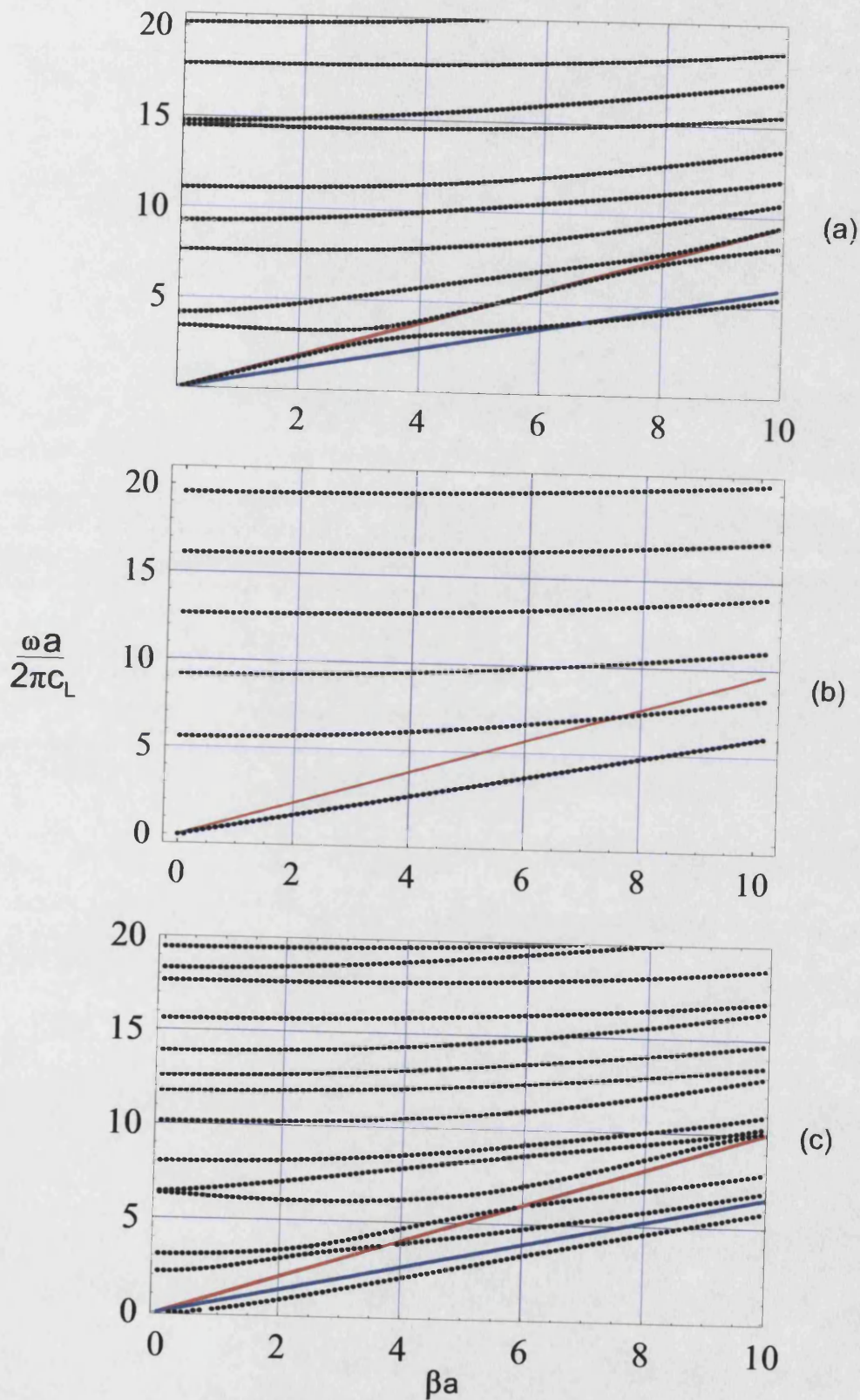
Figure 11.3: Dispersion of (a) compressional waves, (b) torsional waves and (c) flexural waves, in a rod with a diameter of $1.1\mu m$. The red and blue lines correspond to the dispersion of the L and S waves in bulk silica.

$$C_i = \int_0^a U^n_{elastic} \cdot U^n_{optical} r \, dr \qquad (11.30)$$

where i is the modal number and $U^n_{elastic}$ and $U^n_{optical}$ are the normalised displacements as calculated using,

$$U^n = \frac{U}{[\int_0^a U \cdot U^* r \, dr]^{\frac{1}{2}}}. \qquad (11.31)$$

The pump wave is scattered from the refractive index grating induced in the rod by the passage of the elastic wave. Only those modes which produce a volume change are capable of creating the grating and so the problem reduces essentially to the consideration of compressional modes. The torsional modes produce a shearing displacement (U_θ) without creating a local volume change and thus a change in the refractive index. Flexural modes (U_r, U_θ, U_z) will produce a slight volume change although this will be less than than that created the by the passage of the compressional modes.

At a pump operating wavelength of 647nm the phase matching β value as determined from the optical dispersion of the HE_{11} mode has a normalised value of 28.29 and this was found to remain approximately constant for rod diameters from 0.1μm to 5μm.

Taking this phase matching β value, it is possible to determine the frequency of the elastic modes in a given diameter silica rod which are capable of participating in Brillouin scattering. For example, the dispersion of the first few compressional modes at this phase matching β value is shown in figure 11.4 for a 1.1μm diameter silica rod. The intersection of each modal dispersion curve with the dashed red line gives the theoretical Brillouin frequency shift for that particular mode. However, the dominant mode responsible for Brillouin scattering will depend on the overlap between the displacement profile of the compressional mode and the interference pattern of the forward propagating pump and backward propagating Stokes waves.

Figure 11.5 shows the normalised displacement profile and intensity profile of the phase matched compressional modes shown in figure 11.4.

For a 1.1μm diameter rod the dominant mode responsible for Brillouin scattering is predicted to occur at a frequency of 26.88GHz, as determined from the overlap integral (equation 11.30), and is shown in figure 11.6. This is to be compared with an experimentally measured frequency shift of 25.86 ± 0.38GHz in a PCF with a core diameter of 1.1μm.
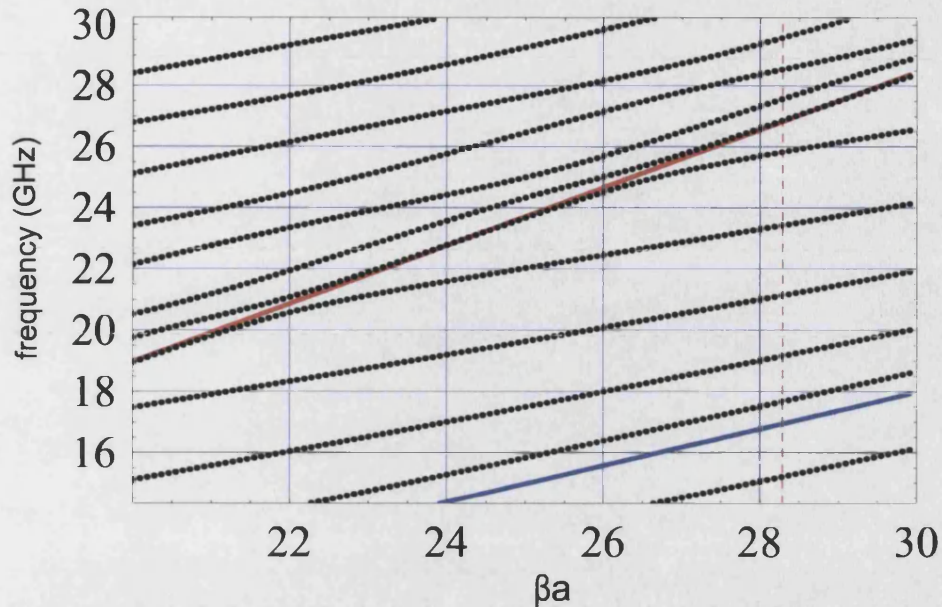
Figure 11.4: Dispersion of compressional waves that phase match the pump to the Stokes wave in a rod with a diameter of $1.1\mu m$ (the normalised phase matching β value is indicated by the dashed red line). The solid red and blue lines correspond to the dispersion of the L and S waves, respectively, in bulk silica.

Figure 11.7 shows how the phase matching compressional modes develop in frequency as the diameter of the silica rod is varied. This plot was constructed by forming the matrix of coefficients A, B and C of equations 11.24, 11.25 and 11.26, and calculating the determinant of this matrix with $m = 0$, $U_\theta = 0$ and $\beta = 28.29$, as ω and rod diameter were varied. The propagating modes are revealed when the determinant of the matrix is 0. The red and blue lines of figure 11.7 correspond to the frequency of the L and S waves in bulk silica, as determined using the phase matching β value.

The acoustooptic overlap for rod diameters corresponding to each experimentally studied core diameter is shown in figure 11.8 and the results are summarised in figure 11.9. The graph shows the experimentally measured frequency values to be generally less than the modelled results. In addition, figure 11.9 reveals a subtle trend in the measured results in that as the core diameter decreases, so does the Brillouin frequency shift. This is markedly different from the predictions of the model which suggests the frequency shift should increase as the core diameter falls.

For core diameters less than $1\mu m$, figure 11.7 suggests that any elastic mode that becomes guided within the core of a PCF will be separated by large frequency intervals and so it is expected that the frequency shifts will deviate most significantly from the predictions of conventional theory for PCF's with core diameters $<1\mu m$.
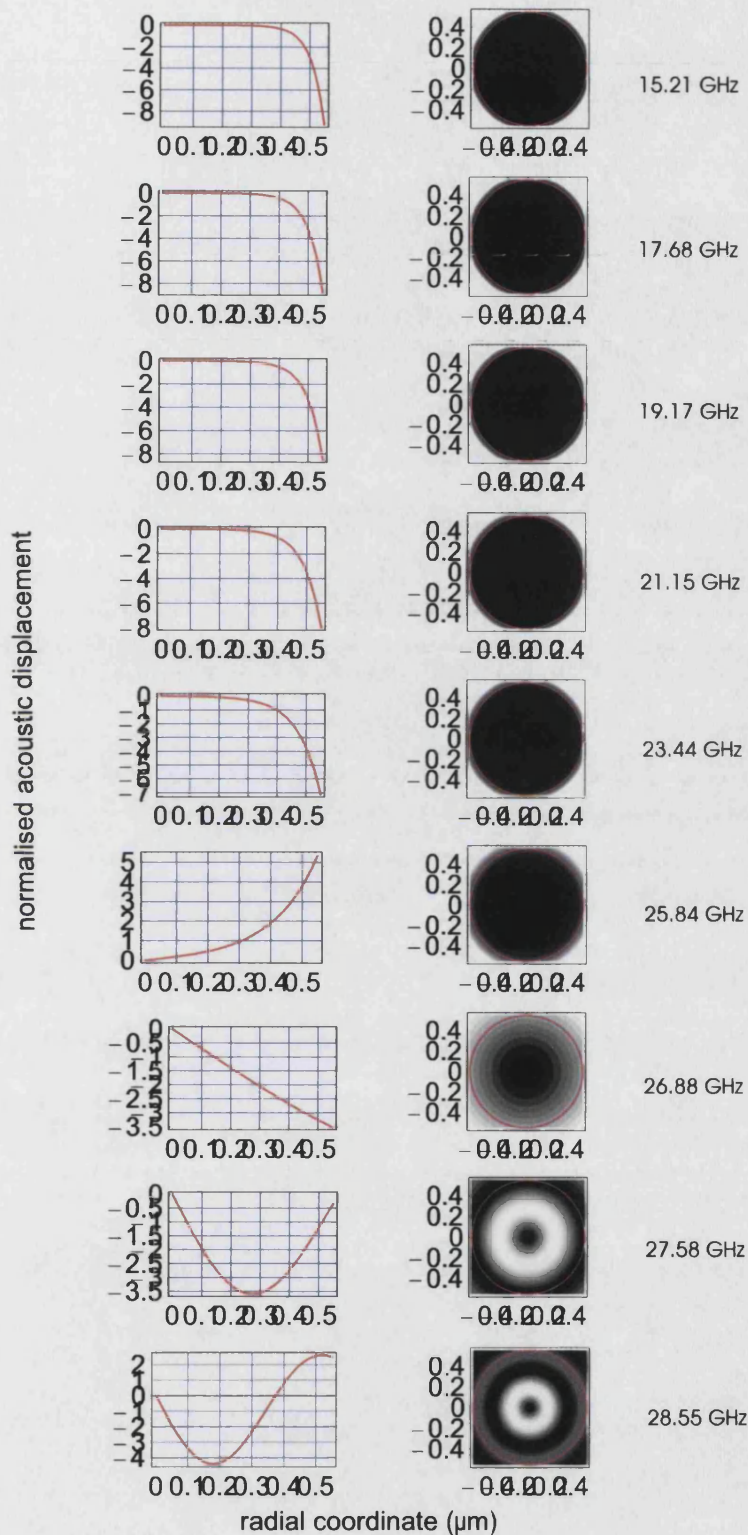
Figure 11.5: Plot showing the modal displacement profiles of the phase matched compressional modes shown in figure 11.4 as a function of the rod radial coordinate. The corresponding intensity profiles of the compressional modes are shown in the density plots opposite with the outer perimeter of the rod shown in red. Regions of high intensity are shown in white, whilst regions of the rod which experience a low intensity are shown in black. The corresponding frequency of the compressional mode is shown along side each profile.

111
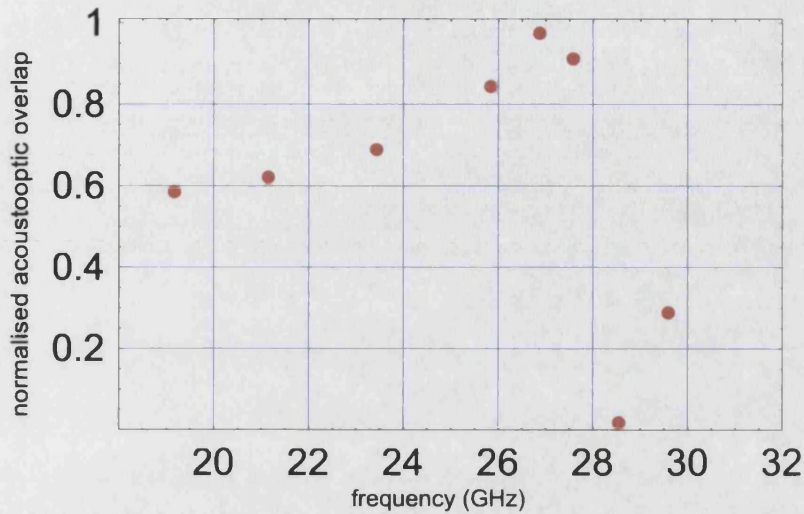
Figure 11.6: Plot showing the acoustooptic overlap for those phase matched elastic modes shown in figure 11.4 and 11.5, as a function of the elastic modal frequency.

Figure 11.7: Plot showing how the phase matching compressional modes develop in frequency as the rod diameter is varied (for a pump wavelength of 647nm). The red and blue lines correspond to the frequency of the L and S waves in bulk silica, respectively, as determined using the phase matching β value.

112
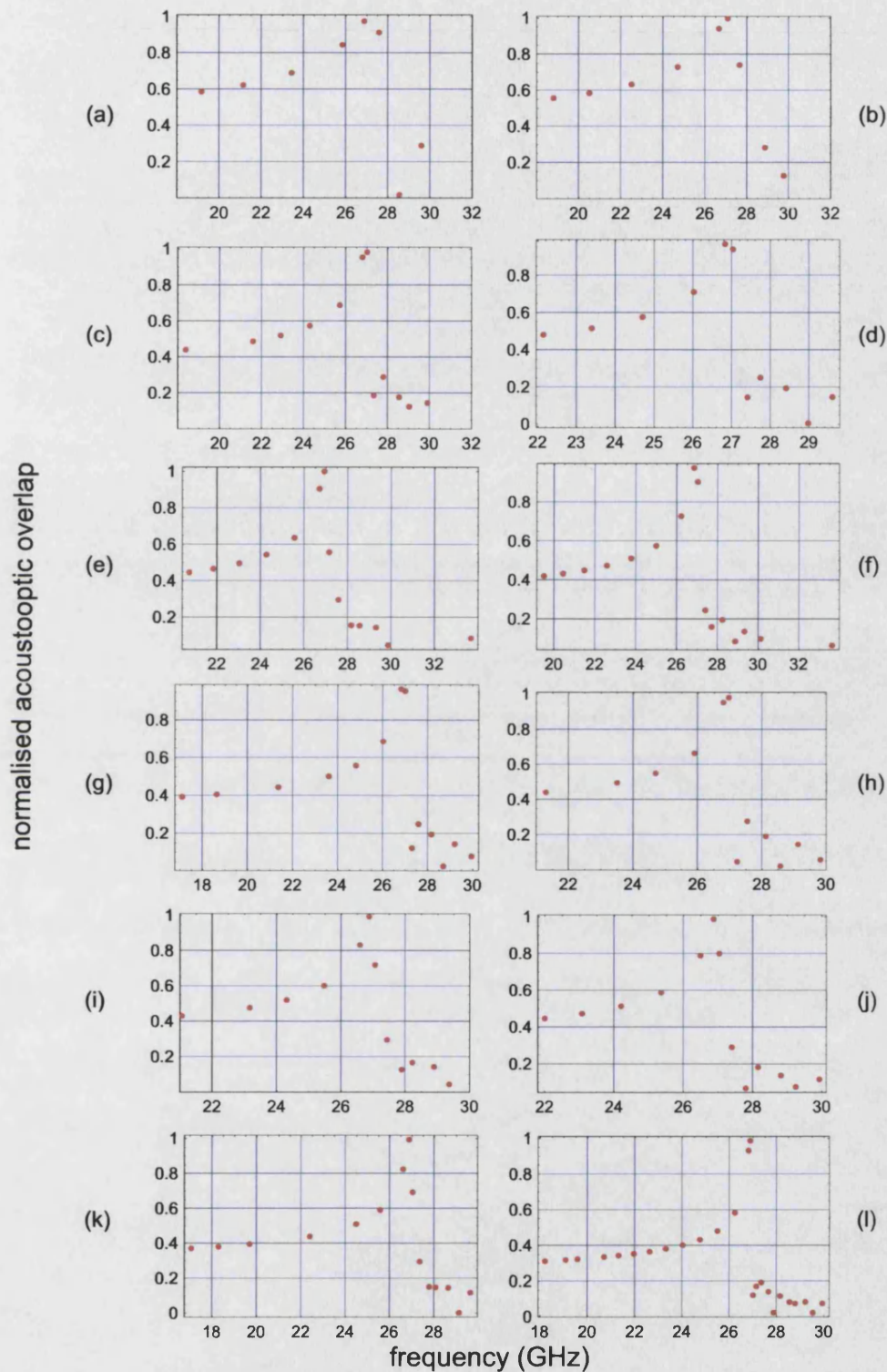
Figure 11.8: Plot showing the theoretical acoustooptic overlap in rods with diameters corresponding to the diameters of each experimentally studied PCF. (a) 1.1μm, (b) 1.2μm, (c) 1.89μm, (d) 2.04μm, (e) 2.11μm, (f) 2.2μm, (g) 2.23μm, (h) 2.25μm, (i) 2.32μm, (j) 2.34μm, (k) 2.5μm, (l) 3.7μm.

113

Figure 11.9: Plot showing the experimentally determined frequency shift measurements in PCF (black points), together with the modelled theoretical frequency shifts (red points) in rods with diameters corresponding to the PCF core diameters. In addition, the predicted frequency shift in PCF's with core diameters of 0.25μm, 0.35μm and 0.5μm are shown.

The influence of the PCF core diameter on the Brillouin shift will become more noticeable when the wavelength of the optical waves involved in SBS become comparable to the core diameter, in addition to the elastic waves. In such favourable circumstances, the overlap between the optical energy profile and the elastic wave is better matched. Thus, using a pump wavelength of 647nm, it is necessary to launch light into a PCF with a core diameter of $\sim 0.7\mu$m to observe any significant frequency shift. However, with the experimental systems described in chapter 10, it is difficult to achieve a stable launch of the pump into small core PCF i.e. $<1\mu$m diameter, and therefore obtain a frequency shift measurement. In the circumstances it is better to use a pump wavelength of 1550nm and launch this pump into a PCF with a core diameter of $\sim 1.5\mu$m.

Figure 11.10 shows the theoretical dispersion of compressional modes in a 1.22μm diameter silica rod. The phase matching β value is shown with the dashed line; the solid red and blue lines correspond to the dispersion of the L and S waves in bulk silica at the phase matching β value.

The development of these phase matching modes in frequency, as the rod diameter is varied, is shown in figure 11.11 and the acoustooptic overlap of these modes with the fundamental optical mode is shown in figure 11.12.

Figure 11.12 suggests that several modes are almost *equally* capable of scattering the pump wave into the Stokes. This possibility of multiple scattering events is more

114
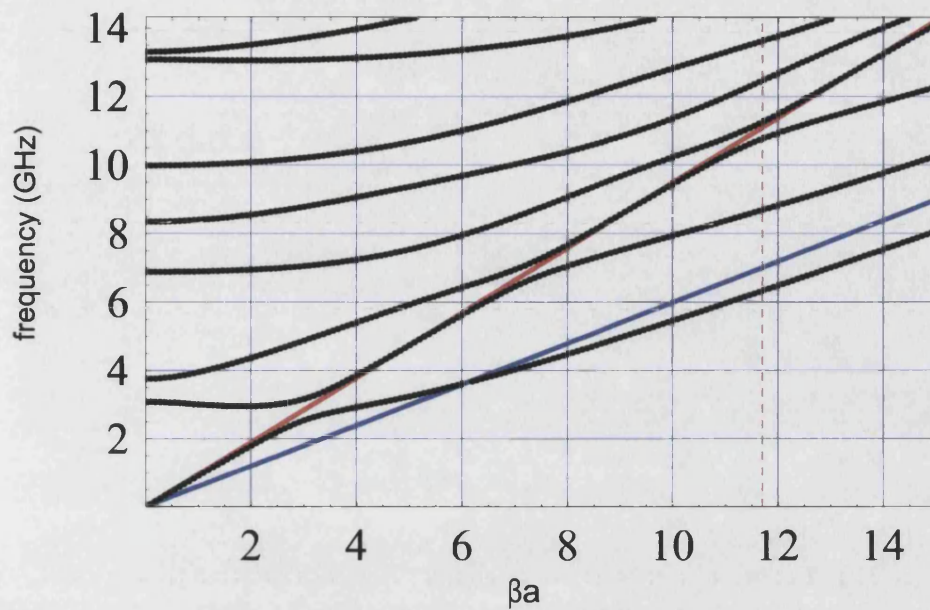
Figure 11.10: Dispersion of compressional waves in a silica rod of diameter 1.22μm. The dashed line indicates the β value of the compressional modes which phase match the 1550nm pump to the Stokes line. The solid red and blue lines correspond to the dispersion of the L and S waves in bulk silica, respectively.
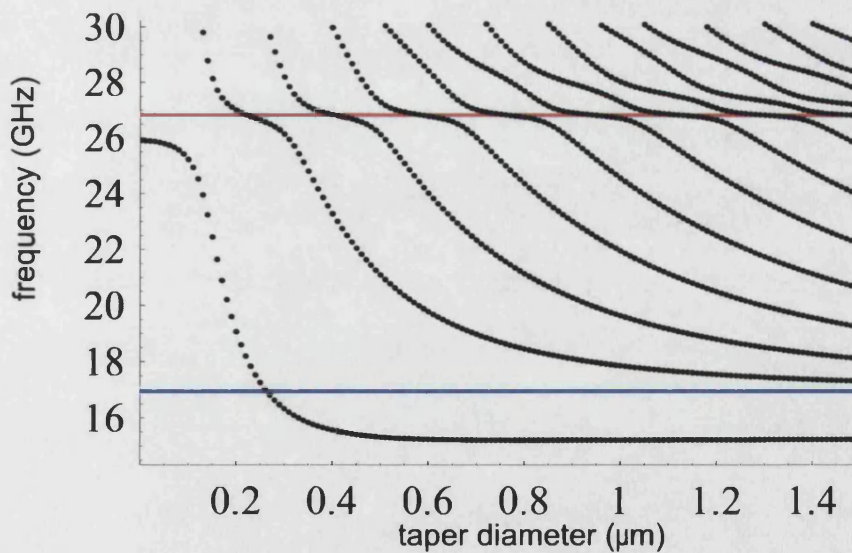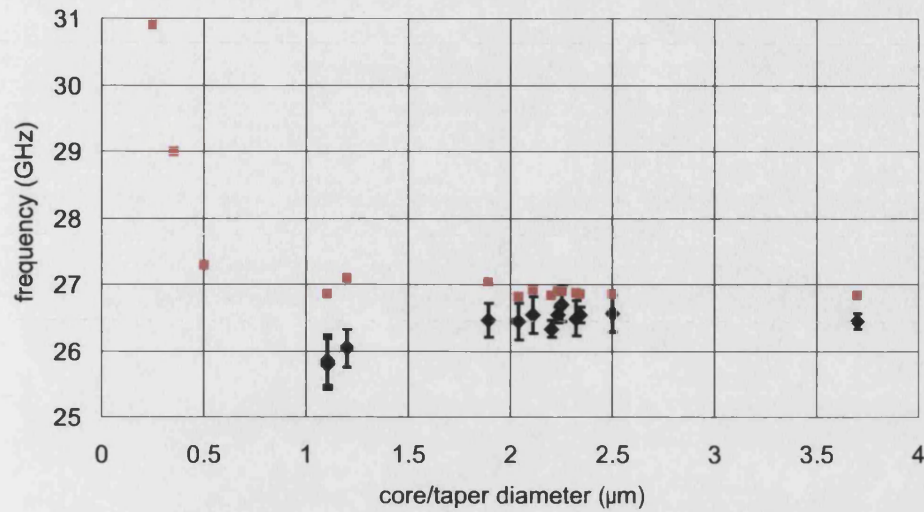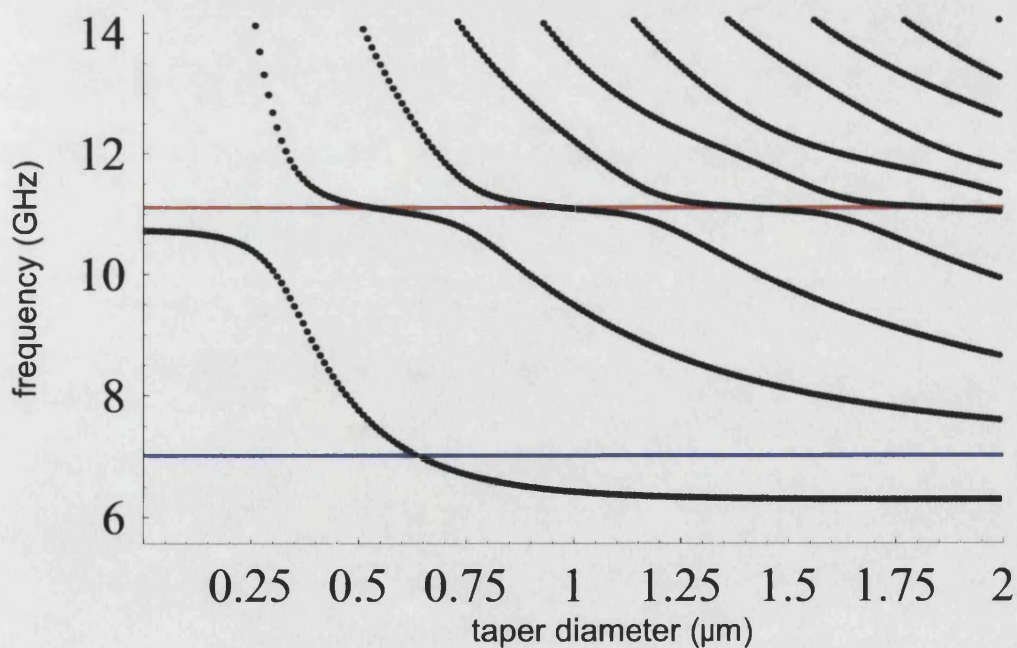

Figure 11.11: Plot showing how the phase matching compressional modes develop in frequency as the rod diameter is varied (for a pump wavelength of 1550nm). The red and blue lines correspond to the frequency of the L and S waves in bulk silica, respectively at this phase matching β value.

115
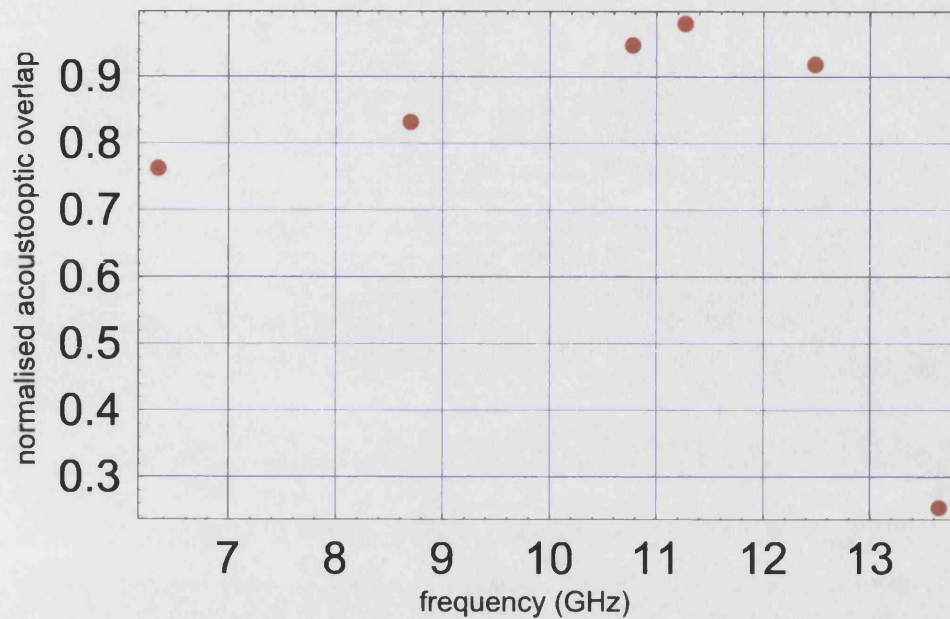
Figure 11.12: Plot showing the acoustooptic overlap for those phase matched elastic modes shown in figure 11.10, as a function of the elastic modal frequency.

pronounced than for a pump wavelength of 647nm as seen in figure 11.6. (In figure 11.12, four compressional modes exist which phase match the 1550nm pump to the Stokes with an acoustooptic overlap integral greater than 0.8 as compared with only two modes in an equivalent diameter rod (figure 11.6b) using a 647nm pump). The dominant compressional mode of figure 11.12 is modelled as occurring at a frequency of 11.27GHz, whilst successively dominant phase matched modes scatter the pump with a frequency shift of 10.78GHz and 12.48GHz with a scattering strength of 97% and 93%, of the dominant mode, respectively.

These predictions were compared with the frequency shift obtained experimentally with a 1550nm pump wave in a PCF with a core diameter of 1.22μm and 9.27μm. The PCF had a length of $\sim$110m and a loss of $\sim$33db/km @ 1550nm. The results were obtained using the heterodyne technique of section 10.1 and are shown in figure 11.13.

Figure 11.13a presents three peaks in the Brillouin spectrum, whilst figure 11.13b shows a single peak that is characteristic of Brillouin scattering in conventional fibre. The series of peaks in the small core PCF were measured at frequencies of 9.78GHz, 9.95GHz and 10.23GHz with respective strengths of $\sim$26% and $\sim$7% of the dominant scattering mode, while the large core fibre produced a single peak at 11.13GHz. The separation of these modes ($\sim$200MHz) shown in figure 11.13a, is such that it would have been difficult to resolve them using the Fabry-Perot interferometer of chapter 10.

It has been reported by Agrawal [63] that Brillouin spectra produced in fibres having a

116
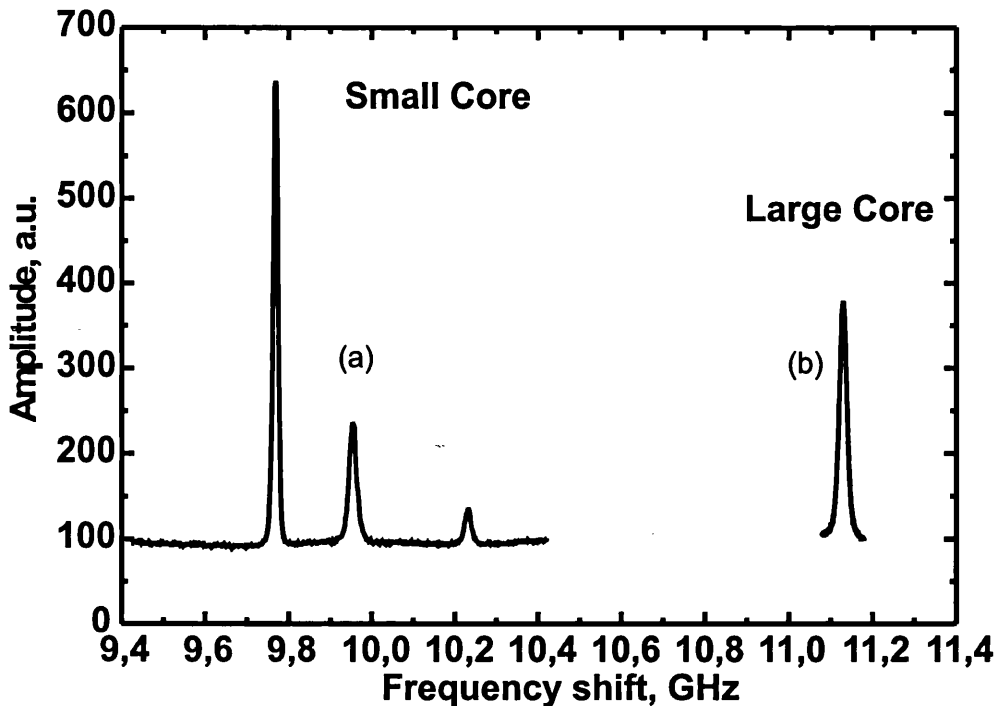
Figure 11.13: Spontaneous Brillouin spectrum obtained from a PCF with a core diameter of (a)1.22μm and (b)9.27μm, using a pump wavelength of 1550nm.

doped core can have multiple Brillouin peaks. The Brillouin spectra produced in fibres having an inhomogeneous distribution of germania within the core has been shown to produce two peaks separated by approximately 100MHz [89]. Thus, it could be speculated that the additional peaks in PCF are the result of an inhomogeneous stress distribution within the core or maybe the result of core contamination during manufacture. The possibility of multiple Brillouin scattering events, wherein the Brillouin signal is itself Brillouin shifted, could also be speculated, although in such circumstances the separation of the peaks would be expected to be approximately 9.8GHz.

The fibre which produced the Brillouin spectrum shown in figure 11.13a, was not single mode at 1550nm and so it is more probable that the presence of the two additional Brillouin peaks is due to Brillouin scattering from additional optical modes. In fact, the fibre was found to support a second family of higher order optical modes which were lossy at 1550nm - a feature which may account for the decrease in scattering strength with an increase in frequency.

Alternatively, the series of peaks may be considered to be due to the scattering of the pump wave by three elastic modes that are guided within the fibre by a phononic band gap. The silica rod model predicts the presence of three scattering events by three compressional modes, although it fails to accurately predict the measured frequency shifts.

The experimental results presented in this chapter and in chapter 10 do not allow for a reliable conclusion to be reached as to whether there is elastic wave guidance in this PCF. In considering the theoretical model, it could be concluded that the elastic waves are not guided within the core of the fibre, since there is no association of the modelled frequency shifts with the experimental results. However, the silica rod model is only an approximate representation of the core within PCF. In reality, the core of PCF is not circular in cross-section and is supported at the centre of the cladding by silica bridges, which will affect the motion of the core. Furthermore, the model only considers Brillouin scattering associated with compressional waves; flexural waves will also create a refractive index change within the PCF core (although to a lesser extent than compressional waves) and so will provide an additional scattering to the optical modes.

It is difficult to assess the influence of the variations of the model from actual PCF in order to conclude whether the series of Brillouin peaks are infact due to elastic wave guidance. The most likely reason for the series of Brillouin peaks seems to be the scattering of higher order optical modes within the fibre core. It would therefore be instructive to perform the same experiment in PCF which is single mode at 1550nm, in order to remove the uncertainty of higher order optical mode scattering, and run the silica rod model for that fibre and compare results.

Chapter 12

Consequence of Elastic Wave Guidance on the Threshold Power for Brillouin Scattering

Chapter 12 is directed to the understanding of how elastic wave guidance affects the threshold power for Brillouin scattering in photonic crystal fibre.

The threshold power for Brillouin scattering is an important quantity in fibre optic systems incorporating narrow bandwidth laser light, since it presents an upper limit to the maximum signal power that can be transmitted through the fibre, as demonstrated in the previous sections. The experimental arrangement used to determine this value is outlined in figure 12.1 and involved measuring the output power as a function of the launched power.

The laser source as illustrated in figure 12.1, was a *New Focus* tunable diode laser and was operated at 1550nm. Approximately 1mW of the signal from the diode laser was passed into a *Keopsys* (*EDFA*) fibre amplifier which could provide 30dB of gain. The output of the EDFA entered the circulator via port 1, which then passed the signal to port 2. The amplified signal was coupled into the test PCF via two microscope objective lenses that were mounted on precision translation stages back-to-back and the power output from the fibre was measured with a *Wandel Goltermann* power meter. Port 3 was used to channel the back reflected signal (combination of elastically scattered and Brillouin shifted signals) into an optical spectrum analyser to monitor the progress of the Stokes line as the launch power was increased.
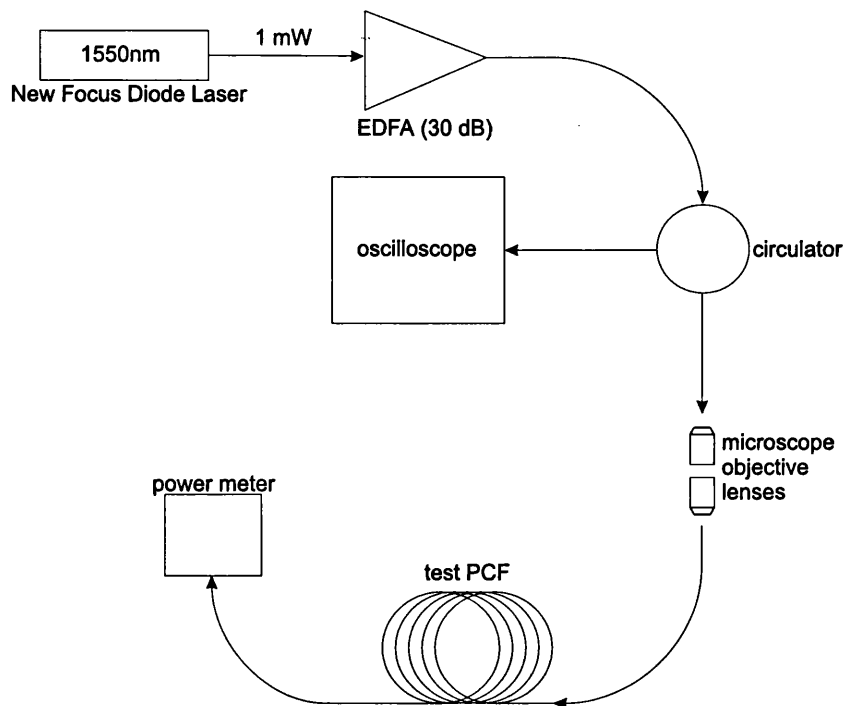
Figure 12.1: Experimental arrangement for measuring the threshold power for Brillouin scattering.

12.1 The Results

The typical variation of transmitted power with launch power is shown in figure 12.2a. As the launch power is increased the power transmitted through the fibre is also seen to increase, linearly at first, and then plateau for a given launch power, thereby indicating the threshold power for stimulated Brillouin scattering. Figure 12.2b shows the gain experienced by the Stokes line for a launch power, below, at, and above threshold. As the launch power is increased, the Stokes line can be seen to grow in intensity from a level below that of the elastically scattered light (no frequency change) to above the intensity levels of the elastically scattered light. It should be noted however, that the linewidth of the laser is significantly less than that shown in figure 12.2b. The linewidth shown in figure 12.2b is characteristic of the bandwidth of the optical spectrum analyser.

For each fibre studied, the power launched into the PCF was calculated by performing a cut-back and measuring the power output from approximately 1m of PCF. Knowing the losses that were accumulated before the coupling stage and the power output from the cut-back, the coupling loss could be estimated and thus the launched power. The core diameters of the PCF's studied ranged from 1.1-4.8μm and in addition to these, a conventional *Pirelli* SMF fibre with a core diameter of 9μm was used as a control.
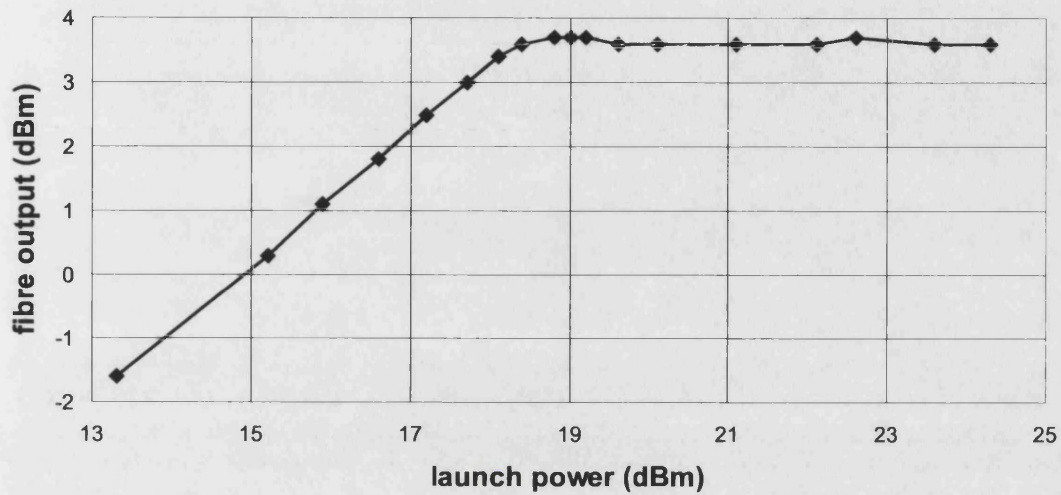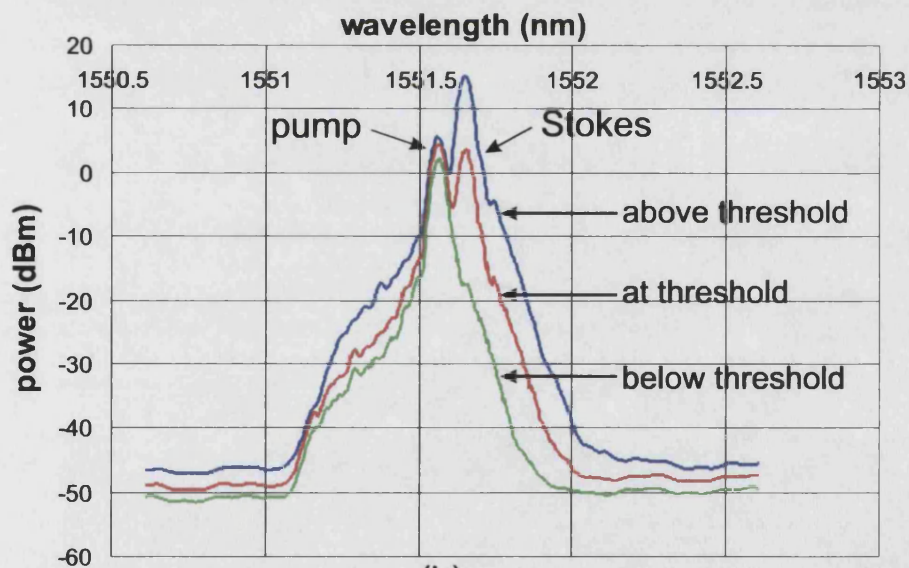
Figure 12.2: Plot showing how (a) the power transmitted through a test PCF, with a core diameter of 3.4μm, varies with the launch power and (b) the gain experienced by the Stokes line for three values of launch power.
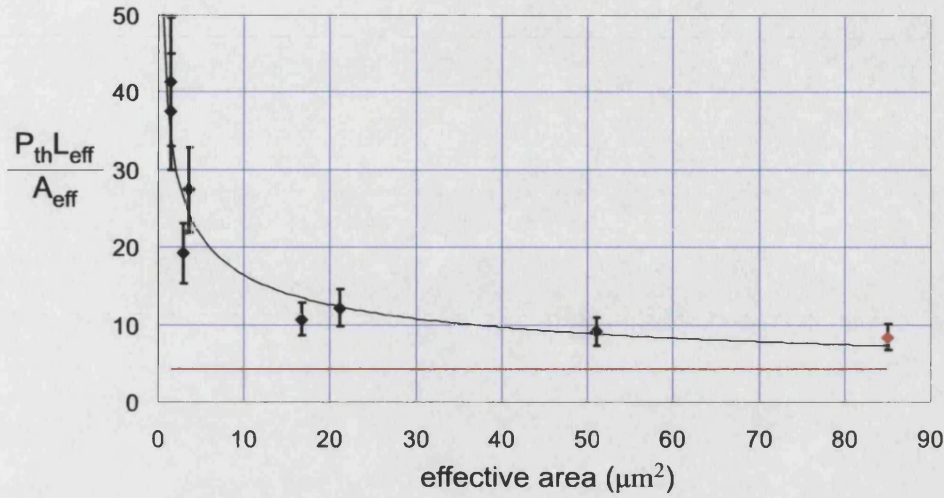
Figure 12.3: Plot showing the variation in threshold powers for PCF's with different core diameters. The red point corresponds to the *Pirelli* SMF.

The results are shown in figure 12.3. The points have been normalised to remove the dependence associated with the different lengths and effective areas so that the fibres can be compared on an equal footing. Rearranging equation 9.6, it is found that

$$\frac{P_{th}L_{eff}}{A_{eff}} = \frac{21}{g_B}.$$

(12.1)

If conventional theory is to predict the threshold power for stimulated Brillouin scattering in PCF, the plot should be nothing more than a linear array of points located at a y-value determined by the RHS of equation 12.1. For conventional SMF the gain parameter g_B has the value $5 \times 10^{-11} m/W$ as given by Agrawal [63] and it is this value that is used to generate the horizontal red line in figure 12.3. There is a clear departure of points from this value for PCF's which confine the signal within a small core ($< 2.5\mu m^2$). The *Pirelli* SMF (as shown with the red point) on the other hand, (as well as PCF's which had a large effective area ($> 25\mu m^2$)) showed better agreement with conventional theory (as expected) having a measured value of 4.8mW as compared with a theoretical value of 2.4mW,

In considering a free silica rod, it was shown in the previous section that the elastic modes become separated within the rod and are capable of producing several Brillouin peaks in the Brillouin spectrum. The series of peaks shown in figure 11.13a have an effective bandwidth which is approximately 10 times greater than the spectrum shown in figure 11.13b.

122

Equation 9.6 reveals the inverse relationship of threshold power with Brillouin gain, g_B. Thus, from equation 9.8 it is evident that as Δf_B increases, so will the threshold power. In constructing an envelope to enclose the three Brillouin peaks of figure 11.13a, and in applying the FWHM of that envelope to equation 9.8, the threshold power as determined from equation 9.6 is calculated to be $\sim$70mW. The threshold power for stimulated Brillouin scattering in this fibre was measured experimentally to be 80mW, which is significantly greater than that measured for conventional SMF of $\sim$5mW. Accordingly, this wide effective Brillouin linewidth may be the cause of the high threshold power in small core PCF.

Equally however, it should also be noted that the threshold power for SBS is dependent on the overlap of the interference profile of the pump and Stokes waves, with the displacement profile of the elastic wave (see section 11.2). For small core PCF's the elastic modes become separated by large frequency intervals as shown in figure 11.11. The number of modes per unit frequency available to participate in Brillouin scattering in small core PCF is less than the number in large core PCF. Thus, as core diameter falls, it becomes more likely that the displacement profile of the compressional mode which participates in Brillouin scattering will become less well-matched to the pump/Stokes interference pattern. This overlap mismatch may thus also contribute to the measured increase in the threshold power for stimulated Brillouin scattering.

Chapter 13

Thesis Conclusion

The propagation characteristics of elastic waves in the singly periodic multilayer stack has been presented through the calculation of the associated phononic band structure. The analysis considered the two shear (S) disturbances in addition to the longitudinal (L) disturbance in formulating the dispersion of elastic waves within the periodic system.

The propagation of plane-polarised coupled elastic waves is significantly different from the uncoupled anti-plane waves which possess very similar characteristics to EM wave propagation. Elastic waves however, generally present a more complicated dispersion than EM waves since the L polarisation state couples to the two S polarisation states at interfaces. The L wave produces additional stop-bands within the Brillouin zones, in addition to those at the boundary, which has implications regarding the transmission and reflection characteristics of the system.

The coupling between L and S waves creates regions in frequency and wavevector in which one particular polarisation state of the coupled pair can be extinguished. This clearly provides a basis for a phononic polariser. Equally, similar regions can also allow the particular polarisation state to be conserved during a scattering event, thereby eliminating the re-partition of energy into its coupled partner.

The interaction of the L and S waves at interfaces within the periodic system was found to create an infinite number of possible antiresonance conditions which can take place to close a particular stop-band. The antiresonance conditions were stated in chapter 6, however, it is impossible to calculate which antiresonance condition will take place to close a particular stop-band without first consulting the band edge diagram (or equivalent) for that particular multilayer stack. As a result, coupled L and S waves

could provide the basis for encryption systems since their interaction in closing the stop bands is chaotic without the prior knowledge of the stack composition and geometry.

Acoustooptic interactions within 2D solid core photonic crystal fibres (PCF) has also been presented through measurements of the frequency shift and threshold power associated with Brillouin scattering. Both optical and electrical analysis of the scattering process has been demonstrated with a variety of PCF's.

Using a laser pump of 1550nm, several Brillouin peaks were found to be generated in a 1.22μm diameter core photonic crystal fibre. The discrete nature of these peaks produced an effective Brillouin linewidth approximately 10 times that of the Brillouin linewidth in conventional SMF, and is thought to be the cause of a measured threshold power for stimulated Brillouin scattering approximately 10 times greater than in conventional SMF.

The frequency shift in PCF was modelled by considering the interaction of the fundamental HE_{11} optical mode, with the phase matched compressional modes in a free silica rod. The experimental results showed a decrease in the measured frequency shift with falling core diameter, whereas the rod model indicated that the measured frequency shift should increase as the core diameter is reduced.

The presence of three peaks in the Brillouin spectrum is suggestive of the scattering of the pump wave by three elastic waves within the core. However, it is uncertain whether these elastic waves are guided by a phononic band gap. It could be the case that three optical modes participated in the scattering event to produce the three Brillouin peaks, since the fibre was not single mode at the pump wavelength. In view of this uncertainty, and the variance between the modelled frequency shifts and the experimental results, it is difficult to ascertain whether the elastic waves were guided by a phononic band gap.

Chapter 14

Appendix A: Elements of the Matrix Propagator for In-Plane Polarised Waves

In relating the components of the elastic wave in layer j of period $N+1$ to the equivalent layer of the previous period, the matrix propagator is obtained by taking the product of matrix propagators for the individual layers of period N. Thus, for in-plane polarised waves, the matrix propagator $\mathbf{M_P^{ip}}$, is given by,

$$\mathbf{M_P^{ip}} = \mathbf{M_{j+1}.M_j} \qquad (14.1)$$

The elements of the propagator matrix for layer j ($\mathbf{M_j}$) of the period are given below. Similarly, the elements of the propagator matrix for layer $j+1$ ($\mathbf{M_{j+1}}$) are obtained by interchanging subscripts j for $j+1$ in equation 14.2.

$$m_{11} = m_{44} = \cos(d_j p_{Sj}) + \frac{2\beta^2(\cos(d_j p_{Lj}) - \cos(d_j p_{Sj}))}{(\beta^2 + p_{Sj}^2)}$$

$$m_{12} = m_{34} = \frac{i\beta(2p_{Lj}p_{Sj}\sin(d_j p_{Sj}) + (\beta^2 - p_{Sj}^2)\sin(d_j p_{Lj}))}{p_{Lj}(\beta^2 + p_{Sj}^2)}$$

$$m_{13} = m_{24} = \frac{i\beta(\cos(d_j p_{Lj}) - \cos(d_j p_{Sj}))}{\mu_j(\beta^2 + p_{Sj}^2)}$$

$$m_{14} = \frac{\beta^2\sin(d_j p_{Lj}) + p_{Lj}p_{Sj}\sin(d_j p_{Sj})}{\mu_j p_{Lj}(\beta^2 + p_{Sj}^2)}$$

$$m_{21} = m_{43} = -\frac{i\beta(2p_{Lj}p_{Sj}\sin(d_jp_{Lj}) + (\beta^2 - p_{Sj}^2)\sin(d_jp_{Sj}))}{p_{Sj}(\beta^2 + p_{Sj}^2)}$$

$$m_{22} = m_{33} = \cos(d_jp_{Lj}) + \frac{2\beta^2(\cos(d_jp_{Sj}) - \cos(d_jp_{Lj}))}{(\beta^2 + p_{Sj}^2)}$$

$$m_{23} = \frac{\beta^2\sin(d_jp_{Sj}) + p_{Lj}p_{Sj}\sin(d_jp_{Lj})}{\mu_jp_{Sj}(\beta^2 + p_{Sj}^2)}$$

$$m_{31} = m_{42} = \frac{2i\beta(\cos(d_jp_{Lj}) - \cos(d_jp_{Sj}))\mu_j(\beta^2 - p_{Sj}^2)}{(\beta^2 + p_{Sj}^2)}$$

$$m_{32} = -\frac{(4\beta^2 p_{Lj}p_{Sj}\sin(d_jp_{Sj}) + \mu_j(\beta^2 - p_{Sj}^2)\sin(d_jp_{Lj}))}{p_{Lj}(\beta^2 + p_{Sj}^2)}$$

$$m_{41} = -\frac{(4\beta^2 p_{Lj}p_{Sj}\sin(d_jp_{Lj}) + \mu_j(\beta^2 - p_{Sj}^2)\sin(d_jp_{Sj}))}{p_{Sj}(\beta^2 + p_{Sj}^2)} \tag{14.2}$$

Chapter 15

Appendix B: Dispersion of the Fundamental HE$_{11}$ Mode in a Free Silica Rod

The derivation of the dispersion relation for the fundamental HE$_{11}$ mode begins with Maxwell's equations for a linear, isotropic, lossless dielectric material with no free charges or current sources.

$$\nabla \times \mathbf{E} = -\mu_r \mu_0 \frac{\partial \mathbf{H}}{\partial t} \tag{15.1}$$

$$\nabla \times \mathbf{H} = \epsilon_r \epsilon_0 \frac{\partial \mathbf{E}}{\partial t} \tag{15.2}$$

$$\nabla . \mathbf{E} = 0 \tag{15.3}$$

$$\nabla . \mathbf{H} = 0. \tag{15.4}$$

$\mathbf{E}$ and $\mathbf{H}$ are the electric and magnetic fields respectively, μ_0 the vacuum magnetic permeability ($\mu_0 = 4\pi \times 10^{-7} Hm^{-1}$) and ϵ_0 the vacuum electric permittivity ($\epsilon_0 = 8.854 \times 10^{-12} Fm^{-1}$). Here ϵ_r is the relative dielectric constant ($\epsilon_r = n(\omega)^2$) and μ_r the relative magnetic permeability, assumed ~ 1.

The response of a given material to the passage of an EM wave will depend on the optical frequency ω. This is known as chromatic dispersion and gives rise to a frequency dependent refractive index. The origin of this effect lies at a fundamental level and is related to the resonant frequencies at which the material absorbs the EM radiation.

The frequency dependence of the refractive index (far from the medium resonances) is approximated by the *Sellmier* equation, as shown in equation 15.5 and must be included in the dispersion analysis,

$$n^2(\omega) = 1 + \sum_{j=1}^{m} \frac{B_j \omega_j^2}{\omega_j^2 - \omega^2}. \tag{15.5}$$

Here, ω_j is the jth resonant frequency and B_j is the strength of the jth resonance. For optical fibres these parameters are obtained by fitting a curve to experimental dispersion data and truncating the series to three terms ($m = 3$). For bulk fused silica, these parameters are $B_1 = 0.6961663, B_2 = 0.4079426, B_3 = 0.8974794, \lambda_1 = 0.0684043\mu m, \lambda_2 = 0.1162414\mu m$ and $\lambda_3 = 9.896161\mu m$ where $\lambda_j = 2\pi c/\omega_j$ [63].

Assuming the electric and magnetic field to be of the form $\mathbf{A} = \mathbf{A}(\mathbf{r}, \theta) \exp[-i(\beta z - \omega t)]$, where $\mathbf{A}$ represents the $\mathbf{E}$ or the $\mathbf{H}$-field, equations 15.1 and 15.2 can be manipulated in cylindrical polar coordinates such that the transverse $\mathbf{E}$ and $\mathbf{H}$-field components can be expressed in terms of the longitudinal z-component of the $\mathbf{E}$ and $\mathbf{H}$-fields as shown below,

$$E_r = \frac{-i}{p^2} \left(\frac{\omega\mu}{r} \frac{\partial H_z}{\partial \theta} + \beta \frac{\partial E_z}{\partial r} \right) \tag{15.6}$$

$$E_\theta = \frac{-i}{p^2} \left(\frac{\beta}{r} \frac{\partial E_z}{\partial \theta} - \omega\mu \frac{\partial H_z}{\partial r} \right) \tag{15.7}$$

$$H_r = \frac{-i}{p^2} \left(\beta \frac{\partial H_z}{\partial r} - \frac{\omega\epsilon}{r} \frac{\partial E_z}{\partial \theta} \right) \tag{15.8}$$

$$H_\theta = \frac{-i}{p^2} \left(\frac{\beta}{r} \frac{\partial H_z}{\partial \theta} + \omega\epsilon \frac{\partial E_z}{\partial r} \right) \tag{15.9}$$

where p is the transverse wavevector component ($p^2 = (kn)^2 - \beta^2$). Thus, the problem reduces to finding the z-component of the $\mathbf{E}$ and $\mathbf{H}$-field since once these are known, E_r, E_θ, H_r and H_θ can be determined from equations 15.6-15.9.

Substituting E_r and E_θ in the expression for the z-component of the $\mathbf{H}$-field in the expansion of 15.1 gives,

$$\frac{\partial^2 H_z}{\partial r^2} + \frac{1}{r}\frac{\partial H_z}{\partial r} + \frac{1}{r^2}\frac{\partial^2 H_z}{\partial \theta^2} + p^2 H_z = 0. \tag{15.10}$$

Similarly, substituting for H_r and H_θ in the expression for the z-component of the E-field in the expansion of 15.2 gives,

$$\frac{\partial^2 E_z}{\partial r^2} + \frac{1}{r}\frac{\partial E_z}{\partial r} + \frac{1}{r^2}\frac{\partial^2 E_z}{\partial \theta^2} + p^2 E_z = 0. \tag{15.11}$$

A suitable trial solution to equation 15.10 can be written in the form,

$$H_z = Q R(r) \exp(im\theta) \tag{15.12}$$

where Q is a constant, and m is an integer to ensure that the fields are periodic in θ with a period of 2π (the factor $\exp[-i(\beta z - \omega t)]$ has been omitted). Substitution of equation 15.12 into equation 15.10 leads to the well-known differential equation for $R(r)$,

$$\frac{\partial^2 R}{\partial r^2} + \frac{1}{r}\frac{\partial R}{\partial r} + \left(p^2 - \frac{m^2}{r^2}\right)R(r) = 0. \tag{15.13}$$

The Bessel solutions to equation 15.13 will depend on the region of space to which they apply. The fields must remain finite at all points within the rod, while solutions outside of the rod must decay for $r \to \infty$ if guided solutions are to exist.

Several choices exist for the two independent solutions to equation 15.13. These include Bessel functions of the first ($J_m(pr)$) and second kind ($Y_m(pr)$), as well Hankel functions of the first ($H_m^{(1)}(pr)$) and second kind ($H_m^{(2)}(pr)$). The Bessel function J_m remains finite at $pr = 0$, whereas the Bessel function Y_m, and Hankel functions of the first and second kind are singular at the coordinate origin. For decaying waves the transverse wavevector component p, becomes imaginary. In this case, for large values of r, $H_m^{(1)}(ip\prime r)$ becomes proportional to the exponentially decaying function $\exp(-p\prime r)$, and $H_m^{(2)}(ip\prime r)$ becomes proportional to the exponentially growing function $\exp(p\prime r)$, where $p\prime = (\beta^2 - (kn)^2)^{1/2}$. Thus, the solution to equation 15.13 within the rod ($r < a$) can be written as,

$$H_z = Q J_m(pr) \exp(im\theta), \tag{15.14}$$

and in a similar fashion, the solution for the E-field for $(r < a)$ becomes,

$$E_z = PJ_m(pr)\exp(im\theta) \tag{15.15}$$

where P is a constant.

The field outside of the rod is represented using the Hankel function of the first kind. Since the problem is in search of the guided modes, the coordinate argument will involve imaginary values and so will provide the necessary decay to the fields as $r \to \infty$. For $r > a$,

$$H_z = SH_m^{(1)}(pr)\exp(im\theta), \tag{15.16}$$

and,

$$E_z = RH_m^{(1)}(pr)\exp(im\theta), \tag{15.17}$$

where R and S are constants.

The four unknown constants P, Q, R and S will be determined by the boundary condition, which requires conservation of the tangential field components, E_θ, E_z, H_θ and H_z. The resulting system of four homogeneous equations can then be set up as an eigenvalue equation for β with the modes of the rod being revealed when the determinant of the eigenmatrix is zero [90].

Evaluation of the determinant results in the dispersion relation,

$$\left(\frac{J_m'(U)}{UJ_m} + \frac{H_m^{(1)'}(W)}{WH_m^{(1)}} \right) \left(\frac{J_m'(U)}{UJ_m(U)} + \frac{n_{cl}^2}{n_{co}^2} \frac{H_m^{(1)'}(W)}{WH_m^{(1)}(W)} \right) = \left(\frac{m\beta}{kn_{co}} \right)^2 \left(\frac{V}{UW} \right)^4 \tag{15.18}$$

where $'$ indicates differentiation with respect to the argument, and U, V and W are dimensionless parameters given by,

$$U = a((kn_{co})^2 - \beta^2)^{1/2} \tag{15.19}$$

$$V = ka(n_{co}^2 - n_{cl}^2)^{1/2} \tag{15.20}$$

$$W = a(\beta^2 - (kn_{cl})^2)^{1/2} \tag{15.21}$$

where n_{co} and n_{cl} correspond to the refractive index of the core and cladding respectively. In general for a cylindrical waveguide all field components are coupled, and for each propagation constant β, two sets of degenerate modes exist. Because of the circular symmetry, modes which trace out a helical path, but progress with opposite helicity can have the same β value. These waves are called hybrid *EH* or *HE* modes depending on whether the z-component of the **E**-field or **H**-field is the larger, respectively. The polarisation associated with these waves is circular, rotating clockwise or anticlockwise. Other types of modes also exist which are linearly polarised, having no angular or azimuthal dependence. These are the TE or TM modes depending on whether the **E** or the **H**-field is perpendicular to the plane of propagation, respectively.

References

[1] Yablonovitch, E. (1993). Photonic Band-Gap Structures. *J. Opt. Soc. Am. B,* **10**(2), pp.283-295.

[2] John, S. (1987). Strong Localisation of Photons in Certain Disordered Dielectric Superlattices. *Phys. Rev. Lett.* **58**(23), pp.2486-2489.

[3] John, S., Rangarajan, R. (1988). Optimal Structures for Classical Wave Localisation: An Alternative to the Ioffe-Regel Criterion. *Phys. Rev. B,* **38**(14), pp.10101-10104.

[4] Martinez-Sala, R., Sancho, J., Sanchez, J.V., Gomez, V., Llinares, J. (1995). Sound Attenuation by Sculpture. *Nature,* **378**(16), p.241.

[5] Ball, P. (2002). Sculptured Sound. *New Sci.,* March, pp.32-35.

[6] Cervera, F., Sanchis, L., Sanchez-Perez, J.V., Martinez-Sala, R., Rubio, C., Meseguer, F., Lopez, C., Caballero, D., Sanchez-Dehesa, J. (2002). Refractive Acoustic Devices for Airbourne Sound. *Phys. Rev. Lett.,* **88**(2), pp.023902-1—023902-4.

[7] Kushwaha, M.S., Djafari-Rouhani, B. (1998). Sonic Stop-bands for Periodic Arrays of Metallic Rods: Honeycomb Structure. *J. Sound Vib.,* **218**(4), pp.697-709.

[8] Robertson, W.M., Rudy, J.F. (1998). Measurement of Acoustic Stop-Bands in Two-dimensional Periodic Scattering Arrays. *J. Acoust. Soc. Am.,* **104**(2), pp.694-699.

[9] Kafesaki, M., Sigalas, M.M., Economou, E.N. (1995). Elastic Wave Band Gaps in 3-d Periodic Polymer Matrix Composites. *Solid State Commun.,* **96**(5), pp.285-289.

[10] Liu, Z., Zhang, X., Mao, Y., Zhu, Y.Y., Yang, Z., Chan, C.T., Sheng, P. (2000). Locally Resonant Sonic Materials. *Science,* **289**, pp.1734-1736.

[11] Rayleigh, Lord. (1892). On the Influence of Obstacles Arranged in Rectangular Order Upon the Properties of a Medium. *Photo Phil. Mag.*, **34**, pp.481-502.

[12] Zalipaev, V.V., Movchan, A.B., Poulton, C.G., McPhedran, R.C. (2002). Elastic Waves and Homogenisation in Oblique Periodic Structures. *Proc. R. Soc. Lond. A*, **458**, pp.1887-1912.

[13] Poulton, C.G., Movchan, A.B., McPhedran, R.C., Nicorovici, N.A., Antipov, A. (2000). Eigenvalue Problems for Doubly Periodic Elastic Structures and Phononic Band Gaps. *Proc. R. Soc. Lond. A*, **456**, pp.1-17.

[14] Platts, S.B., Movchan, N.V., McPhedran, R.C., Movchan, A.B. (2002). Two-dimensional Phononic Crystals and Scattering of Elastic Waves by an Array of Voids. *Proc. R. Soc. Lond. A*, **458**, pp.2327-2347.

[15] Platts, S.B., Movchan, N.V., McPhedran, R.C., Movchan, A.B. (2003). Band Gaps and Elastic Waves in Disordered Stacks: Normal Incidence. *Proc. R. Soc. Lond. A*, **459**, pp.221-240.

[16] Kushwaha, M.S., Halevi, P., Martinez, G. (1994). Theory of Acoustic Band Structure of periodic elastic composites. *Phys. Rev. B*, **49**(4), pp.2313-2322.

[17] Sigalas, M.M., Economou, E.N. (1996). Attenuation of Muliple Scattered Sound. *Europhys. Lett.*, **36**(4), pp.241-246.

[18] Russell, P.St.J., Birks, T.A., Dominic Lloyd-Lucas, F. eds. Burstein, E., Weisbuch, C. (1995). Photonic Bloch Waves and Photonic Band Gaps. *Confined Electrons and Photons*, New York, Plenum Press.

[19] Russell, P.St.J., Tredwell, S., Roberts, P.J. (1999). Full Photonic Bandgaps and Spontaneous Emission Control in 1-d Multilayer Dielectric Structures. *Opt. Commun.*, **160**, pp.66-71.

[20] Ursin, B. (1983). Review of Elastic and Electrodynamic Wave Propagation in Horizontally Layered Media. *Geophysics*, **48**(8), pp.1063-1081.

[21] Lauriks, W., Mees, P., Allard, J.F. (1992). The Acoustic Transmission through Layered Systems. *J. Sound Vib.*, **155**(1), pp.125-132.

[22] Brouard, B., Lafarge, D., Allard, J.F. (1995). A General Method of Modelling Sound Propagation in Layered Media. *J. Sound Vib.*, **183**(1), pp.129-142.

[23] Gilbert, F., Backus, G. (1996). Propagator Matrices in Elastic Wave and Vibration Problems. *Geophysics*, **31**(2), pp.326-332.

[24] Allard, J.F., Champoux, Y., Depollier, C. (1987). Modelisation of Layered Sound Absorbing Materials with Transfer Matrices. *J. Acoust. Soc. Am.*, **82**(5), pp.1792-1796.

[25] Esquivel-Sirvent, R., Cocoletzi, G.H. (1994). Band Structure for the Propagation of Elastic Waves in Superlattices. *J. Acoust. Soc. Am.*, **95**(1), pp.86-90.

[26] Djafari-Rouhani, B., Dobrzynski, L., Hardouin Duparc, O. (1983). Sagittal Elastic Waves in Infinite and Semi-Infinite Superlattices. *Phys. Rev. B*, **28**(4), pp.1711-1720.

[27] Marin, E., mangan, B.J., Diez, A., Russell, P.St.J. (2001). Acoustic Modes of a Dual-Core Square Lattice Photonic Crystal Fibre Preform. *Proc. European Conf. Opt. Commun., ECOC Amsterdam.* pp518-519.

[28] Dimmick, T.E., Kakarantzas, G., Birks, T.A., Diez, A., Russell, P.St.J. (2000). Compact All-Fibre Acoustooptic Tunable Filters with Small Bandwidth-Length Product. *IEEE. Photonics Tech. L.*, **12**, pp.1210-1212.

[29] Diez, A., Kakarantzas, G., Birks, T.A., Russell, P.St.J. (2000). High Strain-Induced Wavelength Tunability in Tapered Fibre Acoustooptic Filters. *Electron Devic. Lett.*, **36**(14), pp.1187-1188.

[30] Liu, W.F., Russell, P.St.J., Dong, L. (1997). Acoustooptic Superlattice Modulator using a Fibre Bragg Grating. *Opt. Lett.*, **22**(19), pp.1515-1517.

[31] Fokker, P.A., Dijkhuis, J.I., de Wijn, H.W. (1997). Stimulated Emission of Phonons in and Acoustical Cavity. *Phys. Rev. B*, **55**(5), pp.2925-2933.

[32] Pan, Y., Rossignol, C., Audoin, B. (2003). Acoustic Waves Generated by a Laser Line Pulse in a Transversely Isotropic Cyclinder. *Appl. Phys. Lett.*, **82**(24), pp.4379-4381.

[33] Gusev, V., Picart, P., Mounier, D., Breteau, J.-M. On the possibility of Ultrashort Shear Acoustic Pulse Excitation due to the Laser-Induced Electrostrictive Effect. *Opt. Commun.*, Article in Press.

[34] Hurley, D.H., Wright, O.B., Matsuda, O., Gusev, V.E., Kolosov, O.V. (2000). Laser Picosecond Acoustics in Isotropic and Anisotropic Materials. *Ultrasonics*, **38**, pp.470-474.

[35] Trigo, M., Bruchhausen, A., Fainstein, A., Jusserand, B., Thierry-Mieg, V. (2002). Confinement of Acoustical Vibrations in a Semiconductor Planar Phonon Cavity. *Phys. Rev. Lett.*, **89**(2), pp.227402-1—227402-4.

[36] Worlock, J.M., Roukes, L. (2003). Son et Lumière. *Nature*, **421**, pp.802-803.

[37] Landau, L.D., Lifschitz, E.M. (1986). *Theory of Elasticity: Volume 7 of Course of Theoretical Physics.* 3^{rd}ed. Oxford: Butterworth-Heinemann Ltd.

[38] Royer, D., Dieulesaint, E. (1996). *Elastic Waves in Solids I - Free and Guided Propagation.* Berlin: Springer-Verlag.

[39] Brekhovskikh, L.M., Godin, O.A. (1995). *Acoustics of Layered Media I.* London: Springer-Verlag.

[40] Hook, J.F. (1961). Separation of the Vector Wave Equation of Elasticity for Certain Types of Inhomogeneous Isotropic Media. *J. Acoust. Soc. Am.*, **33**(3), pp.302-.

[41] Ewing, W.M., Jardetsky W.S., Press, F. (1957). *Elastic Waves in Layered Media.* New York: McGraw-Hill Book Company.

[42] Born, M., Wolf, E. (1965). *Priciples of Optics - Electromagnetic Thoery of Propagation, Interference and Diffraction of Light.* 3^{rd}ed. Oxford: Pergamon Press.

[43] Stoneley, R. (1924). Elastic Waves at the Surface of Separation of Two Solids. *Photo Proc. R. Soc. Lond. A*, **106**, pp.416-428.

[44] Mindlin, R.D. (1950). Thickness-Shear and Flexural Vibrations of Crystal Plates. *J. Appl. Phys.*, **22**(3), pp.316-323.

[45] Russell, P.St.J. (1986). Optics of Floquet-Bloch Waves in Dielectric Gratings. *Appl. Phys. B*, **39**, pp.231-246.

[46] Malischewsky, P.G. (2000). Some Special Solutions of Rayleigh's Equation and the Reflections of Body Waves at a Free Surface. *Geophys. J. Int.*, **39**(2), pp.155-160.

[47] Manzanares-Martinez, B., Ramos-Mendieta, F. (2000). Transverse Elastic Waves in Superlattices: The Brewster Acoustic Angle. *Phys. Rev. B*, **61**(19), pp.12877-12881.

[48] Achenbach, J.D. (1973). *Wave Propagation in Elastic Solids.* Amsterdam: North-Holland Publishing Company.

[49] Parmley, S., Zobirst, T., Clough, T., Perez-Miller, A., Makela, M., Yu, R. (1995). Phononic Band Structure in a Mass Chain. *Appl. Phys. Lett.*, **67**(6), pp.777-779.

[50] Kittel, C. (1996). *Introduction to Solid State Physics.* 7^{th}ed. Canada: John Wiley & Sons.

[51] Ziman, J.M. (1964). *Principles of the Theory of Solids.* Cambridge: Cambridge University Press.

[52] Russell, P.St.J. (1986). Interference of Integrated Floquet-Bloch Waves. *Phys. Rev. A*, **33**(5), pp.3232-3242.

[53] Boumaiza, Y., Hadjoub, Z., Doghmane, A., Deboub, L. (1999). Porosity Effects on different measured Acoustic Parameters of Porous Silicon. *J. Mat. Sci. Lett.*, **18**, pp295-297.

[54] Auld, B.A. (1990). *Acoustic Fields and Waves in Solids Vol I*. Florida: Krieger Publishing Company.

[55] Robertson, W.M., Ash, J., McGaugh, J.M. (2002). Breaking the Sound Barrier: Tunneling of Acoustic Waves through the Forbidden Transmission Region of a 1D Acoustic Band Gap Array. *Am. J. Phys.*, **70**(7), pp.689-693.

[56] Lamb, H. (1917). On Waves in an Elastic Plate. *Proc. R. Soc. Lond.*, **93**, pp.114-128.

[57] Brekhovskikh, L.M. (1956). The Dispersion Equation for Normal Waves in Laminar Media. *Soviet Physics Acoustics: A Translation of the Journal of Academy of Sciences of the USSR*, **2**(4), pp.362-374.

[58] Meitzler, A.H. (1965). Backward-Wave Transmission of Stress Pulses in Elastic Cylinders and Plates. *J. Acoust. Soc. Am.*, **38**, pp.835-842.

[59] Tolstoy, I., Usdin, E. (1957). Wave Propagation in Elastic Plates: Low and High Mode Dispersion. *J. Acoust. Soc. Am.*, **29**(1), pp.37-42.

[60] Holland S.D., Chimenti, D.E. (2003). Air Coupled Acoustic Imaging with Zero Group-Velocity-Lamb Modes. *Appl. Phys. Lett.*, **83**13, pp.2704-2706.

[61] Boyd, R.W., Rzażewski, K. (1990). Noise Initiation of Stimulated Brillouin Scattering. *Phys. Rev. A*, **42**(9), pp.5514-5521.

[62] Waarts, R.G., Braun, R.P. (1985). Crosstalk Due to Stimulated Brillouin Scattering in Monomode Fibre. *Electron Devic. Lett.*, **21**(23), pp.1114-1115.

[63] Agrawal, G.P. (1995). *Nonlinear Fibre Optics*. 2nded. San Diego: Academic Press.

[64] Russell, P.St.J., Culverhouse, D., Farahi, F. (1990). Experimental Observation of Forward Stimulated Brillouin Scattering in Dual-Mode Single-Core Fibre. *Elec. Lett.*, **26**(15), pp1195-1196.

[65] Russell, P.St.J., Culverhouse, D., Farahi, F. (1991). Theory of Forward Stimulated Brillouin Scattering in Dual-Mode Single Mode Fibres. *IEEE J. Quant. Elec.*, **27**(3), pp.836-842.

[66] Ippen E.P., Stolen, R.H. (1972). Stimulated Brillouin Scattering in Optical Fibres. *Appl. Phys. Lett.*, **21**(11), pp.539-541.

[67] Yeniay, A., Delavaux, J-M., Toulouse, J. (2002). Spontaneous and Stimulated Brillouin Scattering Gain Spectra in Optical Fibres. *J. Lightwave Technol.*, **20**(8), pp.1425-1432.

[68] Shibata, N., Waarts, R.G., Braun, R.P. (1987). Brillouin-Gain Spectra for Single Mode Fibres having Pure-Silica, GeO$_2$ doped and P$_2$O$_5$ doped core. *Opt. Lett.*, **12**(4), pp.269-271.

[69] Dämmig, M., Zinner, G., Mitschke, F., Welling, H. (1993). Stimulated Brillouin Scattering in Fibres With and Without External Feedback. *Phys. Rev. A*, **48**(4), pp.3301-3309.

[70] Gaeta, A.L., Boyd, R.W. (1991). Stimulated Brillouin Scattering in the Presence of External Feedback. *Int. J. Nonlinear Opt. Phys.*, **1**(3), pp.581-594.

[71] Barrell, H., Teasdale-Buckell, P. (1951). The Correction for Dispersion of Phase Change in Fabry Perot Interferometers. *Proc. Phys. Soc. B*, **64**(5), pp.413-418.

[72] Lee, J.H., Yusoff, Z., Belardi, W., Ibsen, M. Monro, T.M., Richardson, D.J. (2002). Investigation of Brillouin Effects in Small Core Holey Optical Fibre: Lasing and Scattering. *Opt. Lett.*, **27**(11), pp.927-929.

[73] Shibata, N., Azuma, Y., Horiguchi, T., Tateda, M. (1988). Identification of Longitudinal Acoustic Modes Guides in the Core Region of a Single-Mode Optical Fibre by Brillouin Gain Spectra Measurements. *Opt. Lett.*, **13**(7), pp.595-597.

[74] Hecht, E., Zajac, A. (1977). *Optics* 2nded. London: Addison-Wesley Publishing Company.

[75] Cregan, R.F., Mangan, B.J., Knight, J.C., Birks, T.A., Russell, P.St.J., Roberts, P.J., Allan, D.C. (1999). Single Mode Photonic Band Gap Guidance of Light in Air. *Science*, **285**, pp.1537-1539.

[76] Knight, J.C., Broeng, J., Birks, T.A., Russell, P.St.J. (1998). Photonic Band Gap Guidance in Optical Fibres. *Science*, **282**, pp.1476-1478.

[77] Knight, J.C., Birks, T.A., Russell, P.St.J., Atkin, D.M. (1996). All Silical Single Mode Optical Fibre with Photonic Crystal Cladding. *Opt. Lett.*, **21**(19), pp.1547-1549.

[78] Russell, P.St.J., Birks, T.A., Knight, J.C., Cregan, R.F., Mangan, B.J., De Sandro, J-P. (1998). Silica/Air Photonic Crystal Fibres. *Jpn. J. Appl. Phys.*, **37**, pp.45-48.

[79] Birks, T.A., Knight, J.C., Russell, P.St.J. (1997). Endlessly Single-Mode Photonic Crystal Fibre. *Opt. Lett.*, **22**(13), pp.961-963.

[80] Maughan, S.M., Kee, H.H., Newson, T.P. (2001). Simultaneous Distributed Fibre Temperature and Strain Sensor using Microwave Coherent Detection of Spontaneous Brillouin Backscattering. *Meas. Sci. Technol.*, **12**(7), pp834-842.

[81] Alahbabi, M.N., Cho, Y.T., Newson, T.P. (2004). 100km Distributed Temperature Sensor based on Coherent Detection of Spontaneous Brillouin Backscattering. *Meas. Sci. Technol.*, **15**(8), pp1544-1547.

[82] Bongrand, I., Picozzi, A., Piochelle, E. (1998). Coherent Model of Cladding Brillouin Scattering in Single Mode Fibres. *Electron Devic. Lett.*, **34**(18), pp.1769-1770.

[83] Tang, C.L. (1966). Saturation and Spectral Characteristics of the Stokes Emission in the Stimulated Brillouin Process. *J. Appl. Phys.*, **37**(8), pp.2945-2955.

[84] Smith, R.G. (1972). Optical Power Handling Capacity of Low Loss Optical Fibres Determined by Stimulated Raman and Brillouin Scattering. *Appl. Opt.*, **11**(11), pp.2489-2494.

[85] Damen, E.P.N., Dieleman, D.J., Arts, A.F.M, de Wijn, H.W. (2001). Generation and Propagation of Coherent Phonon Beams. *Phys. Rev. B*, **64**(17), pp.174303-1—174303-12.

[86] Wait, P.C., Newson, T.P. (1995). Measurement of Brillouin Scattering Coherence Length as a function of Pump Power to determine Brillouin Linewidth. *Optcs. Comm.*, **117**(1-2), pp.142-146.

[87] Thurston, R.N. (1978). Elastic Waves in Rods and Clad Rods. *J. Acoust. Soc. Am.*, **64**(1), pp.1-37.

[88] Kaul, R.K., McCoy, J.J. (1964). Propagation of Axisymmetric Waves in a Circular Semi-infinite Elastic Rod. *J. Acoust. Soc. Am.*, **36**(4), pp.653-660.

[89] Tkach, R.W., Chraplyvy, W.R., Derosier, R.M. (1986). Spotaneous Brillouin Scattering for Single Mode Optical Fibre Characterisation. *Electron Lett.*, **22**(19), pp.1011-1013.

[90] Marcuse, D. (1981). *Principles of Optical Fiber Measurements*. New York: Academic Press.